Laboratory Measurements and Modeling of Trace Atmospheric Species
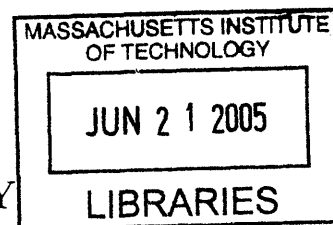
by

Philip M. Sheehy

Submitted to the Department of Chemistry
in partial fulfillment of the requirements for the degree of

Doctor of Philosophy

at the

MASSACHUSETTS INSTITUTE OF TECHNOLOGY

June 2005

Author ....
Department of Chemistry
May 09, 2005

Certified by ....
Jeffrey I. Steinfeld
Professor of Chemistry
Thesis Supervisor

Certified by ....
Mario J. Molina
Institute Professor
Thesis Supervisor

Accepted by ....
Robert W. Field
Chairman, Department Committee on Graduate Students

This doctoral thesis has been examined by a Committee of the Department of Chemistry that included:

Professor Robert W. Field ....

Chairperson

Professor William H. Green...................................

Professor Mario J. Molina ....

Thesis Co-Supervisor

Professor Jeffrey I. Steinfeld ....

Thesis Co-Supervisor

Laboratory Measurements and Modeling of Trace Atmospheric Species

by

Philip M. Sheehy

Abstract

Trace species play a major role in many physical and chemical processes in the atmosphere. Improving our understanding of the impact of each species requires a combination of laboratory experimentation, field measurements, and modeling. The results presented here focus on spectroscopic and kinetic laboratory measurements and photochemical box modeling.

Laboratory experiments were conducted using IntraCavity Laser Absorption Spectroscopy (ICLAS), a high-resolution, high sensitivity spectroscopic method that had been used primarily for static cell measurements in the Steinfeld Laboratory at MIT. Several modifications and improvements have been made to expand its versatility. Firstly, a discharge flow tube was coupled with the ICLA Spectrometer, and the formation kinetics of nitrosyl hydride, HNO, were measured as a means to test the system. Secondly, a novel edge-tuner was introduced as a means to expand the spectral range of the ICLA Spectrometer. An experiment for the detection of the hydroperoxyl radical employing the edge-tuner in the ICLA Spectrometer is discussed and proposed.

The results from the laboratory measurements are followed by the presentation of a near-explicit kinetic box model designed to improve our understanding of the oxidative capacity of the urban troposphere in the Mexico City Metropolitan Area (MCMA). The box model was constructed using the Master Chemical Mechanism and was constrained using a large dataset of field measurements collected during the 2003 MCMA field campaign. The modeling is focused on the hydroxy and hydroperoxyl radicals (OH and HO_2), with an emphasis on the role of volatile organic compounds (VOCs) in the formation of both species.

Thesis Supervisor: Jeffrey I. Steinfeld
Title: Professor of Chemistry

Thesis Supervisor: Mario J. Molina
Title: Institute Professor

for my family

Acknowledgments

During my tenure at MIT as a graduate student, I have been fortunate enough to pursue a variety of research objectives. My two advisors, Jeff Steinfeld and Mario Molina have played a major role in providing me with numerous opportunities and appropriate direction. Although I am a joint student, I spent most of my time at MIT with Jeff Steinfeld. Jeff was always supportive of whatever endeavor I pursued, whether it was in the laboratory or developing my interest in sustainable development. The combination of my research with Jeff and Mario, and Jeff's willingness to let me explore opportunities outside the laboratory have helped shaped my career goals. And although I spent most of my time with Jeff, Mario was always very supportive of my research and always seemed to ask the right questions that made me think about my research in different ways.

The other members of my thesis committee, Bob Field and Bill Green, have also been extremely helpful in my development as a scientist. Bob and Bill both allowed me to attend their group meetings, and their door was always open. Scott Witonsky showed me the ropes on ICLAS when I first got to MIT; and basically was a role model as to how to find that balance between grad school and life. Martin Hunter and Benjamin de Foy were post-docs and office mates that made working all the more enjoyable, and provided me with a valuable source of know-how and understanding. Rainer Volkamer was particularly instrumental in helping me finish my thesis, as he basically took me under his wing when I wasn't really sure what the hell I was going to do to wrap up my 'story' as a graduate student. He put faith in me when others would not have. I'll always be grateful for that. I was kind of an army-of-one for much of my tenure at MIT; members of the Molina Group - in particular, Keith Broekhuizen, Alan Bertram, and Faye McNeill -, the Field Group and Green Group were always around to help me out when necessary. I'd also like to thank Dara O'Rourke for being a mentor and for helping me put my skills as a scientist to practical use. I was fortunate enough to spend 3 days in the laboratory with Sasha Kachanov - an expert laser engineer who makes it all look easy and fun. I'd also like to send a shout-out

to my undergraduate research advisor, Tore Ramstad, who is a great scientist and a good friend.

Outside of the laboratory, I was fortunate enough to find friends in all walks of life. All of the students that have come and gone for SfGS and the WSCSD have been great to get to know, and are far too many to list. Craig Breen, Isaac Manke, JP Cosgrove and the rest of LLUA were always around for a game of basketball or football. My roommate of four years and friend from high school, Josh Fiala, was always around and I'm thankful for his friendship. Josh's fiancee, Jeannette Allen, is a good person, and I'm glad that we're friends. Josh Vaughan and Brent Fisher (along with the aforementioned Craig Breen) were instrumental in acclimating to grad school and getting through some tough first year classes. I met Josh Figueroa within the first week of graduate school; and we have remained good friends ever since, and it'll probably stay that way for a long long time. I met Hilarie Tomasiewicz as a first-year; a lot has changed since then and I am happy that we are still friends today. The Party Guys (Craig, JP, Josh Fiala, and Boomer) came along in the summer of 2003 to help put life in perspective. More recently, I always seem to have a great time when I hang out with Vicky Canto and/or Max Berniker. I regret not having had the opportunity to spend more time with Karim Abdul-Matin and Victor Hebert.

Shawdee Eshghi has been my best friend while I've been at MIT. Her boundless energy, love of science, and insistence on challenging herself at all times are just a few things that come to mind when I think about the most interesting and beautiful person I have ever met. My best friends from my undergraduate years - Joe, Daniel, David, Kurt, Matthew and Jeff - were infinitely supportive over the last 5 years. And finally, I need to thank my family. My siblings: Ann, Rita, Barbara, Michael and John. Michael (aka el presidente) deserves special mentioning, as he and I spent some of the best times of our short lives together in Cambridge: lunches on the weekends, movie challenges, and epidemics. Most importantly, I'd like to thank my mom and dad. Two great people with two big hearts and sharp minds.

Contents

List of Figures

List of Tables

Chapter 1

Introduction

The predominance of relatively inert species, such as nitrogen (N_2) and oxygen (O_2), belies the complexity of the physical and chemical processes that govern the earth's dynamic atmosphere. Trace amounts of reactive molecular fragments, called free radicals, play an integral role in the earth's radiative balance and in the chemical properties of the atmosphere [1]. A principal objective of laboratory studies of free radicals is to obtain the data necessary to understand their behavior in the atmosphere [2]. Spectroscopic and kinetic measurements of free radicals offer valuable insights into the processes governing the atmosphere; however, these studies are often challenging. The high reactivity of free radicals and the difficulty in generating, and subsequently isolating the free radical for analysis are barriers that require adaptive and creative experimental methods. A well-designed experiment will yield the desired spectroscopic signatures or kinetic information of the species of interest.

Absorption spectroscopy is one of many tools available used to study free radicals in the atmosphere. Sir Isaac Newton established the basis for optical spectroscopy when he observed the dispersion of sunlight by a prism over 300 years ago [3]. After the characterization of emission and absorption by Kirchoff and Bunsen in the 19th century [4], laboratory studies focused on emission techniques, rather than absorption. In 1955, after Sir Alan Walsh had introduced the concept of atomic absorption, the first atomic absorption spectrometer was used to measure the atomic vapors of metals [5].

The Beer-Lambert law [6] governs absorption spectroscopy,

$$A = -\ln \frac{I}{I_o} = \sigma N l_{eff} \qquad (1.1)$$

where A is the absorbance, I is the transmitted light, I_o is the incident light, σ is the absorption cross-section, N is the number density of the species being measured, and l_{eff} is the effective absorption pathlength. Assuming the number density of the species of interest is a limiting factor, the sensitivity of an absorption technique can be increased by either increasing the pathlength or decreasing the noise of the experiment. In 1942, a method for generating longer pathlengths was achieved by introducing a multipass absorption cell, commonly referred to as a "White" cell [7]. The introduction of lasers in the late 1950s and early 1960s [8, 9] provided a new method for extending the pathlength of absorption techniques using multi-pass cells, such as the White cell. Although an increased pathlength was achieved using these methods, the sensitivity was ultimately limited by the reflectivity of the mirrors. Because the reflectivity of the mirrors was less than 100%, there was a marked decrease in the intensity of the laser beam with increased effective pathlength, which is akin to increasing the noise of the experiment.

Cavity enhanced spectroscopy, introduced in the 1970s, enables the user to achieve longer pathlengths without increasing the noise by placing the sample of interest inside the cavity of a laser. Several groups recognized that a set of broadband lasers were very sensitive to intracavity, narrowband absorption losses – giving birth to IntraCavity Laser Absorption Spectroscopy (ICLAS) [10–12]. Light from a lasing medium reflects through a sample as many as 10^5 times. The increase in the number of passes increases the effective pathlength, amplifying the absorption lines of the target species, which will appear superimposed on the broad spectrum of the laser.

ICLAS is a high-resolution, high sensitivity technique, making it an attractive alternative to traditional multi-pass absorption cells or a Fourier Transform spectrometer. ICLAS has the sensitivity and resolution to perform a variety of absorption spectroscopic analyses that are useful to the fields of molecular spectroscopy, atmospheric spectroscopy, reaction dynamics and kinetics, nonlinear optical phenomena,

two-photon absorption, etc..

The Steinfeld Laboratory at MIT first constructed an ICLAS laser system in the spring of 1998. It is important to note that the spectrometer is not a "black box" that one simply plugs into an existing laser system, but rather a complicated tool requiring careful assembly and user-determined modifications to optimize the performance of the instrument. Initial studies using ICLAS concentrated on demonstrating the ability of the instrument to make quantitative measurements on the spectroscopic features of the A band of oxygen ($b^1\Sigma_g^+ \leftarrow X\ ^3\Sigma_g^-$) [13]. That study was followed by measurements on the second overtone of the OH stretch of nitrous acid, HONO, an important atmospheric species [14]. The system has since been modified to measure the kinetics of trace species in a flow tube, and has most recently been modified significantly by extending the spectral range in order to measure the spectroscopy and kinetics of a broader range of species. A detailed introduction to the theory and operation of ICLAS is presented in Chapter 2.

The ICLAS system was originally used to make spectroscopic measurements on static systems; however, the potential to make kinetic measurements by coupling ICLAS with a flow tube was an attractive possibility. In Chapter 3, the successful implementation of Kinetics using IntraCavity Absorption Spectroscopy (KICAS) is presented. Nitrosyl hydride, HNO, was used as a test species to validate the KICAS method. Originally, the reaction of HNO with O_2 was studied; however, flaws in the original experimental design required that an alternate approach be employed. Searching for a faster reaction, the formation kinetics of HNO from atomic hydrogen, H, and nitric oxide, NO, fit the profile of an ideal test reaction. The kinetics of the reaction was monitored using the (000) $\leftarrow$ (000) band of the $\tilde{A}^1A'' \leftarrow \tilde{X}^1A'$ electronic transition of HNO.

In Chapter 4, the implementation of a novel edge-tuner to extend the detection range of the ICLA Spectrometer to longer wavelengths is presented. The custom-made edge-tuner (designed by Alexander Kachanov) extended the spectral range of ICLAS to 1040 nm. We present the performance of the ICLAS laser in this extended spectral region with a focus on a proposed experiment designed to detect HO_2.

The kinetics study of HNO and the proposed experiment to detect HO_2 absorption features in the near infra-red using ICLAS focus on the spectroscopy and kinetics of targeted trace species. Understanding the processes of the atmosphere, such as the formation of photochemical ozone in the troposphere, is a difficult task because it requires detailed mechanisms that have been constructed based on substantive laboratory (i.e. smog chamber) and field measurements. Atmospheric chemistry models are an important tool in connecting our basic understanding of each individual trace species, such as HNO and HO_2, and the multiple roles they play in chemical and physical processes. A combination of laboratory measurements, field measurements, and an accurate box model provide a valuable tool for devising a robust strategy for solving air quality problems (see Molina and Molina [15], for instance).

In Chapter 5, the results from a tailored box model of the urban troposphere of the Mexico City Metropolitan Area are presented. A combination of the Master Chemical Mechanism (MCM), FACSIMILE software, and an extensive set of field data obtained from the 2003 MCMA field campaign were used to conduct a comprehensive study of the oxidative capacity of the urban troposphere with a focus on OH and HO_2 radical chemical processes. A detailed explanation of the model construction, particularly the methodologies used for constraining the code, is presented. A comparison between measured and modeled values for HO_X species ($HO_X = OH + HO_2$) is presented. The relative contributions of VOCs to the primary formation and secondary formation of HO_X species is presented based on results of simulations. The model is also used to predict representative concentrations of organic peroxy radicals, RO_2 during the 2003 MCMA field campaign.

Chapter 6 summarizes the results presented in Chapters 2-4, and focuses on the connections between laboratory and modeling measurements in atmospheric chemistry.

Chapter 2

Introduction to ICLAS

2.1 Introduction

The theory and operation of ICLAS have been described in detail in several publications and [10–12, 16–18] will be summarized here. According to the Lambert-Beer law of absorption [6]

$$A = \sigma N l_{eff},$$ (2.1)

where A is the absorbance, σ is the absorption cross-section, N is the number density, and l_{eff} is the absorption pathlength. If an experiment is designed to measure an absorber with either weak spectroscopic transitions or at low concentrations, the absorption technique must compensate by increasing the pathlength or decreasing the noise of the experiment. While both methods are experimentally feasible, the ICLAS technique uses the former. A sample cell – the absorber – is placed inside the cavity of a broadband laser. The gain of the laser compensates for losses, while any absorption line that is narrower than the bandwidth of the laser appears superimposed on the broad spectrum of the laser (Figure 2-1) [17]. The laser actually operates as a multipass cell without reflection losses for the narrow absorption lines of the target species.

ICLAS can be operated with most broadband lasers, including dye, color center, Ti:sapphire, Nd:glass, and vertical-external-cavity surface emitting semiconductor lasers (VECSEL). The focus of this work will be on the solid-state Ti:sapphire lasing medium. The Ti:sapphire laser is ideal for the following reasons; the vibronically-
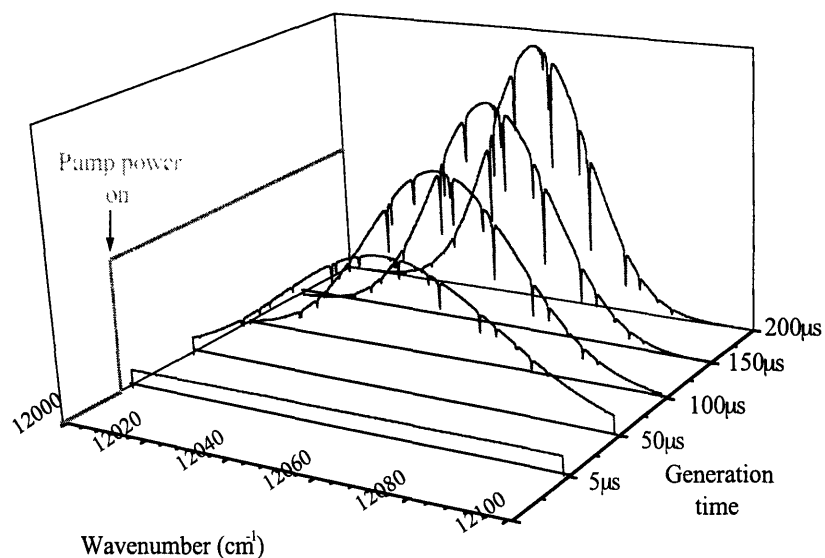
Figure 2-1: Spectro-temporal evolution of the ICLAS laser spectrum with water vapor as an absorber. The broad spectrum of the laser narrows and the narrow absorption lines of water vapor increase linearly as the generation time (proportional to the absorption path length) is increased. (Figure courtesy of A. Garnache).

broadened, emission lines of the Ti:sapphire four-level laser provide a continuously tunable source for wavelengths 700-1000 nm, and the gain medium offers relatively high output powers and frequency stability [19, 20]. The accessible wavelength region of the Ti:sapphire laser used in an ICLAS setup provides access to many low-lying molecular electronic states and overtones of fundamental vibrational modes.

2.2   Theory of operation

The pump power of an argon ion laser creates a population inversion in the Ti:sapphire gain medium that exceeds the threshold value for the cavity, causing the laser to oscillate at the frequency of the maximum of the laser spectrum. The spectral gain profile of a Ti:Sapphire gain medium is illustrated in Figure 2-2. As a homogeneously broadened gain medium, each excited Ti^{3+} ion can simultaneously contribute to the gain of all modes, Q, above threshold and with frequencies within the homogeneous linewidth of the gain medium [21]. Due to this inherent coupling of modes in the homogeneous medium, small changes within the frequency spectrum can potentially

result in profound changes in its output. While the Ti:sapphire laser oscillates simultaneously on all Q modes, if one mode, q_k, is tuned into resonance with an absorption line of the sample at frequency ν_k, the mode will suffer loss, leading to depletion of the population inversion at q_k. The laser will compensate for this loss with an increase in the gain at q_k. As a homogeneously broadened gain medium, the other $Q-1$ modes can compete for the gain at q_k. As another photon generated at ν_k is absorbed by the sample, q_k will be further depleted by an increase in gain while the remaining $Q-1$ modes can continue to grow. This gain/attenuation process will repeat itself until the gain bandwith narrows and excludes q_k or the laser reaches its stationary phase, which is characterized by the average photon number in the cavity mode, $\langle M_q \rangle$, and the cavity loss rate, γ. Due to the strong coupling of the Ti:sapphire laser modes, it is possible that the mutual interaction will totally quench q_k, resulting in an output at ν_k of zero.
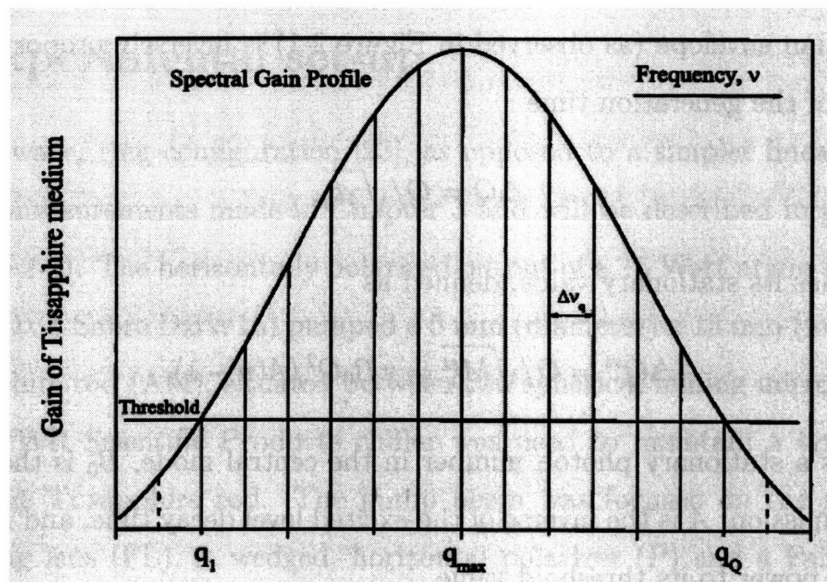
Figure 2-2: The gain profile of a Ti:sapphire laser between ν_{q_1} and ν_{q_Q}. The vertical lines represent the longitudinal modes of the laser cavity, and the spacing between modes is labeled, $\Delta\nu_q$. The horizontal line represents the threshold of the laser, indicating that all modes above this threshold will lase, while those below, represented by the dashed lines are inactive. (Figure from Witsonky [16])

A system of rate equations that couple the gain medium with the number of photons in the cavity can be used to describe the kinetics of the broadband, multimode

laser. Using these rate equations, the evolution of the Ti:sapphire laser with an absorber present is represented by the following [17, 18]:

$$M_q(t_g) = M_{q_o}\sqrt{\frac{t_g}{M}} \exp\left[\left(\frac{q-q_o}{\Gamma}\right)^2 \gamma t_g\right] \exp\left[-\alpha_q l_{eff}\right] \qquad (2.2)$$

where M_q is the number of photons in mode number q, M is a normalization factor, Γ is the half width half maximum (HWHM) of the Lorentzian profile of the stimulated emission centered on its maximum at mode q_0, γ is the cavity loss rate, t_g is the generation time, α is the absorption coefficient, and l_{eff} is the effective absorption pathlength. The two exponential terms in the ICLAS Equation above describe: a) the Gaussian envelope of the laser, and b) the Lambert-Beer law for absorption, characterizing the profile of narrow absorbers in the cavity.

The narrowing of the laser's spectral output is a consequence of competition between the longitudinal modes of the laser [21, 22]. The decrease of the width, ΔQ, of the Gaussian envelope (as observed in Figure 2-1) is inversely proportional to the square root of the generation time

$$\Delta Q = Q/\sqrt{\gamma t_g}, \qquad (2.3)$$

until it reaches its stationary value, defined as

$$\Delta Q^{st} = Q/\sqrt{M_0^{st}} = \pi B_0 Q^2/A(\eta - 1), \qquad (2.4)$$

where M_0^{st} is a stationary photon number in the central mode, B_0 is the rate of the stimulated emission, A is the inverse of the excited level decay time, and η is the ratio of the pump power to its threshold value.

The Lambert-Beer law for absorption, characterized by the second exponential term in Equation 2.2, allows the user to perform high accuracy measurements using ICLAS. For measurements using ICLAS, the absorption pathlength is determined by

$$l_{eff} = \left(\frac{l}{L}\right) ct_g, \qquad (2.5)$$

where l is the absolute absorption pathlength determined by the length of the sample

26

cell, L is the total cavity length, c is the velocity of light, and t_g is the generation time. The ratio of the length of the sample cell, l, to the total cavity length, L, is called the cavity occupation ratio, p.

While the ICLAS laser system embodies a seemingly simple approach – just placing an absorber inside the cavity of a broadband laser – it is actually a sophisticated experimental apparatus. Using an ICLAS laser system is more akin to constructing a laser around a user-defined sample cell, rather than the opposite. Each experimental setup, including the laser and the detection scheme, requires unique customization to facilitate the high-accuracy measurements characteristic of ICLAS. As such, it is not feasible for the user to rely on commercially available lasers and detectors; rather, one must rely on the expertise of the user (trained by an expert laser engineer, such as A. Kachanov) and the expense necessary to construct the system, neither of which is trivial.

2.3 Experimental set-up

A traveling-wave, ring configuration [23], as opposed to a simpler linear cavity, was utilized for measurements made in Chapter 3 and will be described in greater detail here (Figure 2-3). The horizontally polarized output of a 15 Watt argon ion laser (Coherent INNOVA Sabre DBW15) pumped a 5 mm (diameter) x 15 mm (long) Brewster cut, Ti:sapphire rod (AM), situated between two spherical folding mirrors (FM1 and FM2). A VWR Scientific Products chiller was used to maintain a temperature of 13 °C for the Ti:sapphire rod. The pump beam was focused on the gain medium by a focusing lens (FL). A wedged, horizontal polarizer (P) and a Faraday rotator (FR) were inserted into the short arm of the cavity, between the first high reflector (HR1) and the crystal (AM). The Faraday rotator rotates the polarization of the radiation traveling clockwise in the cavity by $+\alpha$ and $-\alpha$ for the counter-clockwise direction. Two high reflectors (HR2 and HR3) act as a compensator and are used to rotate the polarization by $-\alpha$, meaning that the clockwise beam was rotated 0 degrees in the clockwise direction and -2α degrees in the counterclockwise direction. This compensator ensures a uni-directional, traveling-wave, as the Brewster surfaces

27

in the cavity enhance the loss of the rotated radiation, and effectively promotes laser oscillation in only the clockwise direction. The height of the second high reflector (HR2) is adjustable to optimize the compensation. The distance between HR3 and the output coupler (OC) make up the long arm of the cavity, including the sample cell.
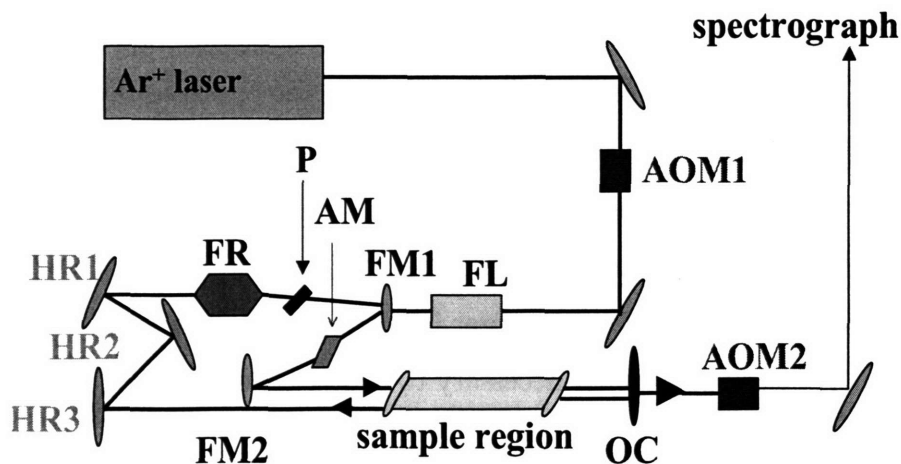
Figure 2-3: Traveling-wave, ring configuration of the IntraCavity Laser Absorption Spectrometer.

The Ti:sapphire laser was continuously tunable between 700-1000 nm. Three sets of mirrors are needed to cover this region. Both the high reflectors and the folding mirrors had better than 99.9 % reflectivity, while the three output couplers had better than 98 % reflectivity. The wavelength regions were as follows: low wavelength (LW), 640-790 nm; middle wavelength (MW), 780-980 nm; and high wavelength (HW), 970-1115 nm. Tuning for each region was generally performed by rotating or translating a pellicle beam splitter, acting as an etalon, inserted into the short arm of the cavity.

Large wedge windows with 2 in. diameter, 0.5 in. thickness, and a 1 degree wedge (CVI Laser Corporation) were used for the sample cells. The entire cavity of the laser, except for the sample cell, was housed within a constructed purge box. During experiments the box was continuously purged with argon to remove residual absorbers, such as water and oxygen. When the concentrations of these absorbers were reduced by three orders of magnitude, generally after 15-20 minutes, experiments were performed.

The generation time of the laser was controlled by two acousto-optic modulators (AOM1 and AOM2). The first gate, AOM1 (IntraAction Corporation model ASM-802B39), directed the pump laser onto the Ti:sapphire gain medium, while the second gate, AOM2 (model ASM-40N), directed the output of the laser to the spectrograph. A 2.5 m echelle grating spectrograph dispersed the laser output, and the spectrally dispersed laser output was recorded with a linear silicon diode array (3,724 pixel Toshiba TCD1301D). The spectrograph could be operated in single, double, or triple pass mode by manually tilting the grating. Alignment of the spectrograph is performed with a 4 mW HeNe laser (Uniphase model 1057-0). The AOMs, the grating position, and the diode array were digitally controlled by software in Delphi programming language written by Alexander Kachanov.

The traveling-wave, ring configuration enhances both the performance and the sensitivity of the instrument. A linear cavity often results in parasitic fringes caused by frequency selective scattering at the maxima of the standing wave of the electric field of the laser on small optical imperfections of the intracavity elements [24]. These imperfections decrease the signal-to-noise ratio and drastically affect the sensitivity of the instrument. In a traveling wave cavity, all the modes are in equal conditions with respect to scattering losses, because there are no maxima and minima of the intracavity field distribution localized differently in space depending on the mode number [24]. It was also known that a weak non-linear dependence of the sensitivity on the generation time exists in the standing-wave laser at 1 ms [25], limiting the pathlength to 300 km. The ring configuration virtually eliminates both the fringes and the non-linear processes that plague the standing wave configuration. Kachanov *et al* [26] demonstrated that, after converting to the ring configuration, the only source of noise in the spectrum was quantum noise due to spontaneous emission into cavity modes. Employing the traveling-wave, ring configuration of the ICLAS laser resulted in achievable pathlengths of up to 3×10^4 km and measurable absorption coefficients as low as $10^{-11} \mathrm{cm}^{-1}$.

While operating the ICLAS laser, it was important to avoid the formation of "clusters" of the longitudinal modes. "Clusters" are frequency dependent losses due

to the natural birefringence of the Ti:sapphire crystal [27]. The crystal acts as a birefringent plate between two polarizers, and if the polarization of the laser inside the crystal was not aligned to the optical axis of the crystal, the electromagnetic wave associated with each longitudinal mode would split into two waves, the ordinary and extraordinary. Interference of these two waves would result in some modes being suppressed. Clusters were not typically a problem for generation times shorter than 100 μs; however, as the generation time was increased, the spectrum would collapse around the clusters as a result of essentially having multiple frequency maxima of the laser spectrum. In this case, the spectrum would eventually appear as a single cluster on a time scale much shorter than the spectral narrowing of the laser [28]. The clustering phenomenon could potentially limit the achievable effective absorption pathlengths to several hundred kilometers.

The silicon linear diode array recorded a spectrum of photon count versus pixel number. The x-axis was calibrated for wavenumber and was linearized to account for the diffraction grating's dispersion. The y-axis was normalized to determine transmittance. Both functions were performed using a computer program titled EtalSpec (authored by Dmitri Permogorov). The wavenumber calibration of ICLAS spectra was performed using nearby transitions from residual water or oxygen absorption lines. Although the cavity of the ICLAS laser was purged with argon, the path from the output coupler to the linear diode array detector was not purged. The 10 meter pathlength between the output coupler and the diode array was sufficient to allow for the absorption of both oxygen and water lines. Depending on the spectral region that the system was set up for, the known frequencies [29] of these lines were used to calibrate the spectra. In the case that the system was operated in a spectral region where oxygen and water absorption lines were insufficiently intense, an iodine absorption cell could be coupled with ICLAS to calibrate the spectra [30].

2.3.1 Time-Resolved Measurements using ICLAS

The basic experimental setup for measuring the spectroscopic parameters of weak absorbers using IntraCavity Laser Absorption Spectroscopy was coupled with a flow

tube to measure kinetics. Although one can measure kinetics using the standard setup by tracking a reactive species over time [16, 31], the flexibility of a flow tube apparatus is an attractive possibility. Also, to our knowledge, an ICLAS system had not been coupled with a discharge flow tube apparatus to measure the kinetics of weak absorbers. A standard discharge flow tube apparatus [32, 33] was constructed using a Pyrex tube (1.8 cm i.d., 65 cm long) and a stainless steel or tygon tubing injector; this apparatus was aligned perpendicular to the sample cell. More specific details about this apparatus will follow in Chapter 3.

2.3.2 ICLAS edge-tuner

An edge-tuner was employed to make measurements at wavelengths longer than 1000 nm (see Chapter 4 for a discussion of species of interest with absorption features at wavelengths longer than 1000 nm). Both the theory and operation of the edge-tuner are presented here. Operation of the laser at the edge of the gain curve requires a strong frequency selector, with the selector loss rapidly increasing on the shorter wavelength side. Such frequency selectors are typically narrowband selectors, precluding their use with ICLAS, as it is a broadband technique. The narrowband selectors can operate at the edge of the gain curve; however, the resulting spectrum is too narrow for ICLAS operation. On the other hand, broadband selectors lack the power to compensate for the decrease in the gain of the laser at longer wavelengths. The author found nothing in the literature describing ICLAS measurements above 1000 nm, using a Ti:sapphire gain medium.

The "edge-tuner" is shown in Figure 2-4. For the sake of simplicity, the standing-wave configuration of the laser was used to demonstrate the utility of the edge-tuner. The standing-wave configuration is essentially the traveling-wave ring configuration (described above in Section 2.3); however, the faraday rotator (FR) and two of the high reflectors (HR2 and HR3) (see Figure 2-3) are removed from the cavity. The introduction of a pair of parallel mirrors mounted on a rotation stage in front of the output coupler provide the optical means for operation of the Ti:sapphire laser between 960 and 1040 nm. The strong spectral dependence of a short-wavelength

edge of a multi-layer dielectric mirror with s-polarization (TM1) provides the tuning capabilities observed.
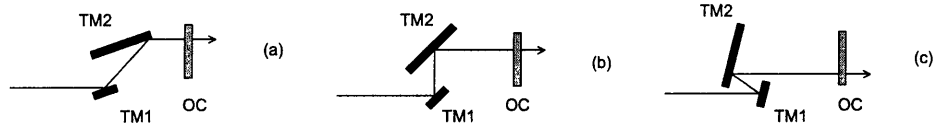
Figure 2-4: Operation of the broadband edge-tuner for ICLAS at varying angles of incidence (AOI). The two parallel mirrors (TM1 and TM2) are rotated to tune the laser: (a) at AOI= 70°, the laser operates at about 960 nm; (b) at AOI= 45°, the laser operates near 1000 nm; (c) at AOI= 5°, the laser is tuned to a maximum wavelength of 1040 nm.

In Figure 2-4-a, the angle of incidence on the TM1 mirror is large, approximately 70°. The TM1 mirror has > 99% reflectivity for s-polarization until about 1000 nm, when its reflectivity drops rapidly. The second mirror, TM2, essentially operates as a high reflector (with a slightly wedged substrate) and has a high reflectivity curve centered at 1020 nm and sufficient bandwidth for tuning. This apparatus provides tuning of the laser to wavelengths up to 1040 nm by simply rotating the pair of mirrors to 'drag' the broadband spectrum of the Ti:sapphire laser to the edge of its gain curve. As the mirror pair is rotated to a smaller angle of incidence (approximately 45° and 5°, respectively) the operational wavelength is tuned to 1000 and 1040 nm, respectively. In each case, the flat reflectivity curve of the high reflector, TM2, tracks the edge of the tuning mirror, TM1, for continuous broadband operation.

Chapter 3

Discharge flow kinetic measurements of HNO

3.1 Introduction

Determining the rate constant for a reaction with multiple reactants can often be difficult because of the complicated data reduction schemes necessary to yield an exact solution. Consider a second-order reaction between two unlike species,

$$X_1 + X_2 \rightarrow X_3 \tag{3.1}$$

The reaction is first order in each of the reactants, X_1 and X_2 and the rate expression is

$$\frac{d[X_1]}{dt} = k[X_1][X_2] \tag{3.2}$$

If the conditions of the experimental design are such that $[X_2] >> [X_1]$, then during the course of the reaction the concentration of X_2 remains nearly constant. This implies that the rate is determined by the equation:

$$[X_1] = [X_1]_0 \exp[-\kappa t], \tag{3.3}$$

where $\kappa = k_1[X_2]$. Equation 3.3 is consistent with the determination of the rate constant for a first-order reaction process; thus, the reaction follows pseudo-first-order kinetics [34]. This makes for a straightforward analysis in determining rate constants for complex reaction schemes.

Discharge flow kinetic measurements are common in the field of chemical kinetics;

the measurement provides a reliable and accurate method for quickly determining a variety of reaction rates for reactive species [34]. At steady-state flow conditions, reaction processes that proceed at a moderately fast rate ($k \approx 10^3$ s^{-1}) are readily determined via a series of measurements made at various reaction intervals that are sufficiently long to maintain a good signal-to-noise ratio. A typical discharge-flow apparatus is shown in Figure 3-1. Let us assume that our discharge-flow kinetics experiment has been designed to meet the requirements for pseudo-first-order kinetics; $[X_2]>>[X_1]$. The reactant, X_1 is injected via a moveable injector to mix with the reactant X_2 over a variable distance z, flowing at a known rate, u. If the concentration c of reactant X_1 is measured at different reaction intervals, and if $(u/A)\ln(c/c(0))$, where A is the cross-sectional area of the flow tube, is plotted against z, the slope of the plot will be $-1/k_1$. The concentration profile of a pseudo first-order process is illustrated in Figure 3-2. Common methods for monitoring a reaction in a flow-tube system include mass spectrometry, laser induced fluorescence, and multiphoton ionization.
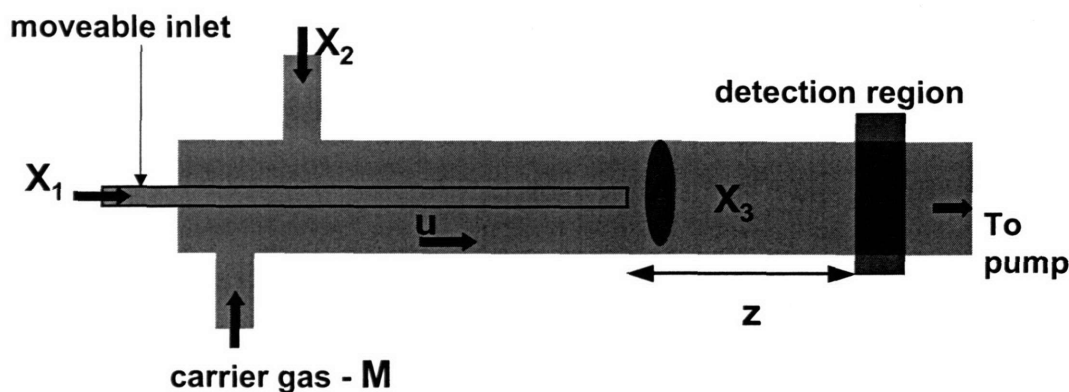
Figure 3-1: A schematic of traditional flow-tube set up using a moveable injector to monitor the reaction, $X_1+X_2 \rightarrow X_3$ under pseudo-first-order kinetics conditions by varying the reaction distance, z.

As noted earlier in Chapter 2, ICLAS has been used extensively for static spectroscopic measurements in the Steinfeld Laboratory at MIT. Because of the sensitivity of the ICLAS technique, we considered it an excellent candidate for detection as part of a discharge flow-tube system for measuring free radical kinetics. We constructed
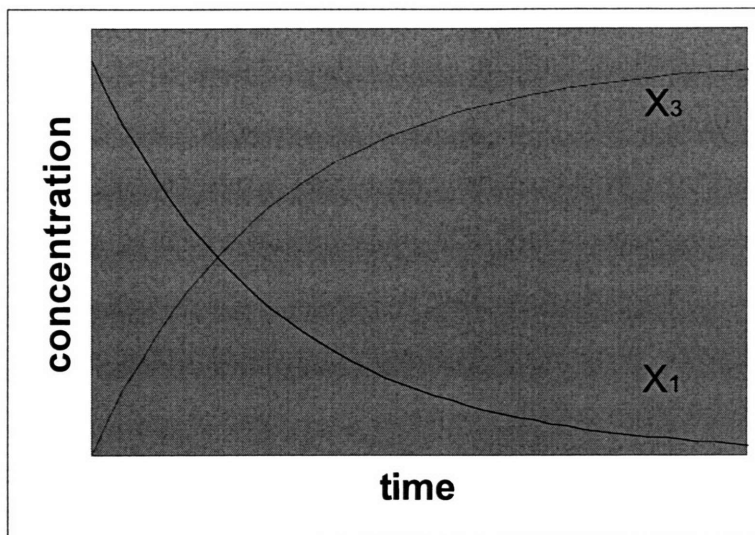
Figure 3-2: A concentration profile of a pseudo-first-order kinetics process, where $[X_2] >> [X_1]$. .

two versions of the discharge flow system for measuring Kinetics using IntraCavity Laser Absorption Spectroscopy (KICAS): one in which the flow was parallel to the axis of the ICLAS laser, and another in which the flow was transverse to the axis of the ICLAS laser. Before getting into the tale of these two set-ups, an introduction to the species of interest is appropriate.

3.2 The Spectroscopy of HNO

Nitrosyl hydride, HNO, was chosen to demonstrate the capability of ICLAS to measure kinetics in a discharge flow system. The HNO molecule was selected for a variety of reasons – it is a key intermediate in number of reactions relevant to the fields of astrophysics, combustion chemistry, and atmospheric chemistry [35–40]. A comprehensive exploration of the kinetics and spectroscopy of HNO will not only verify the utility of ICLAS to measure kinetics, but it will also clarify and expand upon existing information regarding its role in different reaction processes. The $\tilde{A}^1 A'' \leftarrow \tilde{X}^1 A'$ strong electronic transition of HNO is within the spectral range of a Ti:sapphire-based ICLA Spectrometer. The molecule has a large absorption cross-section – requiring only trace amounts of HNO to conduct the necessary experiments ($\sigma > 10^{-17}$

35

cm^{2}molecule^{-1}). In a setup with an occupation ratio of ~35% and a generation time of 500 μs, a detection limit for the total concentration of HNO was roughly 10^7 molecules cm^{-3} by ICLAS.

The spectroscopy of HNO has been measured extensively by both absorption [41–43] and emission methods [44–46]. The molecule has a bent equilibrium geometry and C_s symmetry in its three lowest lying electronic states: $\tilde{X}^1A', \tilde{A}^1A'', a^3A''$. HNO is a slightly asymmetric near prolate rotor; the value of Ray's asymmetry parameter, κ, is -0.988. Only c-type transitions have been observed for the $\tilde{A} \leftarrow \tilde{X}$ transition, indicating the transition moment is perpendicular to the plane of the molecule. The vibrational fundamental modes and their respective frequencies are listed in Table 3.1. Kinetic measurements of HNO were made using the (000) ← (000) band of the $\tilde{A}^1A'' \leftarrow \tilde{X}^1A'$ electronic transition, centered at 13,154.38 cm^{-1}. The rotational parameters are listed in Table 3.2.

Table 3.1: Observed frequencies of the vibrational fundamental modes of the $\tilde{A}^1A''$ and $\tilde{X}^1A'$ states of HNO. All values are reported in cm^{-1} [41, 42]

Mode	$\tilde{A}^1A''$	$\tilde{X}^1A'$
(100) (N-H stretch)	2854.2	2684.0
(010) (N=O stretch)	1420.8	1565.3
(001) (H-N-O bend)	981.2	1500.8

Table 3.2: Rotational constants of the (000) levels of the $\tilde{A}^1A''$ and $\tilde{X}^1A'$ states of HNO. All values are reported in cm^{-1} [41].

Rotational parameter	$\tilde{A}^1A''$	$\tilde{X}^1A'$
A - B	20.88	17.120
B	1.284	1.3593
B - C	0.0828	0.1043
Δ_k	1.93 x 10^{-2}	4.48 x 10^{-3}
Δ_{jk}	206 x 10^{-4}	9.80 x 10^{-5}
Δ_j	3.50 x 10^{-6}	4.05 x 10^{-6}

The distinctive spectroscopic signature of the $\Delta K_a = 1$ subband structure of

the Q and R branches is shown in Figure 3-3. The $^RQ_0(8)$ [1] line at approximately 13168 cm^{-1} was used most often for monitoring HNO kinetics because of the lack of interference from other HNO lines and oxygen transitions, as well as sufficient oxygen lines at nearby frequencies to accurately calibrate the transition (Figure 3.3-4).
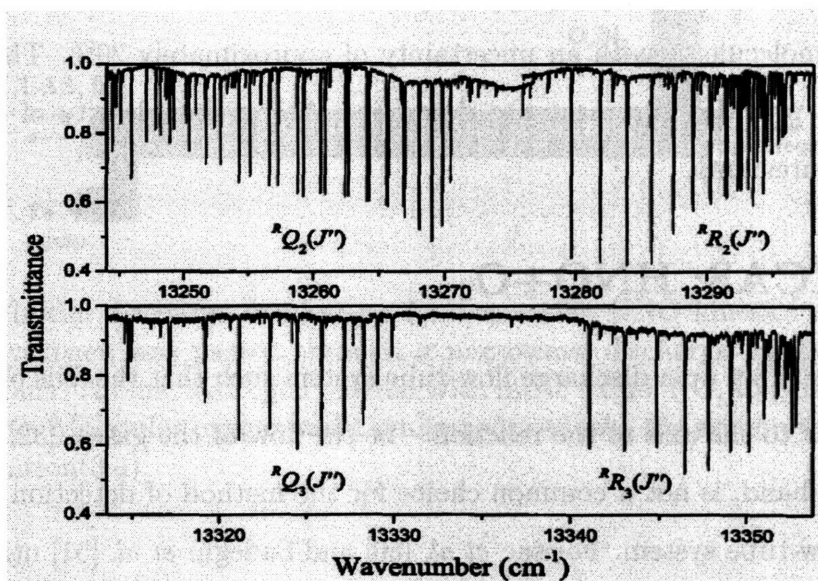
Figure 3-3: Experimental spectrum of the $^RQ_2(J''),^R R_2(J''),^R Q_3(J''),^R R_3(J'')$ sub-branches of the (000)←(000) band of the electronic transition of HNO.
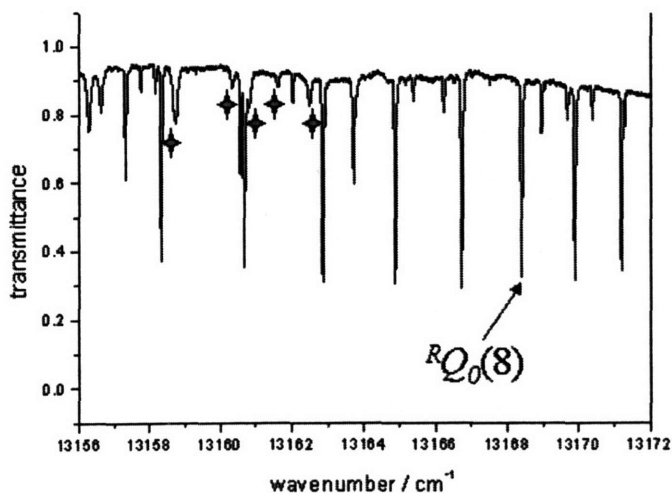
Figure 3-4: ICLAS spectrum of HNO used for kinetics measurements. Transitions marked with a star are oxygen absorption features that are used to frequency calibrate the spectrum.

---

[1]Transitions are labeled as $^{\Delta K}\Delta J_{K''}(J'')$

The absorption cross-section of the $^RR_3(6)$ transition of the (100)$\leftarrow$(000) band of HNO is reported in the literature as 3.3 x 10^{-20} cm^{2}molecule^{-1} at room temperature [47]. Using known Franck-Condon factors [48] and rotational line strength factors calculated using expressions derived by Lide [49], the absorption cross-section of the $^RQ_0(8)$ transition of the (000) $\leftarrow$ (000) band of HNO was calculated to be 4.2 x 10^{-17} cm^{2}molecule^{-1}, with an uncertainty of approximately 20%. This calculated cross-section provided the means to determine the number density of HNO during kinetic measurements.

3.3   KICAS: HNO+O$_2$

It is common to set up a discharge flow-tube system such that the axis of detection is perpendicular to the axis of the reaction – or the flow of the gases [32, 33]. ICLAS, on the other hand, is not a common choice for the method of detection employed in discharge flow-tube system. Foissac et $al.$ [50] and Sadeghi et $al.$ [51] utilized ICLAS to monitor the nitrogen afterglow using a standard flow-tube system. Unfortunately, this method sacrifices the sensitivity that is the hallmark of ICLAS by drastically reducing the cavity occupation ratio. Foissac et $al.$ and Sadeghi et $al.$ [50, 51] had an experimental setup with an occupation ratio of approximately 2%. Employing a setup in which the detection system is parallel to the axis of the flow could potentially increase the ultimate sensitivity of the experiment by a factor of 10.

In an attempt to exploit the sensitivity of the ICLAS instrument, an experiment was designed to measure the following reactions:

$$HNO + O_2 \rightarrow products \tag{3.4}$$

$$HNO + HNO \rightarrow H_2O + N_2O \tag{3.5}$$

$$HNO + wall \rightarrow decay \tag{3.6}$$
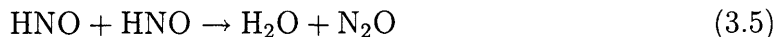
with the axis of detection parallel to the axis of the reaction (Figure 3-5). The optical setup for the ICLA Spectrometer can be found in Chapter 2.

The details of this experiment have been described in the thesis of S. Witonsky [14]
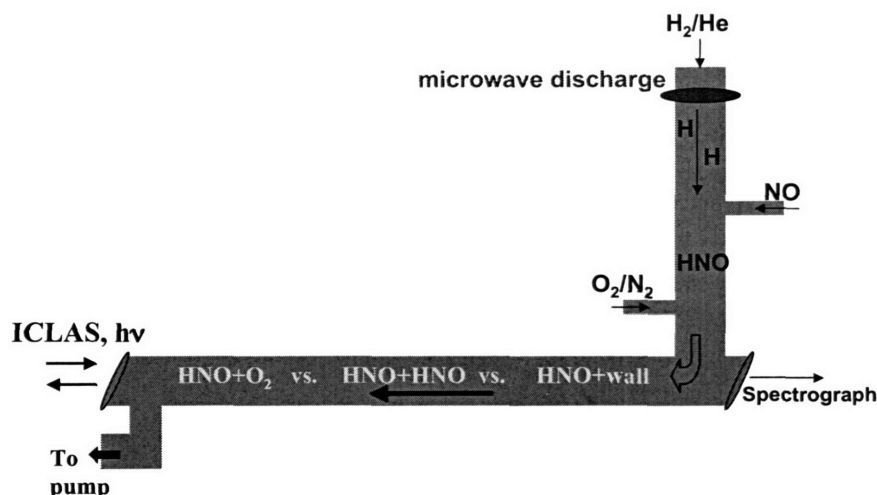
Figure 3-5: Initial discharge flow set-up for measuring HNO kinetics using ICLAS. Molecular hydrogen was passed through a microwave discharge cavity to generate hydrogen atoms. Atomic hydrogen reacted with nitric oxide, NO, to generate nitrosyl hydride, HNO. Molecular oxygen was then introduced into the system to measure the rate for Equation(3.4).

and will only be summarized briefly here. Molecular oxygen was introduced in excess of both hydrogen and nitric oxide, which led to the assumption that $[O_2] >> [HNO]$, and a pseudo-first-order kinetics analysis. The self-reaction of HNO was neglected in the data analysis for several reasons; HNO was present in much smaller concentrations than oxygen, nitric oxide, and the reported rate for the self-reaction indicated a relatively slow reaction ($k_3 = 6.64$ x 10^{-16} cm^{3}molecule^{-1}s^{-1}) [52]. The data analysis required the derivation of a time-integrated measured signal and its relation to the rate constants. This method was used to account for the fact that any given ICLAS measurement in a system in which the flow is parallel to the laser is actually a measurement of the column density (where the absorption cell is the column) of HNO.

Although this experiment was able to provide an upper limit for the reaction rate between HNO and O_2, the results of the measurements were plagued by several experimental flaws that will be explored in more detail here. The following is a list of the reactions originally assumed to be taking place in the axial flow kinetic

measurements:

$$H + NO \rightarrow HNO \qquad (3.7)$$

$$HNO + O_2 \rightarrow products \qquad (3.4)$$

$$HNO + HNO \rightarrow H_2O + N_2O \qquad (3.5)$$

$$HNO + wall \rightarrow decay \qquad (3.6)$$
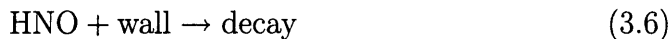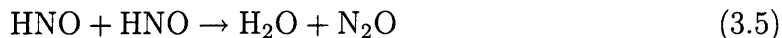
The number density of reactive H-atoms in the flow stream was approximately 10^{13} molecules cm^{-3}. Because NO was in excess ($>10^{15}$ molecules cm^{-3}), the expected concentration of HNO should have been on the order of 10^{13} – assuming complete titration of H-atoms by NO; however, calculations using the absorption cross-section, revealed a discrepancy of two orders of magnitude between the expected (10^{13} molecules cm^{-3}) and the observed (10^{11} molecules cm^{-3}) number density. It was originally anticipated that O_2 was competing with NO for available H-atoms produced in the microwave discharge; however, this does not explain the low concentrations of HNO observed prior to the addition of oxygen to the flow tube. It has since become apparent that a significant amount of NO_2 – as an impurity in the NO stream – was also competing with NO, and eventually O_2 for available H-atoms. The reaction rate between H-atoms and NO_2 ($k = 1.3x10^{-10}cm^3molecule^{-1}s^{-1}$) is much greater than the rate for the three-body reactions involving H-atoms, NO or O_2, and a carrier gas, M. There was no method employed to purify the NO stream of impurities in the HNO-O_2 experiment.

Based on the measured and calculated rates for the HNO + O_2 reaction, the observed decrease in HNO concentration upon the addition of O_2 to the system could not solely be attributed to the presence of oxygen. The sharp decrease in HNO upon addition of oxygen was most likely due to a reaction between H-atoms and O_2 – indicating that the formation reaction, H + NO, was not complete. The attempt to isolate the kinetics between HNO and O_2 was unsuccessful; as such, it was not feasible to report a reaction rate. It is more likely that the reaction scheme for the axial flow kinetic measurements was:

$$H + NO + M \rightarrow HNO + M \tag{3.7}$$

$$H + NO_2 \rightarrow OH + NO \tag{3.8}$$

$$H + O_2 + M \rightarrow HO_2 + M \tag{3.9}$$

$$HNO + O_2 \rightarrow products \tag{3.4}$$

$$HNO + HNO \rightarrow H_2O + N_2O \tag{3.5}$$

$$HNO + wall \rightarrow decay \tag{3.6}$$
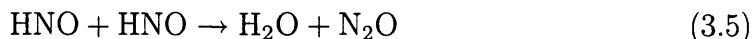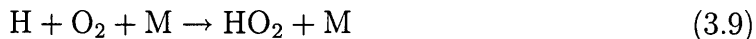
Based on the information presented here, it was apparent that the experimental constraints on the kinetic scheme of interest needed to be improved in order to verify the utility of the KICAS system using a discharge flow tube setup.

3.4   KICAS: H+NO

Basic flow calculations correlated with reported rate constants (Appendix A) indicated that it was unlikely that the reaction between H-atoms and NO was complete in the flow tube. It also became clear – for a number of reasons – that we were not measuring the reaction between HNO and O_2: we had not sufficiently isolated the two species ensuring a 'clean' reaction, there were exceptionally high levels of reactive impurities, we had limited control over the flow speed and the reaction time in the flow tube, and we were attempting to determine a rate that was too slow for us to measure based on the experimental coupling of the flow tube and the ICLAS detection system.

Since the reaction between atomic hydrogen, H, and nitric oxide, NO, was not going to completion, we realized that we could measure the formation of HNO in our system; however, complications arising from the axial set-up suggested that we should attempt measuring the kinetics in a 'traditional' flow tube set up – in which case the detection system (ICLAS) is perpendicular to the flow of the reactants. Although this orientation lowers the detection limit for HNO because of a smaller occupation ratio, HNO is still detectable at approximately 10^9 molecules cm^{-3}.

The following reactions are relevant to the study of HNO formation using ICLAS as the detection method:

$$H + NO + M \xrightarrow{k_1} HNO + M \qquad (3.7)$$

$$H + H + M \xrightarrow{k_2} H_2 + M \qquad (3.10)$$

$$H + HNO \xrightarrow{k_3} H_2 + NO \qquad (3.11)$$

$$HNO + wall \rightarrow decay \qquad (3.6)$$

3.5 Experimental

All measurements were performed with an IntraCavity Laser Absorption Spectrometer in a traveling-wave, ring configuration, furnished by Science Solutions, Inc. A 15-W argon ion laser pumped a Ti:Sapphire laser with a total round trip cavity length of 383 cm. The length of the sampling region was 3.6 cm, resulting in an effective path length of 197 m. A 2.5 m grating spectrograph operated in double-pass mode and order 19 dispersed the laser output at a resolution of 0.013 cm^{-1}, and the spectrally dispersed laser output was recorded with a silicon diode array. Two acousto-optic modulators (AOM) controlled the generation time of the ICLAS laser. The first AOM directed the pump laser onto the Ti:Sapphire gain medium, and the second directed the output of the Ti:Sapphire laser to the spectrograph. In all measurements presented here, a generation time of 70 μsec was used and 100 spectra were averaged.

The apparatus used for measuring the rate constant of HNO formation is shown in Figure 3-6. Experiments were carried out in a Pyrex tube (1.8-cm i.d., 65-cm long) connected to a T-cross that served as the axis for the optical detection system. Helium was used as the main carrier gas (BOC gases., 99.999%). The flow tube gas was pumped by a Welch Duo-seal vacuum pump (500 L min^{-1}). Pressures were measured using a 0-100 Torr MKS Baratron manometer. The flow of the helium carrier gas was monitored using a TubeCube® A7940HA-5 flow meter. The flow of nitric oxide was monitored using a Sierra Instruments Side Trak™ mass flow meter.
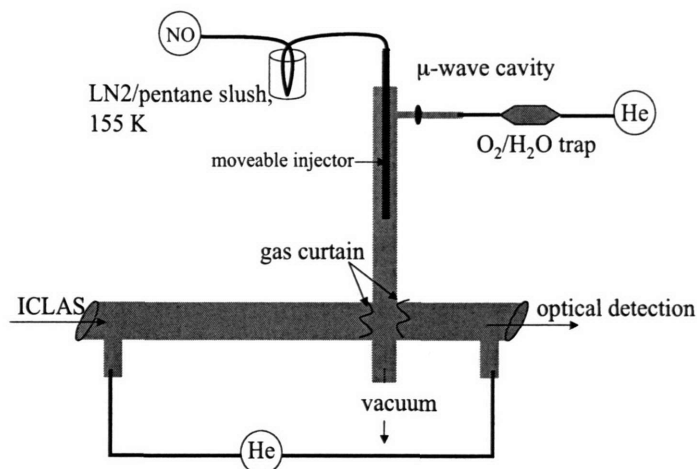
Figure 3-6: Flow apparatus used for measuring HNO formation kinetics using an ICLA Spectrometer.

Hydrogen atoms were injected through a side-arm inlet located at the rear of the flow tube. The excess reactant, NO, was injected through a moveable inlet. The total flow through the injector was kept below 10% of the main carrier gas flow.

Hydrogen, H_2, exists as a 1-ppm impurity in the grade 5.0 helium [53]. The number density of the helium carrier gas is approximately 10^{17} molecules cm^{-3}. This corresponds to a molecular hydrogen number density of $\sim 10^{11}$ molecules cm^{-3}. Atomic hydrogen was generated by passing the helium carrier gas through a microwave discharge. The microwave discharge cavity was cooled with a stream of nitrogen to maximize atomic hydrogen yields [54]. The helium was passed through an OxiClear Disposable Gas Purifier to effectively reduce the concentrations of water and oxygen. The efficiency of the microwave discharge cavity in dissociating molecular hydrogen may vary from day-to-day; however, regardless of potential day-to-day variations, between 1 and 10% of the molecular hydrogen should be atomized to generate H-atoms. There should be approximately 10^9-10^{10} molecules cm^{-3} of atomic hydrogen generated in the flow tube.

To remove NO_2, a purified stream of NO was prepared by passing the gas through a liquid nitrogen and pentane (LN2/pentane) slush cooled to approximately 165 K. The temperature of the LN2/pentane slush was monitored with a Fluke 51 Series II digital thermometer. Only a trace amount of NO_2 is necessary to affect the formation

kinetics of HNO. The rate constant for the reaction between atomic hydrogen and NO_2, Reaction 3.8, is several orders of magnitude greater than Reaction 3.7; so even though NO is present in such excess, NO_2 still competes for hydrogen atoms. Minimizing, and essentially eliminating NO_2 as an impurity is essential. Within the flow tube, the density of NO varied from 1-3 x 10^{16} molecule cm^{-3}.

The ICLAS laser was constructed with Brewster faces to minimize losses. Two large wedge windows, 2-in diameter, 0.5-in thick and a 1-degree wedge, were used for the sample cell. The wedged substrate minimizes the reflection of light back into the cavity, thus avoiding strong fringes. By coupling the flow tube apparatus to the optical detection system of ICLAS, two side arms that branch from the flow tube were unavoidable. This configuration allows for the diffusion of HNO into the side arms. To prevent the diffusion of HNO into the side arms, potentially contaminating the windows and decreasing the sample cell window transmission, a 'gas curtain' of helium was introduced. Eliminating diffusion to the side arms also eliminates the potential for inaccurate measurements of HNO number density as a result of an increased effective path length.

Spectra of the (000)←(000) band of HNO were recorded around 13,165 cm^{-1}. The calculated value for the absorption cross-section of the $^RQ_0(8)$ transition of the (000)←(000) band of HNO was used to determine the number density of HNO (described earlier). Frequency calibration of the spectra was performed using nearby oxygen transitions.

The total flow rate was around 20 SLPM of air, corresponding to a linear flow rate of approximately 5 x 10^3 cm s^{-1}. Measurements were conducted at total pressures of both 13.85 Torr and 24.00 Torr.

3.6   Results and Discussion

The procedure used for determining the reaction rate constant with this method is similar to those commonly used for low-pressure flow tubes [32, 33]; however, the product, rather than the reacting species, was monitored. Nitric oxide and helium were injected at a fixed rate, and their number densities were calculated assuming

complete mixing in the region downstream of the injector. In each reaction, both NO and He (carrier gas=M) were present at concentrations several orders of magnitude greater than the estimated hydrogen atom concentration, creating pseudo-first-order conditions. The plasma discharge was initiated or 'lit' and the position of the moveable injector was varied to generate a series of kinetic curves (Figures 3-7 and 3-8). A non-linear least squares fit was then performed in Microcal Origin®. The data were fit to the following expression:

$$[HNO]_t = \frac{k_{eff}[H]_0}{k_w - k_{eff}} \left(e^{-k_{eff}t} - e^{-k_w t} \right) \tag{3.12}$$

where $k_{eff} = k_1[NO][M]$ (M=He), and $[H]_0$ is the initial concentration of atomic hydrogen in the flow tube in the absence of nitric oxide. Selected experimental conditions and results for the reaction $H+NO+M \rightarrow HNO+M$ are presented in Table 3.3. The initial concentration of atomic hydrogen was not explicitly determined. The input value for $[H]_0$ was assumed to be approximately equal to $[HNO]_{z_{max}}$ where z is the distance between the injector and the ICLAS axis of detection. When z was maximized, neither an increase in background pressure nor an increase in the concentration of NO yielded a higher concentration of HNO. Both of these indicators confirm that $[HNO]_{maximum} \approx [HNO]_{z_{max}}$. It was also assumed that all the [HNO] formed at z_{max} was from the titration of atomic hydrogen with nitric oxide. This assumption leads to $[HNO]_{max} \approx [H]_0$. The number densities calculated for [HNO] are in good agreement with expected values: the concentration of atomic hydrogen generated from the discharge was estimated between 10^9-10^{10} molecules cm^{-3} and the calculated number densities for $[HNO]_{max}$ vary between 3 - 5 x 10^9 molecules cm^{-3}.

Considering potential systematic errors in the measurement of gas flows, pressure, and detector signal, as well as uncertainties in the transition moment and the Franck-Condon factors used to calculate the HNO number density, it is estimated that the rate constant can be determined with an accuracy of ±20%. The stated uncertainties in the values of rate constants reported are based on the accuracy of the fit.

The termolecular rate constant that we report here is (4.3 ± 0.4) x 10^{-32} cm^6 molecule^{-2} s^{-1}. Clyne and Thrush [52] and Miyazaki and Takahashi [55] have de-
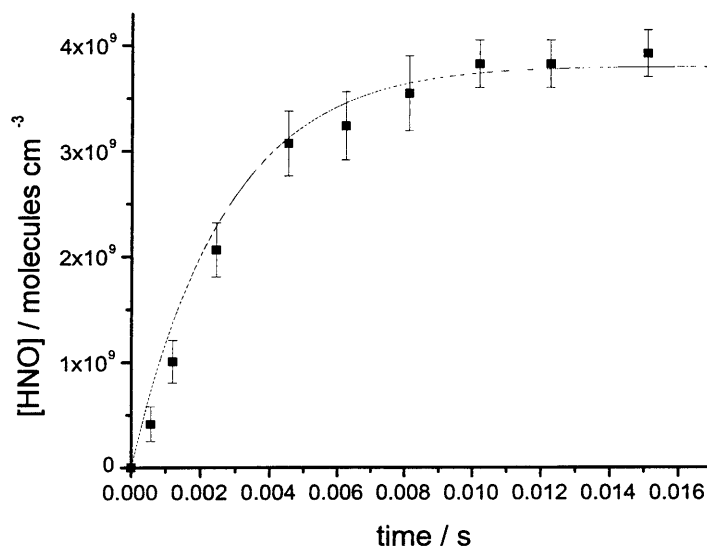
Figure 3-7: A sample kinetics plot at 13.85 Torr with measured HNO number densities and an exponential fit to the data. Error bars represent the mathematical precision of the data point at one standard deviation. The non-linear least squares fit yields a termolecular rate constant of $(3.0 \pm 0.3) \times 10^{-32}$ cm^6 molecule^{-2} s^{-1} and an upper limit for the wall loss rate of (0.6 ± 0.3) s^{-1}. All values are reported with 1σ uncertainty.

termined the value of k_1 by measuring the decrease in HNO emission intensity in a discharge-flow system. They report values of $(1.8 \pm 0.3) \times 10^{-32}$ cm^6 molecule^{-2} s^{-1} and 3.0×10^{-32} cm^6 molecule^{-2}s^{-1}, respectively. These are the only two values in the literature that report the formation of HNO with helium as a carrier gas. The work of Miyazaki and Takahashi requires a complicated data reduction scheme [55], making a comparison of values extremely difficult. Differences in experimental conditions

Table 3.3: Observed termolecular rate constants at 13.85 and 24.00 Torr for the reaction, H+NO+M → HNO+M

Pressure, Torr	velocity, cm s^{-1}	[H]$_o$, x10^9 cm^{-3}	$k_1 \pm \sigma$, 10^{-32} cm^{6}molec^{-2}s^{-1}	$k_w \pm \sigma$, s^{-1}
13.85	5.3	4.15	3.0 ± 0.3	0.6 ± 0.3
	4.9	4.01	4.1 ± 0.4	0.5 ± 0.4
	5.1	3.86	5.7 ± 0.4	0.7 ± 0.2
24.00	5.1	3.92	4.7 ± 0.5	0.7 ± 0.4
	5.2	4.01	4.1 ± 0.4	0.5 ± 0.5

46

Figure 3-8: A sample kinetics plot at 24.00 Torr with measured HNO number densities and an exponential fit to the data. Error bars represent the mathematical precision of the data point at the two standard deviation level. The non-linear least squares fit yields a termolecular rate constant of $(5.7 \pm 0.3) \times 10^{-32}$ cm^6 molecule^{-2} s^{-1} and an upper limit for the wall loss rate of (0.7 ± 0.2) s^{-1}.

between this work and the work of others, primarily Clyne and Thrush [52, 56], are listed here in an effort to explore potential reasons for the slightly different reported rate constants (Table 3.4).

Although similar concentrations of nitric oxide were used in all experiments, the concentration of atomic hydrogen in other flow tubes was approximately 0.5-2% of the total flow [52, 55–57]. In this work, the concentration of atomic hydrogen was reduced to approximately 1 x 10^{-4} % of the total flow. Minimizing the concentration of atomic hydrogen limits the potential for other formation or recombination reactions involving atomic hydrogen. Similarly, limiting the concentration of atomic hydrogen limits the formation of HNO. This minimizes potential losses of HNO via wall reaction, self-reaction, or other successive reactions.

In the KICAS flow tube, the absorption spectrum of HNO is not observed if the nitric oxide stream is not purified by means of the LN2/pentane cold bath. Nitrogen dioxide exists as an impurity in the stream of NO from the cylinder. Nitrogen dioxide

reacts much faster with atomic hydrogen than nitric oxide does. A rigorous purification of the NO stream is essential to measuring the rate parameters of Reactions 3.6 and 3.7 accurately. Clyne and Thrush make a similar observation in that they are unable to detect the 'glow intensity' due to the emission of HNO at increased concentrations of nitrogen dioxide [52].

The work of Clyne and Thrush [52, 56] does not account for any potential wall loss – for both HNO and atomic hydrogen. In our system, it is possible that the wall is acting as a third body and contributing to the stabilization of the electronically excited HNO* molecule, as well as acting as a loss site. Similar recombination phenomena are possible with atomic hydrogen. The only indication of sensitivity to detecting HNO in the literature is given by observations associated with the steady-state concentration of HNO being much less than $0.2*$[NO] [52, 56]. A rough estimate of the detection sensitivity reveals that the HNO was observed in concentrations around 10^{12}-10^{13} molecules cm^{-3}, much higher than the concentrations reported here. A search of the literature reveals very similar detection schemes to that used by Clyne and Thrush's emission intensity measurements. We demonstrated that we could effectively reduce the concentration of HNO such that the focus of our study is limited to the formation of HNO, followed by a slow wall reaction. At higher concentrations of HNO, it is

Table 3.4: Summary of experimental results for the H + NO + M reaction.

k_1, 10^{-32} cm^6 s^{-1}	T, K	pressure, Torr	bath gas	method	Reference
1.8 ± 0.3	293	$0.7 - 3$	He	flow tube, emission	Clyne and Thrush [52]
2.9	300	$4 - 6$	He	flow tube, emission	Miyazaki and Takahashi [55]
4.3 ± 0.4	295	13 - 25	He	flow tube, ICLAS	this work
4.1 ± 0.4	293	0.73	H_2	flow tube, emission	Clyne and Thrush [56]
10.9 ± 1.3	298	$0.4 - 3.0$	SF_6	flow tube, chemiluminescence	Hartley and Thrush [57]
18.8 ± 3.4	298	$0.4 - 3.0$	H_2O	flow tube, chemiluminescence	Hartley and Thrush [57]

unlikely that the slow self-reaction,
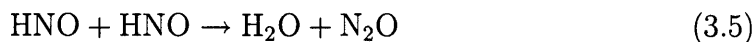
$$HNO + HNO \rightarrow H_2O + N_2O \qquad (3.5)$$

becomes significant; however, it is likely that higher concentrations of HNO will affect the fast reaction,

$$H + HNO \xrightarrow{k_3} H_2 + NO \qquad (3.11)$$

Although Reaction 3.11 is and should be considered in the study by Clyne and Thrush [52], the potential of this reaction to skew the measured concentration of HNO in the ICLAS system is minimized by manipulating the number densities and flows such that [NO]>>[H], [HNO].

The total pressure in the system employed by Clyne and Thrush was 5-10 times lower than the pressures used in this experiment. Under the experimental conditions reported by Clyne and Thrush, it is interesting to note that $k_3 > k_1[M]$. This is not the case in our experiment. By limiting the concentration of atomic hydrogen and the formation of HNO, we were able to observe a steady-state concentration of HNO (at about 6 msec of reaction time). The disadvantage of operating at higher pressures, however, is that it increases the effects of a laminar flow reactor. In most low-pressure flow reactors, the carrier velocity will have a parabolic profile because of laminar flow. As a result, reactants near the center of the absorption cell will travel faster than those near the wall. Calculating rate constants with a correction for laminar flow is described in detail by Brown [58]. The effects of laminar flow corrections to the rate value reported by Clyne and Thrush are most likely negligible because of the very low pressure employed. While there may be some corrections for laminar flow necessary for the rate constant reported here via ICLAS, it is likely that the correction is minor for the following reason: for a typical generation time (80 μs) the ICLAS laser will effectively sample an *average* of the reacting species traveling at an *average* linear flow velocity (5 x 10^3 cm s^{-1}). Imagine a volume of reacting species traveling at a flow velocity with a radial parabolic distribution transverse to the ICLAS laser. The generation time of the ICLAS laser is a long enough 'pulse',

such that this volume will travel between half a centimeter and several centimeters. As the ICLAS laser passes thousands (or more) of times through this volume, it is sampling at many different points along the parabolic distribution of the flow velocity of the volume. It is assumed here that the observed absorption profile is the result of an average of the parabolic profile of the flow velocity (i.e. an average flow velocity) in a laminar flow scenario. As such, it is assumed that the observed number density of the absorbing species is an average profile in the absorbing cell, and that the effects of laminar flow at the pressures employed are minor and are captures in the measurements made by ICLAS.

The wall loss reaction is reported with high uncertainties because of the relatively small effect it has on the simulated curve up to a value of 1 s^{-1}. The upper limit for the rate constant of the wall reaction for this system is reported as 1 s^{-1}, and is most likely in the range 0.2- 0.7 s^{-1}, which is in good agreement with other reported values [31, 59]. At values above 1 s^{-1}, the curve fitting function, Equation 3.12, begins to demonstrate behavior inconsistent with the experimental observations. On the time scale of the experiment (~20 msec), a value greater than 1 s^{-1} would demonstrate a slow, but detectable decline in the concentration of HNO. All of the experimental data at varying pressures observed here supports a slower decay associated with the wall reaction.

3.7   Modeling the reaction in CHEMKIN®

A simplified model can provide qualitative and quantitative support to the accuracy of the experimentally determined reaction rates using the discharge flow tube setup described above. The Aurora application as part of the CHEMKIN® software (distributed by Reaction Design) provides the time-evolution or steady state of a well-mixed reactor. In the applications included in CHEMKIN®, the well-mixed reactor is the best proxy for the discharge flow tube setup used in the KICAS measurements described above. The Aurora application was used to model the series of reactions in the HNO reaction system above to compare computer-generated kinetics curves with the experimental kinetics curves obtained from the KICAS measurements.

The following reactions were used for the chemistry input to the Aurora program:

$$H + NO + M \xrightarrow{k_1} HNO + M \tag{3.7}$$

$$H + H + M \xrightarrow{k_2} H_2 + M \tag{3.10}$$

$$H + HNO \xrightarrow{k_3} H_2 + NO \tag{3.11}$$

$$HNO + wall \rightarrow decay \tag{3.6}$$

The rates used for the reactions were: $k_1 = 4.3 \times 10^{-32}$ cm^{6}molecule^{-2}s^{-1}, $k_2 = 6 \times 10^{-33}$ cm^{6}molecule^{-2}s^{-1}, $k_3 = 1.7 \times 10^{-12}$cm^{3}molecule^{-1} and $k_w = 0.5$ s^{-1}. The application was set up to run under the conditions given in 3.7:

Table 3.5: Selected reaction conditions input for the Aurora application in CHEMKIN®. The number densities are reported in arbitrary units that reflect the relative concentrations of each reactant, based on the concentration of the carrier gas, helium (4×10^{17} molecules cm^{-3}).

temperature	295K
pressure	13.85 / 24 Torr
time	20 msec
[H]	2×10^{-8}
[NO]	3.7×10^{-2}
[H$_2$]	1×10^{-6}
[He]	1

Although absolute number densities for HNO are presented in Figure 3-9, the features of the respective curves are more revealing. Both the shape of the curves and the amount of time necessary to reach [HNO]$_{max}$ are consistent with the experimentally obtained plots. The simple model used here demonstrates good agreement with the KICAS experiment described above.

3.8 Summary

Marked improvements have been made on an experimental setup to employ ICLAS as a method for detection in a discharge flow tube. These improvements have demonstrated the utility of the ICLAS laser, used in conjunction with a flow tube setup

Chemkin Model of the H+NO reaction

H+NO model at 24 Torr

H+NO model at 13.85 Torr
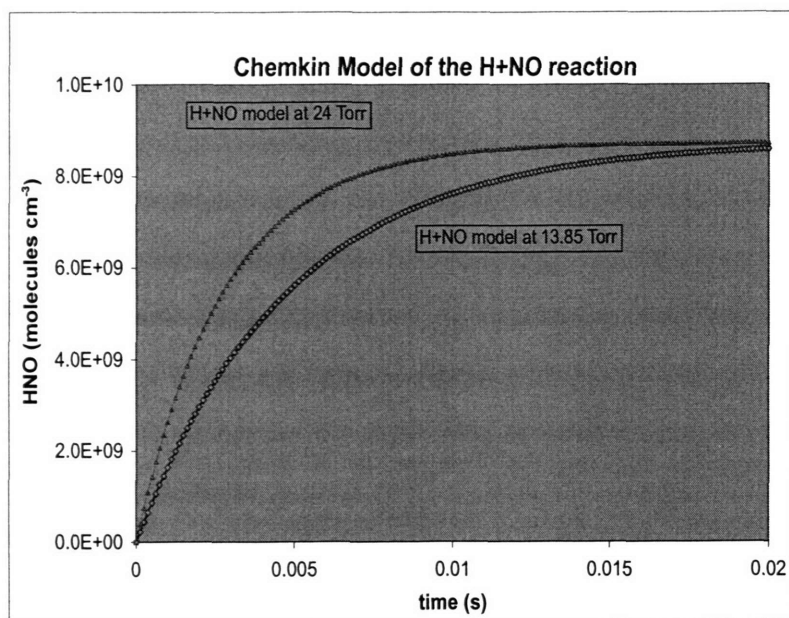
Figure 3-9: The CHEMKIN® output based on a simulated set of reaction kinetics based on the HNO system described above. The steeper rise at the higher pressure is consistent with the experimentally observed characteristics of HNO formation.

by measuring the rate for the reaction between atomic hydrogen in the presence of nitric oxide and a helium carrier gas. The experimental setup employed here and the ones used in the literature are sufficiently different to yield different rate constants. Although the rate constant reported here is slightly higher than values in the literature, it is consistent within expected experimental uncertainties associated with rate parameters. We were able to limit reactive pathways that would inhibit the formation of HNO, and have determined a reaction rate for Reaction 3.7. The sensitivity of ICLAS, coupled with our carefully designed experimental apparatus and reaction conditions suggests that our value is reliable and likely to be closer to the correct value.

A simple model using the Aurora application in the CHEMKIN® software compares extremely well with experimental data collected via the KICAS experiment. A reaction rate constant of $(4.3 \pm 0.4) \times 10^{-32}$ cm^6 molecule^{-2} s^{-1} at 295 K was measured for the reaction:

$$H + NO + M \overset{k_1}{\rightarrow} HNO + M \qquad (3.7)$$

Chapter 4

Extending the Spectral Range of ICLAS: A Proposed Experiment for Detecting the Hydrogen Peroxyl Radical (HO$_2$)

4.1   ICLAS: Limitations

The spectroscopic and kinetics studies ([13, 14, 16], Chapter 3) performed in the Steinfeld Laboratory using the ICLA Spectrometer have each demonstrated the utility of ICLAS as a powerful technique, contributing to the continuously expanding suite of instruments that facilitate laboratory measurements of trace atmospheric species. However, the ICLA Spectrometer has several limitations.

The laser is tunable between 700 and 1000 nm using a combination of highly reflective mirrors and pellicle beam splitter or a prism/slit combination [16]. These tuning techniques, however, will generally only 'drag' the broadband laser operation to around 1000 nm. Both techniques require a rather high pumping power from the argon ion laser (upwards of 6+ W) and they both introduce additional losses within the cavity. There are several very strong absorption features for water vapor and oxygen in the aforementioned spectral range, as evidenced by the stick plots in Figure 4-1. These plots were generated using the HAWKS (Hitran Atmospheric Work Station) platform [60]. Note the particularly strong bands of water centered at 10500 cm^{-1}, 12200 cm^{-1}, and 13750 cm^{-1}, and the aforementioned A band of oxygen. These

features have both positive and negative implications for making spectroscopic and kinetic measurements using ICLAS.
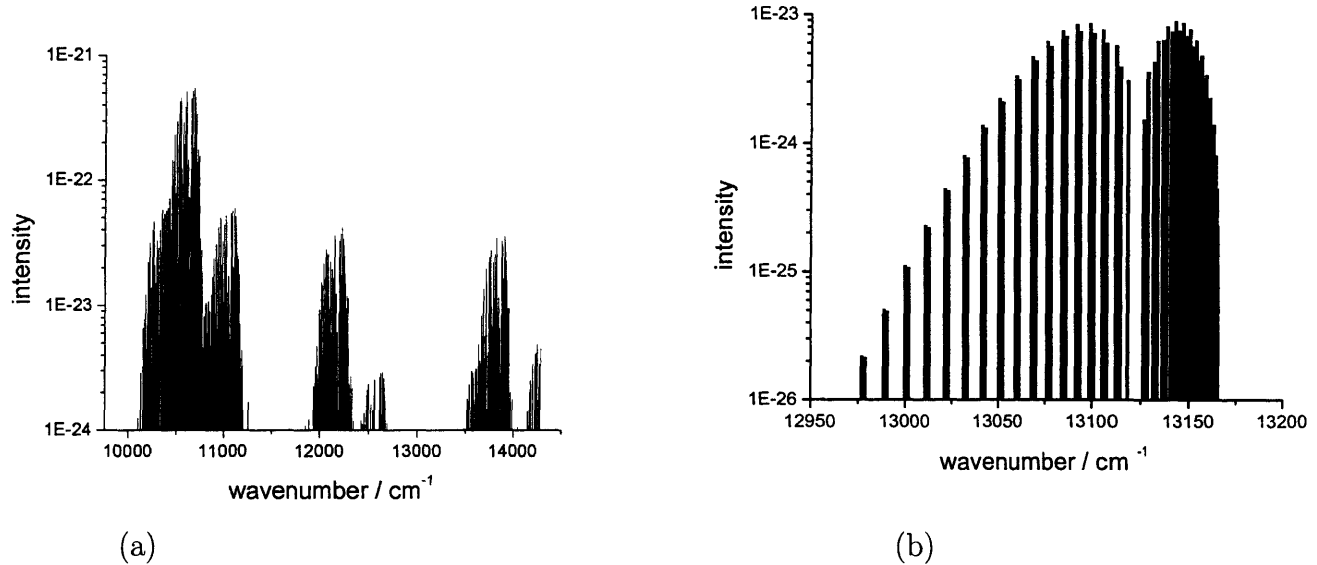
Figure 4-1: Simulation of water vapor (a) absorption bands and the oxygen A band (b) in the spectral range of the ICLA Spectrometer. Simulations were performed using the HITRAN database [60].

The HONO and HNO measurements were made just off the shoulder of a rather significant absorption band of water vapor and oxygen, respectively. Operating near these absorption bands provides a convenient way to calibrate spectra precisely and accurately, above and beyond the simpler, yet effective method of aligning with a HeNe laser. Even though the cavity of the laser is purged with argon, and can significantly reduce the intracavity absorption of both species, the signal of the laser still traverses a rather significant and non-purged path between the output coupler, the spectrograph, and eventually the linear diode array. If one is operating at a wavelength near a weaker absorption band for one of these atmospheric species, then the result is the convenient calibration mentioned above. On the other hand, if one is operating in or near one of these bands, then the intracavity absorption is saturated, and makes it difficult to extract data from weakly absorbing species.

The volume between the output coupler and the spectrograph could be enclosed and purged, however, this would be by no means trivial and has its drawbacks. Be-

cause the laser is often tuned and re-built, the beam often shifts, and even if it shifts slightly, it must be re-aligned into the spectrograph. Enclosing the optics that direct the beam into the spectrograph would make this re-alignment procedure cumbersome. Also, the volume that would end up being enclosed would be roughly 10 times that of the existing purge boxes for the cavity of the laser. Effectively purging these boxes takes approximately 10-12 minutes, and a continuous stream of argon gas. Purging a much larger volume would be both time consuming and expensive.

There are other options besides purging. One can modify the timing sequence of the ICLA Spectrometer in a method termed Correlated Double Sampling. CDS was first demonstrated by Charvat *et al.* [61] and was used by Witonsky to monitor the photofragmentation of acrylonitrile, $H_2=CHCN$ [16]. For CDS, two time slices from one generation pulse of the laser are recorded, and the ratio of the two signals reveals a virtually noiseless spectrum. CDS can be used to extract spectral information in regions where the species of interest overlaps with a dense background spectrum (i.e. water vapor or oxygen). The assumption is that the first spectrum contains concentrations of X_1 and Y_1 for the weakly absorbing species and the strong absorber, respectively. The second spectrum recorded then would have spectral features based on concentrations of X_2 and Y_2, where it is assumed that $Y_2=Y_1$ (and often, but not necessarily, that $X_1 = 0$). A ratio of the two signals, then would leave only the absorption features for the weak absorber with a concentration of X_2-X_1. The utility of this method, however, is dependent on the weaker absorbing species being dynamic; that is, the species of interest must change its concentration between the two sampling periods, otherwise, the proverbial baby is being thrown out with the bath water.

Clearly there are methods to make measurements of trace species using ICLAS, in spite of the experimental difficulties that have been listed above. There are advantages, however, to moving to longer wavelengths in the near infra-red, as this spectral region presents less spectroscopic interference from water vapor and oxygen, and it also moves to regions in which many of the absorption features of trace species are stronger - surely a win-win situation for the experimentalist.

4.2 Experimental Observations of Tuning above 1 μm

To confirm the tuning of the ICLAS laser beyond 1000 nm, an asymmetrically Z-folded standing wave, linear cavity configuration was used (see Figure 4-2). The output of a 15-W argon ion laser pumped a Ti:Sapphire laser, situated between two spherical folding mirrors (FM1 and FM2), with a radius of curvature of 15 cm. The pump beam was focused on the gain medium by a focusing lens (FL) with a 10 cm focal length. The edge-tuner (ET) was placed between the sample cell and the output coupler. The high reflectors and folding mirrors had better than 99.9 % reflectivity. The first mirror in the edge tuner (TM1) (see Figure 2-4) was used at the short wavelength edge of its reflectivity curve. The second mirror (TM2) was greater than 99 % reflective for the wavelength region 940 - 1140 nm. A new output coupler was required, as the height of the output beam varied more than 0.5 in, the diameter of the output coupler used in previous ICLAS arrangements. The output coupler used for tuning had a diameter of 1.5 in, with a 3 degree wedged substrate, and had a reflectivity of 99 %. The tuning of the laser from 960 to 1040 nm was confirmed using a diffraction
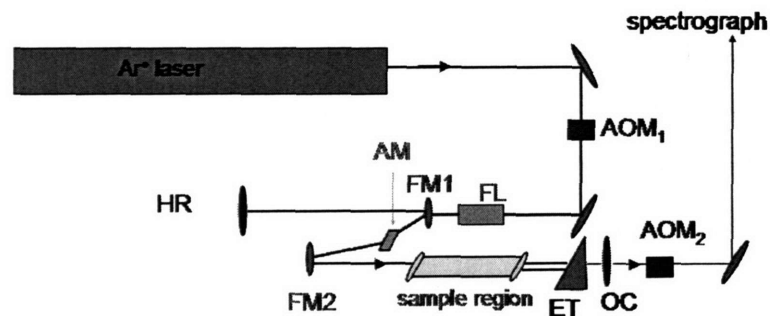
Figure 4-2: Standing-wave, linear cavity configuration of an IntraCavity Laser Absorption Spectrometer, with the novel edge-tuner (ET) in place.

grating and the output of the argon ion laser that is coupled with the Ti:sapphire laser. The broadband lasing of the Ti:sapphire laser was observed, between the 7th and 9th orders of diffraction of the argon ion line of 514.5 nm, near the 8th order of diffraction at 1029 nm. Using an infrared camera and the diffraction grating, the edges of the broadband spectral range were marked. Using the relationship defined

56

by Bragg's diffraction

$$n\lambda = 2d\sin\theta, \tag{4.1}$$

where n is the order of diffraction, d is the distance between scattering centers (or grooves on the grating) and θ is the angle of diffraction, the spectral range accessible using the edge-tuner was determined.

Although the extension of the spectral range for ICLAS with the edge-tuner was only 40 nm, this marks a significant benefit to the user. Figure 4-1 shows the very strong absorption band of water, near 10000 cm^{-1} (or 1 μm). Moving to longer wavelengths away from this band provides much more flexibility to resolve spectroscopic features of molecules with transitions falling in this range. Of particular interest is the hydroperoxyl radical. We have predicted that the 003-000 band of the $\tilde{A}^2A' - \tilde{X}^2A''$ electronic transition of the hydroperoxyl radical can measured with ICLAS at 1024 nm.

4.3 Introduction to HO$_2$ Spectroscopy

The hydroperoxyl radical, HO$_2$, is an important intermediate in both atmospheric and combustion chemistry. The spectroscopy of the radical has been studied extensively with the hope of developing sensitive methods for detecting trace levels of the species in the atmosphere and in laboratory experiments [62–74]. The radical is also of particular spectroscopic interest because it is a prototypically light, asymmetric top molecule. The near-infrared spectrum of HO$_2$ has been studied extensively using emission spectroscopy[62–66, 71], but not as much by absorption techniques [67, 68]; there are few high-resolution studies of the near-infrared absorption spectra. Historically, HO$_2$ transitions in the IR have been difficult to measure by absorption techniques because of the weak oscillator strength (the absorption cross-section, σ, for HO$_2$ in this region is about 10^{-21} cm^{2}molecule^{-1}) and because of the spectral region in which it is located.

The HO$_2$ molecule has a bent equilibrium geometry and C$_s$ symmetry. It is a slightly asymmetric, near prolate rotor ($\kappa \sim -10^{-3}$). Only c-type transitions have

Table 4.1: Observed fundamental frequencies of the vibrational fundamental modes of the $\tilde{X}^2A''$ state of HO_2 (cm^{-1}) [64].

Mode	$\tilde{X}^2A''$
100, OO$\leftrightarrow$ H	3436.2
010, O-O-H bend	1391.8
001, O$\leftrightarrow$ OH	1097.6

Table 4.2: Rotation and spin-rotation parameters for the 000 level of the $\tilde{X}^2A''$ and $\tilde{A}^2A'$ states of HO_2 (cm^{-1}) [64].

constant	$\tilde{X}^2A''$	$\tilde{A}^2A'$
A	20.356	20.486
B	1.118	1.021
C	1.056	0.968
Δ_N	3.8 x 10^{-6}	4.1 x 10^{-6}
Δ_{NK}	1.149 x 10^{-4}	1.386 x 10^{-4}
Δ_k	4.122 x 10^{-3}	4.868 x 10^{-4}
Δ_{SK}	7.893 x 10^{-4}	-1.139 x 10^{-3}
ε_{aa}	-1.653	1.911
ε_{bb}	-0.0141	0.00234
ε_{cc}	2.918 x 10-4	-9.871 x 10^{-3}
$\varepsilon_{ab} + \varepsilon_{ba}$	-0.01297	–

been observed for the radical. The ground state of HO_2, $\tilde{X}^2A''$, 000 has been studied with a variety of high-resolution techniques including millimeter-wave and microwave spectroscopy. The vibrational fundamental modes and their frequencies are listed in Table 4.1. The lowest excited state of HO_2 was experimentally observed by (low-resolution) absorption and emission spectra of the $\tilde{A}^2A' - \tilde{X}^2A''$ transition in the near-infrared region by Hunziker and Wendt [67] and Becker, et $al.$ [62], respectively. Fink and Ramsay later confirmed that the $\tilde{A}^2A'$ state is the only stable excited electronic state of the molecule [64]. The rotation and spin-rotation parameters for the 000 level of the $\tilde{X}^2A''$ and the $\tilde{A}^2A'$ states are listed in Table 4.2.

Fink and Ramsay observed that the 000-000 and the 001-000 bands of the $\tilde{A}^2A' - \tilde{X}^2A''$ transitions at 1.43 μm and 1.26 μm fall into "atmospheric windows" and that long-pass absorption measurements were possible with InGaAsP or InGaAs diode lasers [64]. Although both of these transitions are slightly outside the spectral range

of the ICLAS system that is set up at MIT, this observation regarding absorption measurements using multi-pass techniques is relevant to the 003-000 and 004-000 transitions in the near infrared. The spectral range of the ICLAS system at MIT is limited by the lasing medium, Ti:sapphire, and the silicon diode array detector. Neither the Ti:sapphire crystal nor the diode array detector are capable of operating beyond 1.1 μm. The 003-000 and 004-000 transitions are at 1.024 μm and 0.945 μm, respectively. Both regions are accessible via ICLAS, with the former requiring additional tuning elements (as described in Section 4.1 above). Using the same rotational and spin-rotation constants for the $\nu_3' = 3$ excited electronic state of HO_2 as the $\nu_3' = 0$ state (see Table 4.2), the spectrum of the 003-000 transition was simulated using SpecView14, as seen in Figure 4-3.
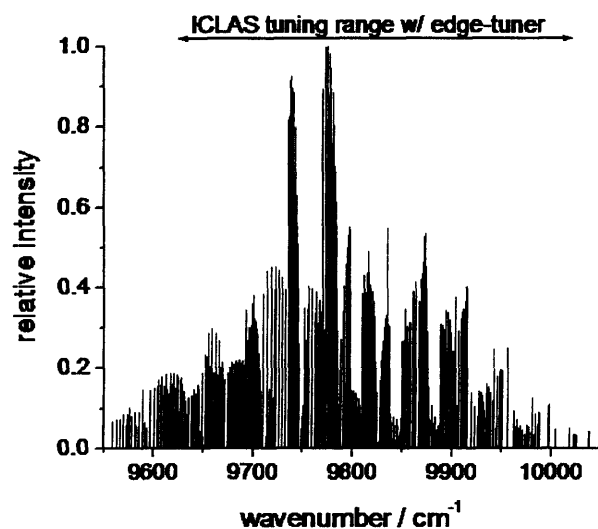
Figure 4-3: Simulation of the 003-000 band of the $\tilde{A}^2 A' - \tilde{X}^2 A''$ electronic transition centered at 9765 cm^{-1}. The simulation is based on the rotational constants [64] listed in Table 4.2. The arrow above the simulated spectrum represents the tuning range of the edge-tuner described above.

Optimistically, an ICLAS experiment could be designed to measure the 004-000 band at 0.945 μm; however, the strong absorption band of water (Figure 4-1) in this same region precludes any static measurements of this band. One could employ the CDS technique described briefly above; however, it would first be useful to understand some of the basic spectroscopic features of the radical in this region, before designing

an experiment with potentially complicated time-resolved measurements.

The situation presented here is an excellent example of some of the aforementioned limitations of ICLAS: interference from water vapor; potentially complicated experimental design (CDS); the lack of feasibility of purging the system to reduce absorption signal of strong absorber; and the limited tuning capabilities provided by the pellicle beam-splitter and the prism/slit combination.

4.4   Proposed Experiment for Detecting HO_2

There are no high-resolution spectroscopic studies of HO_2 in the near infrared. Based on Fink and Ramsay's detection of the 000-000 and 001-000 bands of the $\tilde{A}^2 A' - \tilde{X}^2 A''$ electronic transition [64], the absorption cross section, σ, of the 003-000 transition is estimated to be 4 x 10^{-21} cm^{2}molecule^{-1}, for the entire band. Using expressions derived by Lide [49] for estimating rotational line strengths in slightly asymmetric rotors, it is estimated that the highest populated rotational line will have an absorption cross section of 5×10^{-23} cm^{2}molecule^{-1}. Experimentally, an appropriately designed sample cell can provide an occupation ratio of 50 %; a generation time of 100 ms in this arrangement would provide an effective path length of 1.5 x 10^9 cm (15000 km). There are several methods for generating the hydroperoxyl radical: addition of atomic hydrogen (generated from a microwave discharge of molecular hydrogen) to oxygen in the presence of a third body; photolysis of chlorine gas (308 nm) in the presence of methanol and oxygen [75]; and the addition of fluorine atoms (generated from a microwave discharge of molecular fluorine) to hydrogen peroxide [76]. Each of these techniques generates HO_2 with average concentrations ranging from 1 - 80 x 10^{12} molecules cm^{-3}. It is important to limit the residence time in the sample cell to reduce the loss of HO_2 by self-reaction. Similarly, it is advantageous to coat the sample cell walls with a halocarbon wax to prevent wall loss.

Using the parameters described above for the absorption cross section (σ), effective path length (l_{eff}), and number density of the absorber (N), it is estimated that the most populated rotational levels (and strongest rotational lines) of the 003-000 band of the $\tilde{A}^2 A' - \tilde{X}^2 A''$ electronic transition of the hydroperoxyl radical will have

60

an absorbance ranging from 5-60 %. The absorbance is reported with such a large range for several reasons. Firstly, the number density may vary, depending on the efficiency of generating the radical. For instance, if using a microwave discharge, it has been noted (Chaper 3) that the efficiency of a discharge is not constant. Secondly, the generation time of the laser may vary for the experiment, depending on the performance of the edge-tuner in the traveling wave, ring-configuration. Understanding of the operation of a ring solid state laser with the edge-tuner is not yet complete; it has been suggested that a new structure of unknown origin may appear in the envelope of the spectrum for long generation times [23]. Finally, the estimates for the absorption cross-section of the strongest and most populated rotational lines have an uncertainty of 50 %.

If detection of the hydroperoxyl radical is achieved via ICLAS, it would be worthwhile to attempt to conduct kinetic measurements of the self-reaction, as the uncertainty of the reported value[35] is significant:

$$k = \left[(2.1 \pm 1.6)\text{x}10^{-10}\exp[(-5051 \pm 772)/\text{T}]\right] + (1.8 \pm 0.2)\text{x}10^{-13}\exp[885/T] \qquad (4.2)$$

There are bimolecular and termolecular pathways for the reaction, with the assumption that water vapor enhances the reaction. A water-hydroperoxyl radical complex was proposed [77], and supported by theory [78] and experiment [76]; however, it has not been directly detected. Perhaps, with ICLAS, it would be possible to clarify the reaction pathways for the self reaction of hydroperoxyl radical in the presence of water vapor, and, depending on the spectral features and resolution, detect the proposed water-radical complex. If there is significant detection of the higher rotational levels of the 003-000 transition of the hydroperoxyl radical, then changes in the spectrum in the presence of water vapor may shed light on the spectroscopy of the complex. It is anticipated that if the complex is indeed stable and detectable via ICLAS, then the line intensities of the rotational levels should decrease; however, sufficient sensitivity and resolution of these rotational levels are required.

4.5 Summary

Like any method, ICLAS has its strengths and weaknesses. The ICLA Spectrometer in the Steinfeld Laboratory at MIT operating with a Ti:Sapphire lasing medium has been modified to make measurements slightly beyond 1 μm. We have demonstrated the tuning capabilities of a novel edge-tuner between 960-1040 nm. The extension of the spectral range of the ICLAS system provides the instrument with even more potential to measure the spectroscopy and kinetics of a variety of weakly absorbing species, particularly HO_2, that were previously either undetectable, or experimentally challenging to measure.

A combination of previous low-resolution measurements, a simulation of the 003-000 transition, and carefully designed experimental conditions reveal that it is likely that one could detect HO_2 via ICLAS. Further spectroscopic and kinetic studies using ICLAS and the edge tuner have been suggested, with an emphasis on the hydroperoxyl radical, HO_2.

Chapter 5

Modeling OH and HO$_2$ in the Mexico City Metropolitan Area (MCMA)

5.1 Introduction

5.1.1 HO$_X$ Chemistry

The hydroxyl radical, OH, and the hydroperoxyl radical, HO$_2$, play significant roles in many of the chemical processes in the atmosphere, including ozone formation, aerosol formation, and acid rain. The initial work of Weinstock [79] and Levy [80] demonstrated that photochemically generated radicals – HO$_X$ (OH and HO$_2$) and RO$_X$ (HO$_2$+RO$_2$) – are a major part of understanding tropospheric chemistry. The OH radical is the atmosphere's most important oxidizer and cleansing agent, while the HO$_2$ radical is a major reactive component in the process that leads to the formation of tropospheric ozone. Studying the processes of both radicals is essential to understanding the general oxidative capacity of the atmosphere. Because these radicals initiate and participate in an overwhelming majority of the atmosphere's chemical pathways, it is essential that we understand the factors that influence their production, recycling and removal.

Figure 5-1 shows an outline of the HO$_X$ cycles that will be discussed in greater detail in this Chapter. The photolysis of nitrous acid (HONO), nitric acid (HNO$_3$), and ozone (O$_3$) are the primary sources of OH radicals in the urban troposphere. The photolysis of O$_3$ generates an excited oxygen atom, O(^{1}D), which reacts with

water to generate two OH molecules. The photolysis of aldehydes in the presence of NO is also an important source of OH radicals, as the hydroperoxyl radical is rapidly cycled to OH at high NO_x concentrations. OH radicals are also generated when organic peroxides (byproducts of VOC oxidation processes) are photolysed. The photolysis of formaldehyde (HCHO) and other organic aldehydes (RCHO) are the primary sources of HO_2 formation.

Radical recycling or propagation leads to interconversion between the OH and HO_2 species. The OH molecule is directly converted to an HO_2 molecule when reacting with carbon monoxide (CO), O_3, hydrogen (H_2) or a nitrate radical (NO_3). The OH molecule initiates a variety of oxidation pathways when it reacts with a volatile organic compound (VOC). The oxygenated VOC (ox-VOC) react with another OH molecule to generate an HO_2 molecule.

Organic peroxyl radicals (RO_2) are formed after the reaction between OH and a VOC in the presence of oxygen; they eventually cycle back into HO_2 molecules in the presence of nitric oxide (NO) and NO_3. This process, coupled with the cycling of HO_2 into OH via reaction with NO, NO_3 and O_3, spurs the formation of tropospheric ozone in two ways: 1) the NO to nitrogen dioxide (NO_2) conversion leads to ozone formation ($O_2+O(^3P)\rightarrow O_3$) after the NO_2 molecule is photolyzed ($NO_2+h\nu \rightarrow NO+O(^3P)$) in the presence of oxygen, and 2) it recycles the OH molecule, re-initiating the oxidation of VOCs.

The dominant sink for OH radicals is the reaction with NO_2, forming HNO_3. At night, the reaction between OH and NO is another pathway for removal of the radical. In cleaner air, OH will react with HO_2 for removal of both species. The HO_2 radical will self-react to form hydrogen peroxide, H_2O_2, or with organic peroxyl radicals, RO_2, to from organic peroxides, ROOH. Other sinks, such as deposition and heterogeneous chemistry in cloud drops and aerosols have been suggested, and is currently not well established [81].
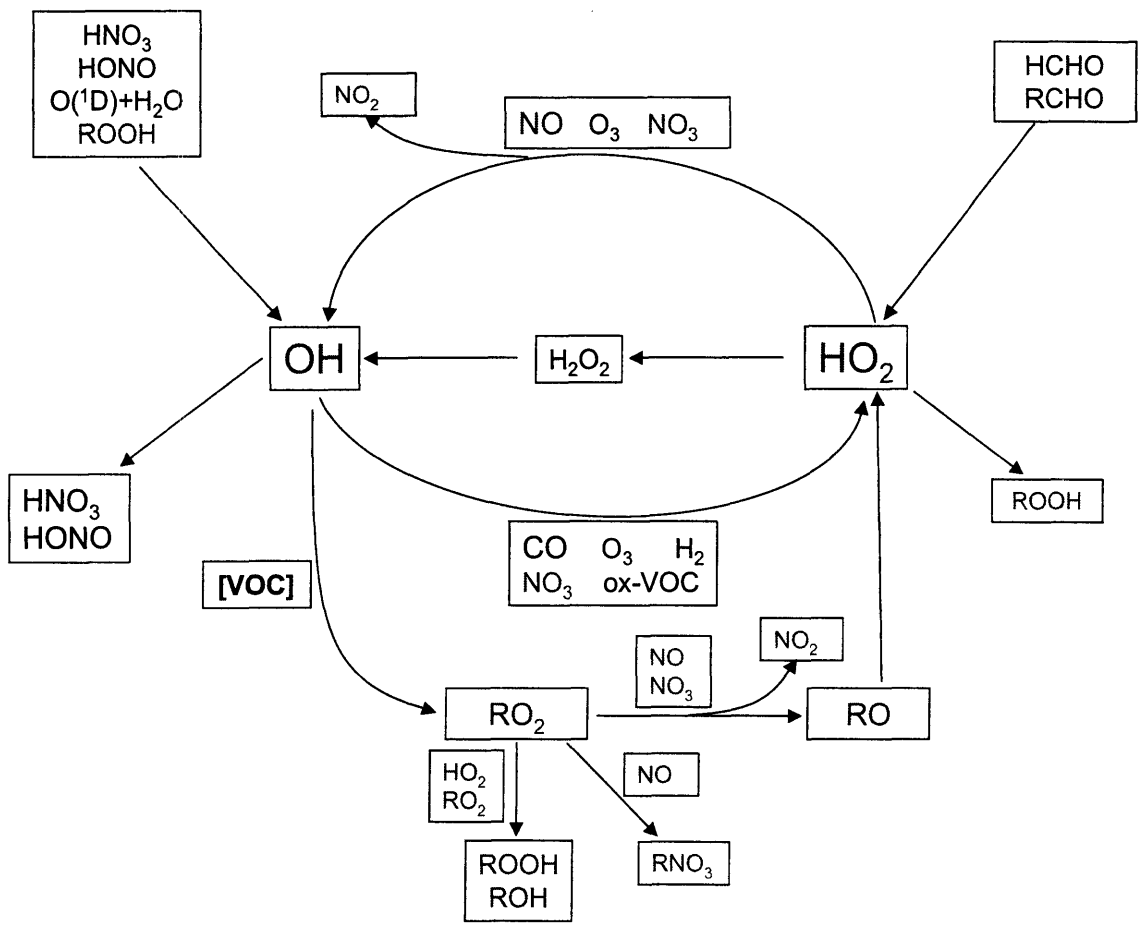
Figure 5-1: Simplified reaction scheme in the troposphere for OH and HO_2 radicals.

5.1.2 Measuring and Modeling HOx chemistry in the troposphere

The behavior of OH and HO_2 under urban tropospheric conditions has only recently been studied. Although there are many studies that combine OH and HO_2 measurements and modeling, there have been only a few field campaigns with HO_X measurements in a polluted urban atmosphere. Direct detection of the species has been difficult because they are both highly reactive and are present at low concentrations. Advances in the suite of techniques capable of measuring OH and HO_2, as well as other atmospheric constituents, has facilitated an increased number of studies designed to improve our understanding of tropospheric chemistry. Popular methods for detecting OH and HO_2 radicals include laser-induced fluorescence (LIF) [82, 83], differential optical absorption spectroscopy (DOAS)[84], and chemical ionization mass spectrometry (CIMS)[85]. Measurements of HOx chemistry in an urban atmosphere have been made in London [86] and Birnginham UK [87]; Los Angeles, CA [88]; Nashville, TN [89]; Houston, TX [90]; New York, NY[91]; and near Berlin, Germany [92] [1]. Only the more recent studies have had simultaneous measurements of HO_X and other constituents that are necessary to constrain models for comparisons to measurements.

In the Los Angeles Free Radical Experiment (LAFRE), George *et al.* used their own numerical integration program, PAMOL, and a chemical reaction mechanism, CAL [93], to model HOx chemistry. They were able to constrain their mechanism with measured values for HO_X, NO_X, O_3, peroxyacetyl nitrate (PAN), H_2O_2, HONO, HNO_3, 100+ VOCs, and 9 carbonyl species. The CAL mechanism lumps hydrocarbons according to their reactivity into about a half dozen different surrogate species. While the authors had success reproducing measured OH values, they found that the CAL mechanism incorrectly predicted HO_2 concentrations in the Los Angeles atmosphere due to incomplete HO_2/RO_2 chemistry, overprediction of HONO formation, and underprediction of dicarbonyl photolysis and/or radical sources from reactions

---

[1]This refers to a semi-rural/urban site near Berlin, Germany. It is important to note that the highest levels of observed NO were limited to a few ppb_V and that there were strong biogenic influences.

between alkenes and ozone. Four primary recommendations from their study of HOx chemistry were: 1) reduce average times for VOC and carbonyls from the 4-hr averages they employed; 2) an improved check on OH and HO_2 ambient measurements; 3) extend model calculations to other mechanisms; 4) measure aerosol size distribution to assess possible production and loss of radicals through heterogeneous pathways.

In the Southern Oxidants Study (SOS) in Nashville, Tennessee [89], Martinez *et al.* employed a lumped chemical mechanism used elsewhere [94]. They had measurements for a variety of species, including NO_X, NO_y, HCHO, PAN, and many VOCs. In both cases, their model was capable of reproducing the general characteristics of HO_X chemistry; however, at high NO concentrations (a few ppbv) they were unable to model the increased HO_2 concentration. The increase in HO_2 meant that ozone production did not decrease at higher concentrations of NO. They also discovered that their model was lacking with regard to the OH budget, as additional OH sources were required to balance the OH sinks.

As part of the PM2.5 Technology Assessment Characterization Study in New York (PMTACS-NY), Ren *et al.* [91] used the Regional Atmospheric Chemistry Mechanism (RACM) [95]. As in previous studies, they were able to capture the general characteristics of HOx chemistry with their model; however, they could not reproduce HO_2 concentrations at high levels of NO (occurring in the early morning). They also were unable to reproduce the nighttime levels of OH, as their calculated values were significantly lower than the observed values. The authors conclude that further research – in both observations and modeling – was required in the investigation of HOx sources and the rapid cycling between the OH and HO_2 radicals,

In the BERLIner OZone experiment (BERLIOZ), Platt *et al.* [92] employed the Master Chemical Mechanism (MCM) [96], a near-explicit mechanism developed at the University of Leeds (discussed below) to calculate OH, HO_2 and RO_2 radical concentrations with constraints from measured compounds, including NO, NO_2, O_3, PAN, CH_2O, and 71 different hydrocarbons (HC). Their model yielded a good qualitative description of the measured diurnal profiles of OH, HO_2 and RO_2. Both the HO_2 and RO_2 concentrations were quantitatively well described by the model. Unlike other

models mentioned above, they had problems reproducing OH levels at *low* levels of NO_x, which they attributed to an incomplete set of VOC mechanisms. Based on the measurements and modeling from their campaign, the authors suggested that better, and more comprehensive VOC measurements are required with sufficiently high time resolution, improved HCHO and RCHO measurements, and speciated measurements of organic peroxyl radicals, RO_2 as a means to assess the role of VOCs on the radical chemistry and their contribution to photochemical ozone production.

There are several motivations for the development of the box model described here. Generally, as part of the Mexico City Project, it is important to continue improving our understanding of the oxidative capacity of the urban troposphere. The extensive suite of data available from the 2003 MCMA field campaign and recent improvements to the MCM afford a unique opportunity to explore a variety of questions related to HO_x chemistry. In addition to being a potentially valuable contribution to the modeling studies as part of the Mexico City Project, this work is a means to provide tests for the validation of the improved mechanisms in the MCM. Development and improvement of the MCM is an ongoing process that requires continuous testing. According to Saunders *et al.* [97], the mechanism has not been primarily developed as part of work done in conjunction with chamber experiments, and as such, lacks the built-in validation procedures of other mechanisms (see Simonaitis *et al.*[98], for example). Similarly, a detailed analysis of the model's strengths and weaknesses will 'close the loop', so to speak, with feedback to experimentalists (such as users of an instrument like the ICLA Spectrometer) regarding areas or parameters that require more consideration and attention.

The specific aims of this box model development were: 1) to compare observed and modeled values of OH and HO_2 as a means to assess the current understanding of VOC mechanisms related to HO_x chemistry; 2) separate the sources of HO_x radicals as due to primary formation processes or secondary recycling processes resulting from VOC oxidation; 3) determine the role of each type of VOC in recycling of HO_x; and 4) determine modeled concentrations of organic peroxyradicals to complement existing HO_x measurements.

5.2 Description of Box Model

5.2.1 Master Chemical Mechanism (MCM)

The work presented here was performed using the latest version (v3.1) of the near-explicit Master Chemical Mechanism (MCMv3.1) [99, 100]. The MCM was developed at the University of Leeds with the intention of providing researchers with an appropriate modeling tool for understanding gas phase tropospheric chemistry. The mechanism was designed to be flexible and accommodating to understand processes such as ozone formation, reaction intermediate recycling, and other cycles that require detailed chemistry. The mechanism is based on available laboratory data, but it has not been fully tested against field measurements and photoreactor experiments.

The most recent version of the MCM includes the degradation kinetics and oxidation schemes of 135 VOCs, based on mechanisms described by Jenkin and Saunders *et al.* [96, 97, 101]. Most notable in the updated version, is the improved understanding of aromatic schemes using recent studies on atmospheric oxidation [102–110]. The MCMv3.1 is ideal for a range of NOx and VOC emission categories, and as such, is appropriate for use in urban, rural, or remote tropospheric environments. The mechanism's flexibility in its potential applications is matched by the ease with which it is updated as new data becomes available. The version of the code used here includes about 13500 reactions and 4600 chemical species. Figure 5-2 represents a schematic summary of how the kinetic and mechanistic data is compiled into the Master Chemical Mechanism.

5.2.2 FACSIMILE

We used the FACSIMILE [111] software package as our numerical integrator for the box model. The software is specifically designed to handle partial differential equations that are stiff; that is, the system in question may have some solutions that change very rapidly compared to others, or some of the solutions may change rapidly at certain times and slowly at others. While many numerical integrators have difficulty with stiffness, FACSIMILE is well suited to handle these types of problems. The

INITIATION

PHOTOLYSIS
carbonyls
ROOH RC(O)OOH
and RONO$_2$

OH reaction
all VOC and
oxygenated products

NO$_3$ reaction
alkenes   dienes
aldehydes   ethers

O$_3$ reaction
alkenes   dienes
Unsaturated
oxygenated products

OXY (RO)
O$_2$ reaction
decomposition
isomerisation

PEROXY (RO$_2$)
reaction with
NO NO$_2$ NO$_3$
HO$_2$ R'O$_2$

Excited CRIEGEE
(RR'COO$^\#$)
stabilization
decomposition

Stabilized CRIEGEE
(RR'COO)
reaction with
SO$_2$ NO NO$_2$
CO and H$_2$O

Carbonyls PANs
RONO2 ROOH ROH
RC(O)OOH RC(O)OH CO

CO$_2$

Figure 5-2: Tree diagram outlining the processing of chemistry by the Master Chemical Mechanism (Figure provided by Jenkin *et al.* [96]).

complex chemical systems of tropospheric chemistry, including HO_X chemistry, VOC oxidation and degradation, and NO_X chemistry, are stiff systems because of large range of time scales that characterize the kinetics. The user-friendly interface, and its flexibility give FACSIMILE the appropriate characteristics to perform the numerical integration of the detailed chemical mechanisms of the Mexico City Metropolitan Area (MCMA).

5.2.3   Running the box model

The model calculations were performed on a 24-hr basis, and was initialized every 10 minutes with the constrained input parameters listed here, including: inorganics, alkanes, alkenes, aromatics, alcohols & glycols, aldehydes, ketone, esters, ethers & glycol ethers, haldohydrocarbons, miscellaneous VOCs, dilution [2], photolysis rate parameters, and finally, HO_X. The input parameters for the box model discussed here have been categorized, with some minor modifications, based on their treatment by the Master Chemical Mechanism. The description of each set of input parameters includes a brief description of the measurements, and how these measurements were used to effectively constrain the code as a box model that is as representative of the MCMA urban troposphere as the current dataset permits. Unless otherwise noted, data was measured at the site for the National Center of Investigation and Environmental Qualification (CENICA) in Iztaplala, Mexico City. A diurnal average profile of each species measured during the campaign was constructed using all available data. The diurnal profiles were constructed in 10-minute intervals and are presented in the appropriate sections below.

Field measurements of OH and HO_2 provide a unique opportunity to run a series of cases designed to assess MCMv3.1. As part of this assessment, we are able to characterize the sources of uncertainty in the mechanism and make suggestions for validation studies. The primary focus of the work presented in this chapter is on OH and HO_2 chemistry in the troposphere. The box model was run in several different

---

[2]Reactive species in the model that were not measured were effectively diluted using a kinetic rate. This is discussed further in the text.

cases: 1) constrained for all organic and inorganic parameters with the exception of HO_X; 2) constrained for all organic and inorganic parameters with the exception of OH (HO_2 was constrained); 3) constrained for all organic and inorganic parameters with the exception of HO_2 (OH was constrained); 4) all input parameters are constrained. After examining each case as it relates to HO_X chemistry, an example of the utility of the box model is presented by investigating glyoxal formation.

Inorganics

The box model employed here has been constrained for 8 species which have been termed 'inorganic': carbon monoxide (CO), nitric oxide (NO), nitrogen dioxide (NO_2), nitrous acid (HONO), nitric acid (HNO_3), ozone (O_3, sulfur dioxide (SO_2), and methane (CH_4). Although neither CO nor CH_4 are inorganic species, they have been grouped with this list of species because of the role each species plays in the simulation due to their long lifetimes in the atmosphere. CO and CH_4 were measured by open path Fourier Transfer Interferometry by researchers from Chalmers University of Technology, and NO was measured by chemiluminescence by researchers at Universidad Nacional Autonoma de Mexico (UNAM). Data for NO_2, HONO, O_3, and SO_2 all come from the instruments using Differential Optical Absorption Spectroscopy (DOAS) for detection.The HNO_3 measurements are continuous data measured by FTIR at the La Merced site, which may introduce some uncertainty; however, HNO_3 is only a minor source of OH radicals.

Each of the species in this inorganic grouping has continuous real-time measurements that require no scaling and/or estimating. The diurnal profiles of these species are presented in Figures 5-3 and 5-4.

Alkanes

MCMv3.1 includes the degradation and reaction dynamics of 22 alkane species. The model presented here has been constrained for 21 of the 22 alkane species [3]. Of these, 19 are constrained based on measurements and a scaling method (described below),

---

[3]The lone alkane species that was not used was 2,2-dimethylpropane.
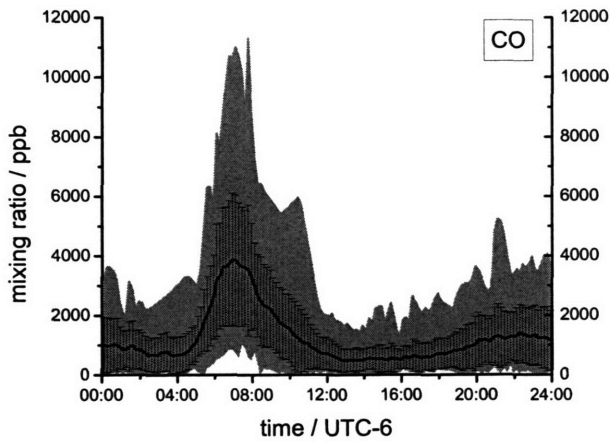
(a)
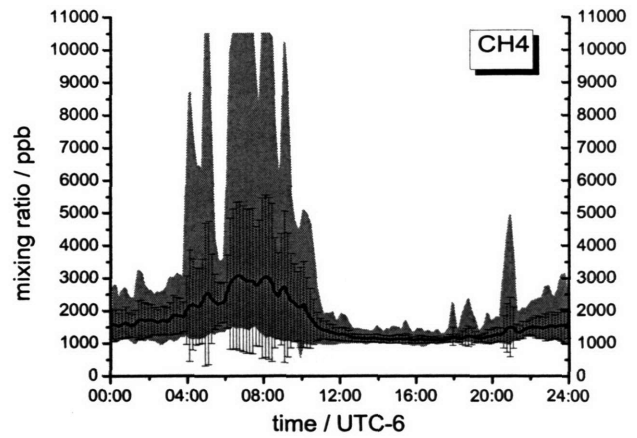
(b)
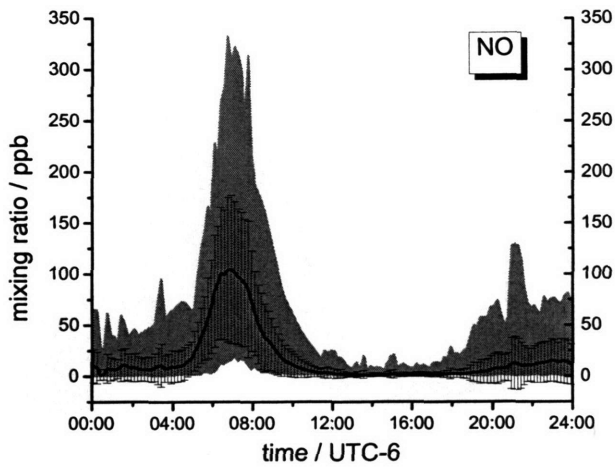
(c)
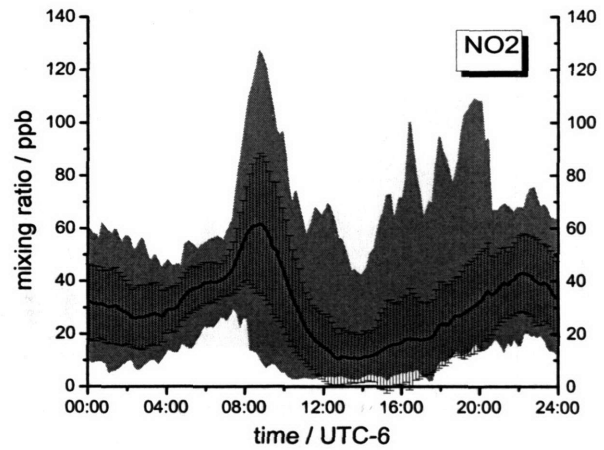
(d)

Figure 5-3: Diurnal profiles of inorganic species measured during the 2003 MCMA field campaign. The lightly shaded values represent the range of data measured. The black line represents the average of the data collected during the campaign with ± 1 standard deviation.
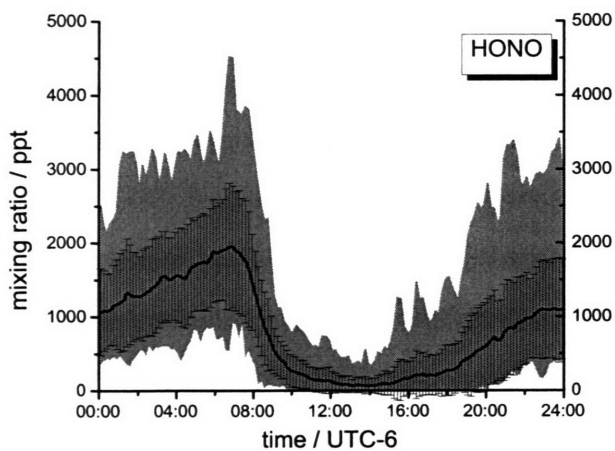
(e)
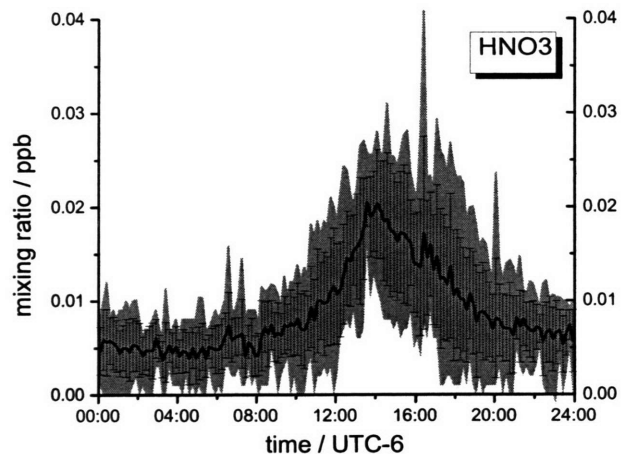
(f)
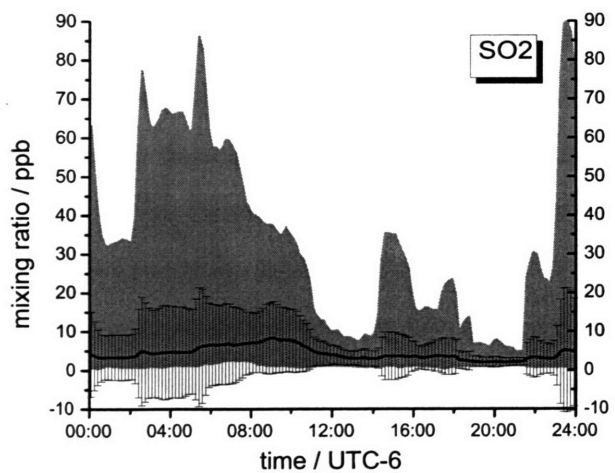
(g)
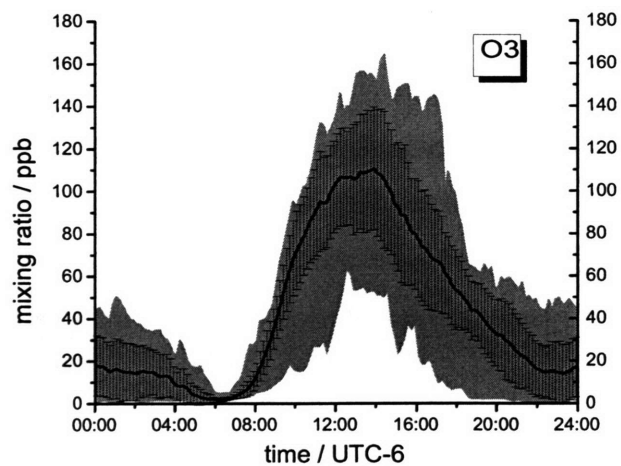
(h)

Figure 5-4: Diurnal profiles of select inorganic species measured during the 2003 MCMA field campaign. The lightly shaded values represent the range of data measured. The black line represents the average of the data collected during the campaign with ±1 standard deviation.

and the other 2 species have been estimated based on available emissions data. (note: Although methane is treated in the MCM with other alkanes, it has been included in the **Inorganics** section above because of its low reactivity, specifically in HO_x chemistry.) The method for constraining the code for these alkanes is described in detail here.

VOCs, including alkanes, were collected via whole air canister sampling and analyzed using a gas chromatograph with flame ionization detection (GC/FID) by researchers at Washington State University (WSU)[112]. Data were provided for the days and times listed in Table 5.1. The alkanes measured by this method were then scaled based on their concentration as a function of the number of C-H stretches in the compound, ppb_{C-H}, relative to the total concentration of alkane species (again, measured in ppb_{C-H}). The ratios of each individual alkane species concentration to the total number of alkanes measured are presented in Figure 5-5.

Table 5.1: Dates and times of VOC data collected by air canister sampling by WSU.

Date	Time
08 April	09:45 - 11:00
09 April	06:00 - 09:00
13 April	11:00 - 12:30
14 April	06:00 - 09:00
27 April	06:00 - 10:00
28 April	06:00 - 13:00
29 April	06:00 - 10:00

While there are only data from 7 days shown in Figure 5-5, it appears that the percent composition of the alkane species shows no significant variation over the range of times, 06:00 - 13:00. Based on these data, an average percent composition is assigned to the 18 alkane species (Table 5.2). The scaling factors for the alkane species that were not measured via the canisters are estimated based on available emissions data [113]; the n-undecane and n-dodecane concentrations are estimated to be 75% and 15% of the n-decane species concentration, respectively. This assumption is based on the percentage of emissions composition that C11 and C12 alkanes represent in non-catalyst gasoline engine exhaust. The speciation is based on the exhaust for
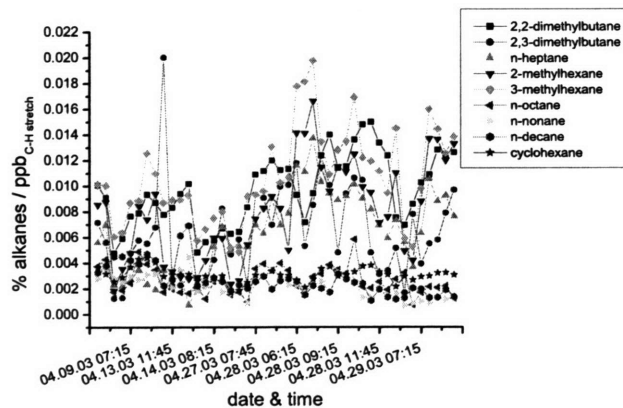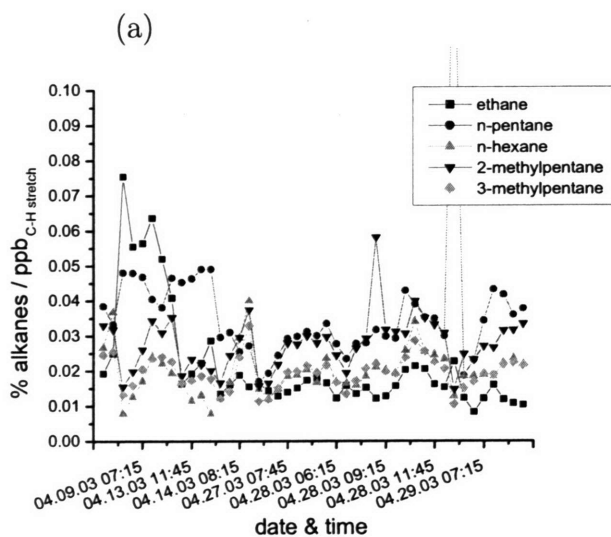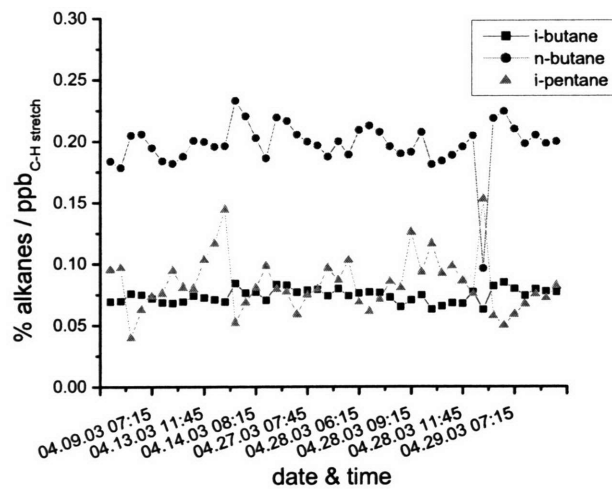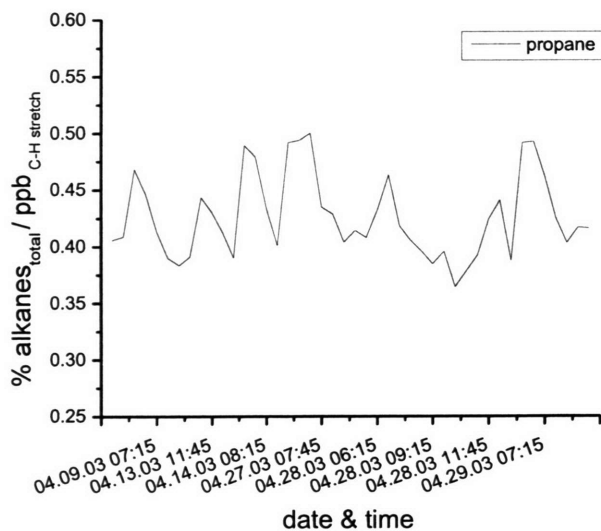
(a)

(b)

(c)

(d)

Figure 5-5: Alkane speciation derived from VOC data collected via air canister sampling by WSU during the 2003 MCMA Field Campaign.

gasoline-powered light-duty vehicles without catalytic converters [113].

Table 5.2: Alkane scaling factors used in the box model, calculated as a function of measured mixing ratios scaled by number of C-H stretches. The last 2 compounds are scaled based on emissions factors [113], and are fit to the general alkane profile.

alkane species	scaling factor ($\pm\sigma$) x 10^{-2}
ethane	2.18 (1.53)
propane	42.6 (3.66)
i-butane	7.40 (0.56)
n-butane	19.7 (1.99)
i-pentane	8.37 (2.30)
n-pentane	3.69 (1.99)
n-hexane	1.98 (0.67)
2-methylpentane	2.77 (0.79)
3-methylpentane	1.95 (0.47)
2,2-dimethylbutane	0.97 (0.28)
2,3-dimethylbutane	0.64 (0.37)
n-heptane	0.64 (0.31)
2-methylhexane	0.80 (0.39)
3-methylhexane	1.10 (0.36)
n-octane	0.26 (0.11)
n-nonane	0.22 (0.09)
n-decane	0.27 (0.13)
cyclohexane	0.31 (0.06)
n-undecane	0.20
n-dodecane	0.04

We use the factors listed in Table 5.2 to scale data collected using an open path FTIR instrument operated by researchers from Chalmers at the CENICA site during the field campaign. The FTIR data are provided in a measurement of butane equivalents; the total number of C-H stretches observed via the FTIR data is scaled to butane (10 C-H stretches). There are 4 days (13, 14, 27, 28 April) of data overlap between the canister and FTIR measurements for alkanes (Figure 5-6). The agreement between the two techniques is good, in both similar concentrations and observable diurnal profiles from the data.
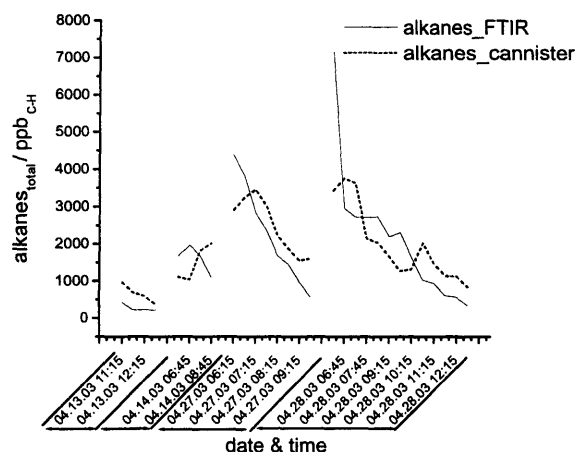
Figure 5-6: A comparison of two types of measurements for alkanes during the 2003 MCMA field campaign: FTIR and air canister sampling. Both measurements have been scaled using a volume mixing ratio and the number of total C-H stretches. The raw FTIR data were provided by researchers from UNAM and the raw data from air canister sampling were provided by researchers from WSU.

Alkenes

MCMv3.1 includes the degradation kinetics and reaction dynamics for 16 alkene species and 2 dialkene species. The model presented here has been constrained for all of these alkenes; 12 of them have been constrained based on measurements and a scaling method (described below). The remaining 6 species have been scaled based on available emissions data.

A combination of the canister data and a real-time continuous Fast Olefin Sensor (FOS), operated by researchers at WSU, was used to determine the appropriate scaling for the alkene species. The FOS instrument detects olefins based on the chemiluminescent reaction between alkenes and ozone. The detector responds with different sensitivity to a variety of olefins [114]. Potential instrumentation errors exist because there are reactions between ozone and other trace gases that could potentially interfere with the signal. The instrument was calibrated using propene.

For this box model, a generic FOS signal was plotted against the alkene data from the canister data (Figure 5-7) assuming that an equal (unity) response of the FOS towards different olefin species. The agreement between the available data is excellent;

78

the matching profiles between the two types of measurements is even more noteworthy when one considers the relatively wide range of concentrations measured. Note the different scales between the olefin sensor signal and the ppb$_C$ measurement from the canisters. To determine the appropriate alkene scaling factors, the overlapping data from the canister were divided by the data from the FOS instrument and averaged over the entire range of data. These scaling factors are reported in Table 5.3 with a 1σ. The scaling factors listed in Table 5.3 are used with the FOS data to generate input parameters for the alkenes.

The other scaling factors for alkenes included in the box model are determined using speciation profiles for exhaust and fuel evaporative emissions [113], and are included in Table 5.3 . It is assumed that the primary source of these alkenes is from engine exhuast emissions from light duty vehicles without catalytic converters.

Table 5.3: Scaling factors for alkene species, as determined by comparison between data obtained from air canister sampling and a Fast Olefin Sensor. Both sets of data are complements of the research group at WSU. The alkene species separated from the rest have been estimated based on available emissions data[113].

alkene species	scaling factor ($\pm\sigma$) x 10^{-2}
ethene	80 (3.2)
propene	44 (1.7)
2-methylpropene	31 (1.4)
c-2-butene	4.5 (1.9)
t-2-butene	5.0 (4.8)
1-pentene	5.9 (0.2)
c-2-pentene	2.8 (1.3)
t-2-pentene	5.0 (3.0)
2-methyl-1-butene	12 (2.2)
2-methyl-2-butene	8.5 (7.6)
1,3-butadiene	4.8 (0.3)
isoprene	3.9 (0.4)
1-butene	15
3-methyl-1-butene	5.9
1-hexene	2.1
c-2-hexene	2.1
t-2-hexene	3.8
2,3-dimethyl-2-butene	2.1
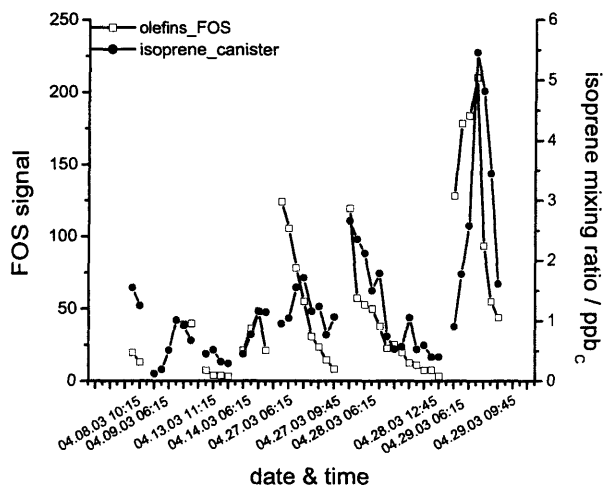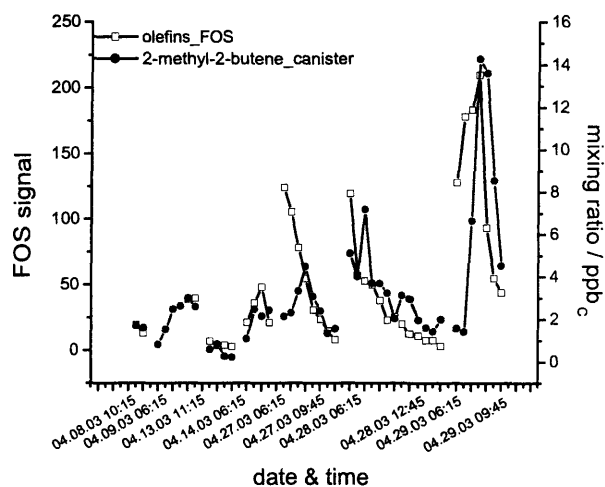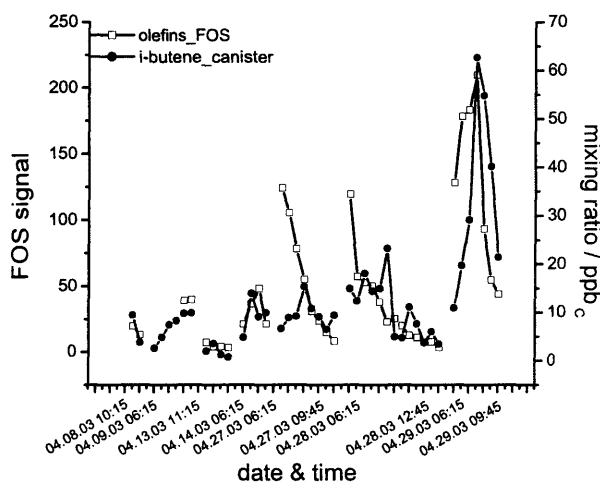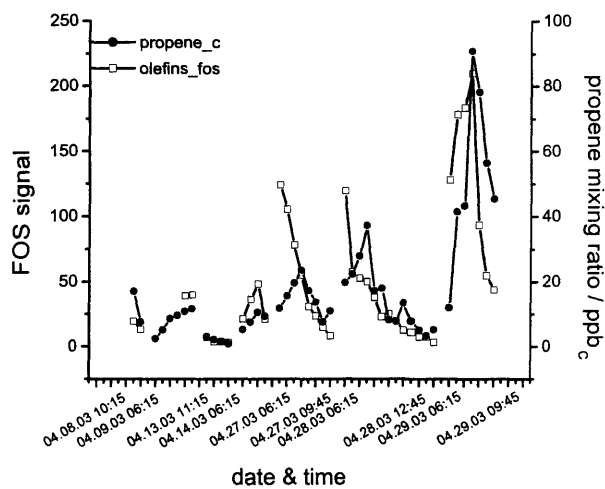
Figure 5-7: Alkene mixing ratios, as determined by analysis of air canister sampling, are plotted against the signal from a real-time continuous Fast Olefin Sensor (FOS) instrument during 7 days of overlapping measurements. Both sets of data were provided by the research group at WSU. The closed circles represent data from the canister sampling: a) isoprene; b) 2-methyl-2-butene; c) i-butene; d) propene.

The average diurnal profile for the FOS signal (Figure 5-8) was used in conjunction with the scaling factors listed in Table 5.3 to constrain the code used for the box model.
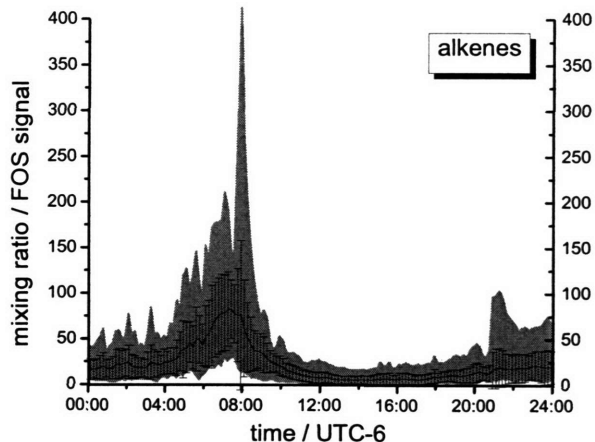
Figure 5-8: The averaged diurnal profile for the FOS signal used to determine the concentrations of alkene species used in the box model. Data for the FOS signal are provided by the research group at WSU.

Aromatics

MCMv3.1 includes the degradation kinetics and reaction dynamics for 18 aromatic hydrocarbons. The model presented here has been constrained for 16 of the 18 aromatic hydrocarbon species[4]. Of these 16 species, 14 of them are constrained based on WSU canister data and DOAS measurements. The other two aromatic hydrocarbons were scaled based on emissions data.

The DOAS instruments [115, 116] provided direct real-time continuous measurements of benzene, toluene, m-xylene, p-xylene, styrene, benzaldehyde, and mono-substituted benzenes (see Figures 5-9 and 5-10.). Data from the WSU canisters are used to determine appropriate scaling factors for a number of other aromatic hydrocarbons. The scaling is determined by the mixing ratios in ppb of carbon, ppb_C, of

---

[4]The two aromatic species that were not constrained are 3,5-dimethyl ethyl benzene and 3,5-diethyl toluene.

each aromatic as a percentage of the total mixing ratio of all measured aromatic hydrocarbons (Figure 5-11). The scaling factors are listed in Table 5.4. Each compound not directly measured (other than the mono-substituted benzenes discussed below) via DOAS is scaled based on the total mixing ratio in ppb of carbon, determined by the real-time continuous measurement of toluene. Because the toluene measurement is used as a reference for calculating the total mixing ratio of aromatic hydrocarbons in ppb of carbon, it is inherently assumed that the species not directly measured have a similar diurnal profile as toluene.

Selected data from the DOAS instrument were plotted against data obtained by the air canister sampling to demonstrate the utility of scaling the aromatic hydrocarbons by ppb of carbon as a means to constrain the code (Figure 5-12). The observable profiles between the two measurements are consistent, and scaling as a percentage of ppb of carbon captures the relative profile of each species.

It is assumed that ethyl benzene, n-propyl benzene, and i-propyl benzene combined represent 100% of mono-substituted benzene species measured by the DOAS instrument. The scaling factors for these species presented in Table 5.4 represent the average percentage (by %ppb$_C$) of each species relative to the sum of these species mixing ratios. The scaling factor for i-propyl benzene (cumene) was determined using emissions data from the EPA inventory database [117]. To determine the appropriate scaling factor for i-propyl benzene, the ratio of i-propyl benzene emissions to ethyl benzene emissions from urban monitors was averaged over the entire set of available data for the United States in 2004. The data were selected based on the reported location of the detector.

The scaling factor for 1,2,3-trimethyl benzene was determined based on emissions data from Harley et al.[113]. These data assume the primary source of 1,2,3-trimethylbenzene is exhaust from gasoline-powered light-duty vehicles without catalytic converters. It is assumed that the diurnal profile of 1,2,3-trimethyl benzene is similar to that of toluene.
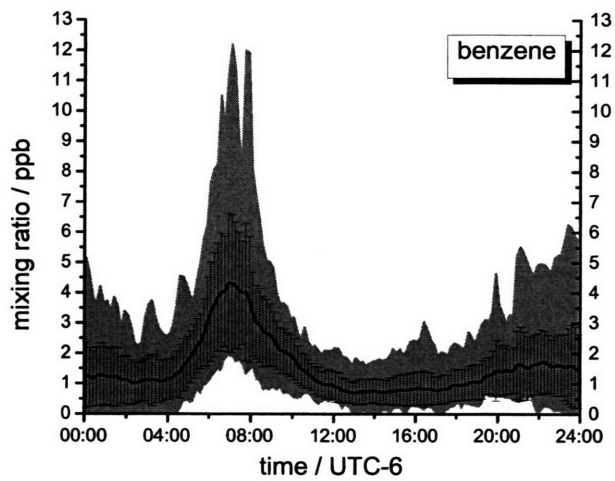
(a)
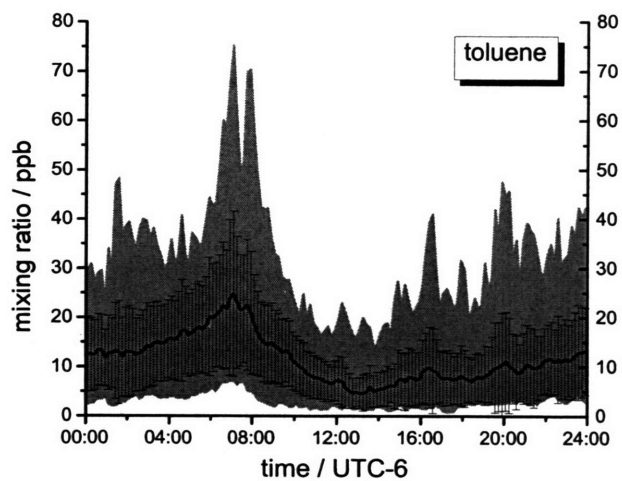
(b)
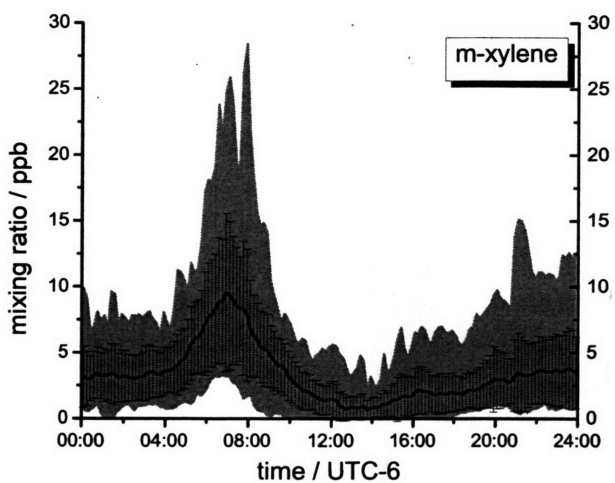
(c)
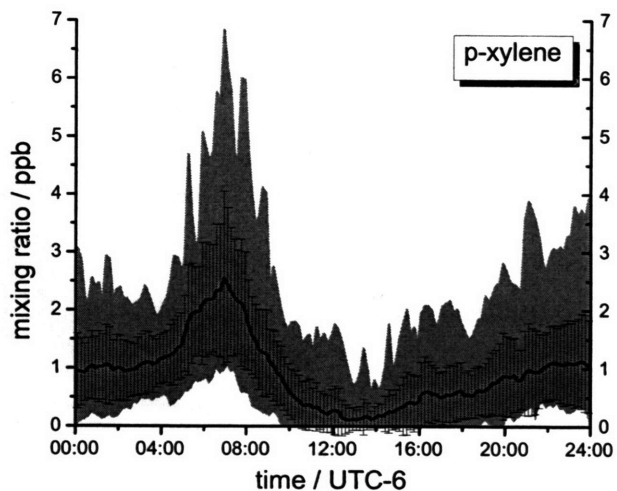
(d)

Figure 5-9: Diurnal profiles for aromatic hydrocarbons that were directly measured via DOAS by Rainer Volkamer at MIT.
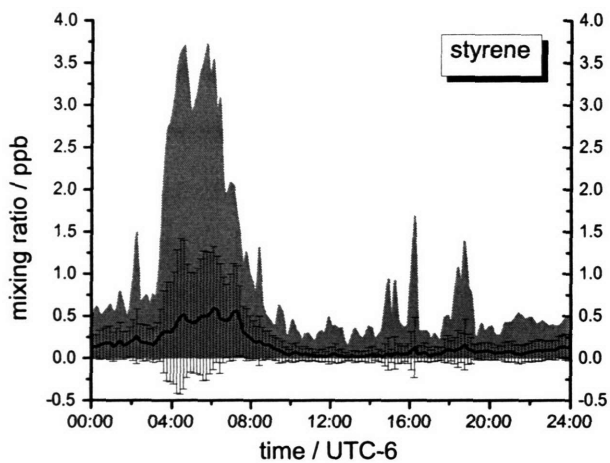
(a)
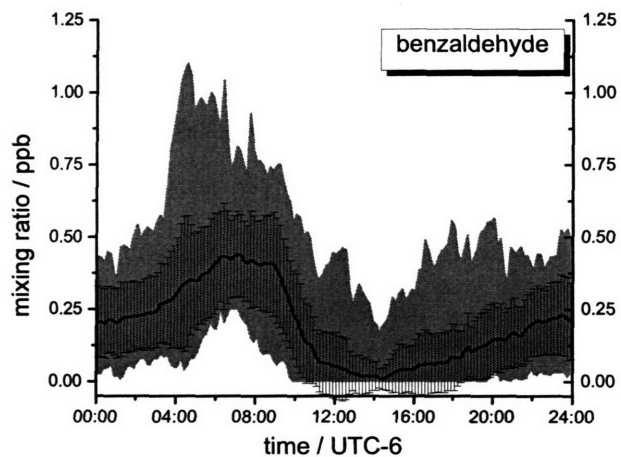
(b)
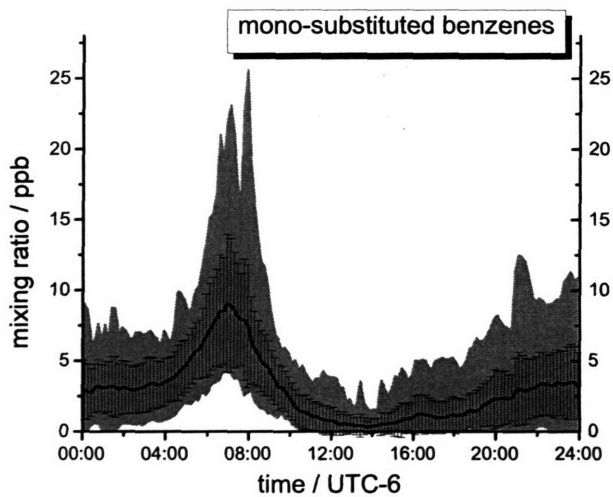
(c)

Figure 5-10: Diurnal profiles for aromatic hydrocarbons that were directly measured via DOAS by Rainer Volkamer at MIT.
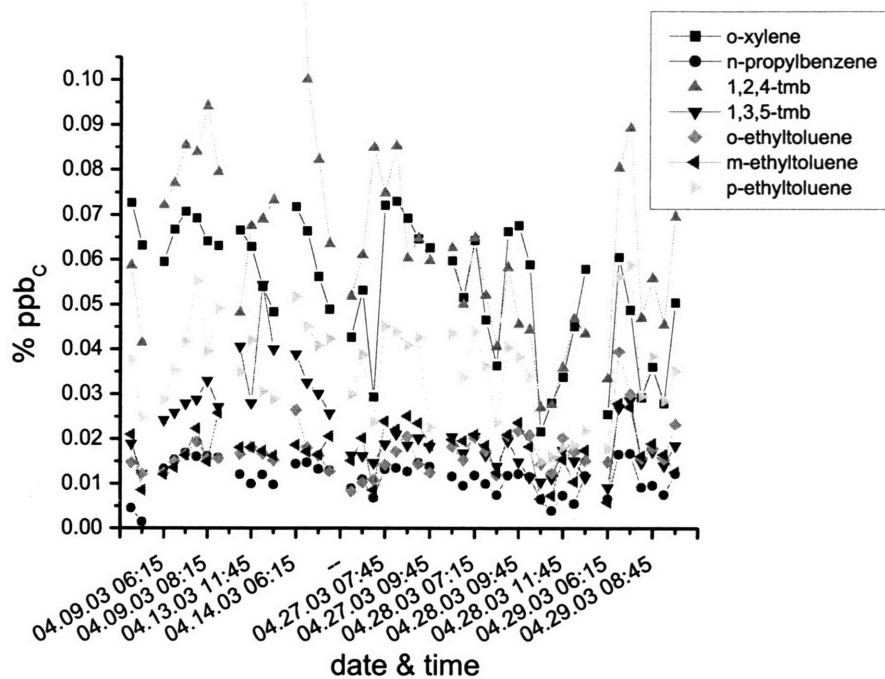
Figure 5-11: Ratio of select aromatic hydrocarbons to total aromatic hydrocarbons as percentage of mixing ratio in ppb of carbon.

Table 5.4: Scaling factors for aromatic hydrocarbons, as calculated from the percentage of each species relative to the total ppb of carbon for aromatic hydrocarbons from air canister sampling data. The data were provided by the research group from WSU. The scaling factors in the second 'box' are the percentages that each species represents for measured mono-substituted benzenes. The third 'box' has a scaling factor that was estimated based on available emissions data from the EPA inventory [117].

aromatic hydrocarbon	scaling factor $(\pm\sigma)$ x 10^{-2}
o-xylene	5.4 (1.5)
1,2,4-trimethylbenzene	6.4 (2.4)
1,3,5-trimethylbenzene	2.2 (0.9)
o-ethyltoluene	1.7 (0.5)
m-ethyltoluene	1.8 (0.5)
p-ethyltoluene	3.6 (0.1)
ethyl benzene	62 (10)
n-propyl benzene	16 (3)
i-propyl benzene	22 (4)
1,2,3-trimethylbenzene	1.6

85
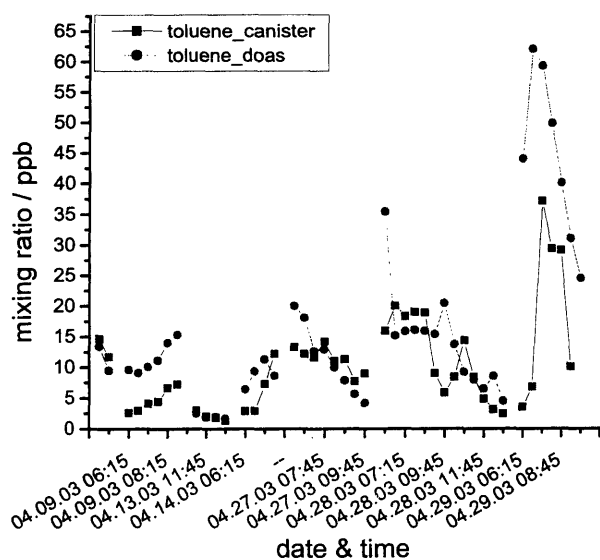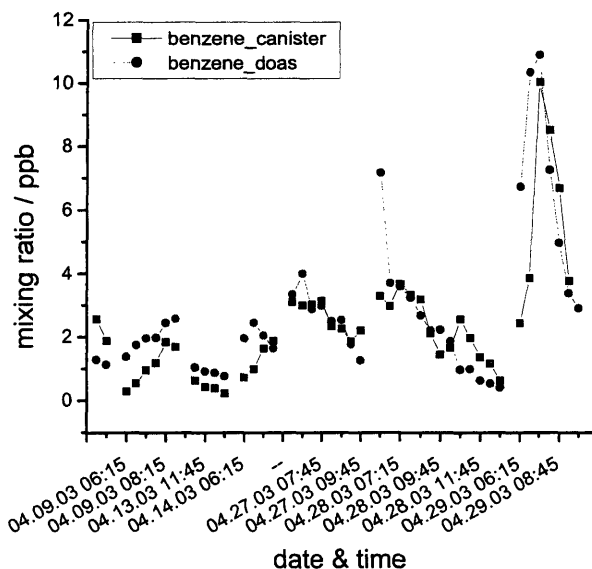
(a)   (b)

Figure 5-12: Aromatic hydrocarbon mixing ratios in ppb of carbon from two types of measurements made during the field campaign: DOAS and air canister sampling. The DOAS data were provided by Rainer Volkamer at MIT and the air canister data were provided by the research group at WSU. The circles represent the DOAS data. a) toluene and b) benzene.

Alcohols and Glycols

MCMv3.1 includes the degradation kinetics and reaction dynamics for 18 alcohol and glycol species. The model presented here has been constrained for 10 of these species: 8 alcohols and 2 glycols. Of these species, only methanol was directly measured during the 2003 MCMA field campaign. The remaining species were scaled using available emissions data.

Real-time, continuous measurements of methanol were made during the field campaign by researchers at Pacific Northwest National Laboratory (PNNL) using a Proton Transfer Reaction Mass Spectrometer (PTR-MS) instrument [118]. The averaged diurnal profile for methanol, as determined from the data provided by PNNL, is shown in Figure 5-13.
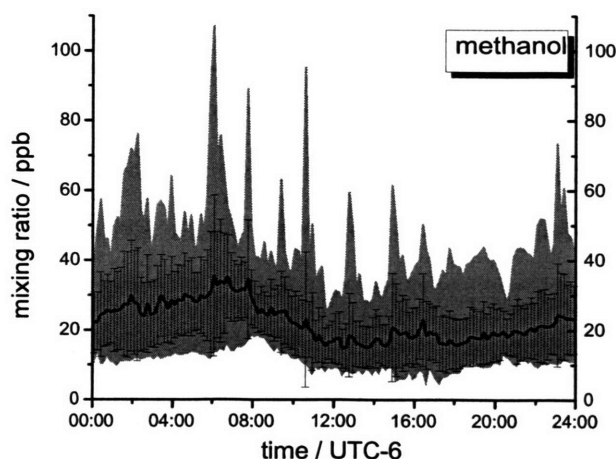
Figure 5-13: Diurnal profile of methanol as measured during the 2003 MCMA field campaign. Data were provided by research group at PNNL. The data here were used to scale the ambient concentrations used in the model for the species in Table 5.5.

The remaining species (Table 5.5) were scaled relative to methanol using estimations based on available emissions data from Harley *et al*[113]. These species were scaled based on speciation profiles of surface coatings and adhesives with consideration given to available information regarding source contributions to non-methane organic gas concentrations measured at various monitoring sites. Harley *et al.* have shown that the *relative* abundance of select organic compounds in a respeciated gas

inventory generally agrees with ambient data. The two main assumptions made are: a) the constrained alcohol and glycol species have similar ambient profiles to methanol and b) the primary source of emissions for these species are from the use of surface coatings and adhesives.

Table 5.5: Scaling factors for select alcohols and glycols. Factors are estimated based on emissions data from Harley et al.[113]. The scaling factors are reported as a percentage of the mixing ratio of methanol in ppb of carbon.

alcohol/glycol species	scaling factor
ethanol	15
1-propanol	5
2-propanol	5
1-butanol	2
2-butanol	2
2-methyl-1-propanol	2
2-methyl-2-propanol	2
ethylene glycol	25
propylene glycol	10

Aldehydes

MCMv3.1 includes the degradation kinetics for 6 aldehyde species. The box model presented here has been constrained for 3 of these. Both formaldehyde and acetaldehyde were directly measured by DOAS and PTR-MS, respectively. The observed values for formaldehyde were scaled because of a recent update of the absorption cross-section of HCHO [119]. The diurnal profiles for both of these species are presented in Figure 5-14. The third aldehyde species, propanal, was scaled to formaldehyde based on available emissions data [113, 117]. Propanal was estimated as 4.5% of formaldehyde emissions based on speciation data from gasoline engine exhaust from light-duty vehicles without catalytic converters.

Ketones

MCMv3.1 includes the degradation kinetics and reaction dynamics for 10 ketones. The box model presented here has been constrained for 3 of these species. Both
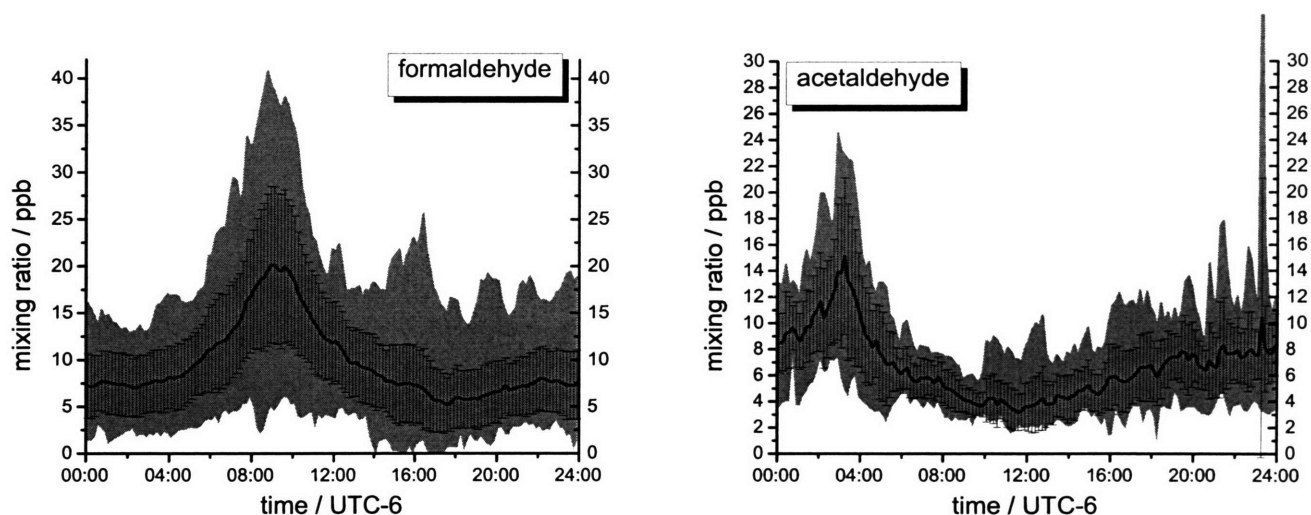
(a)   (b)

Figure 5-14: Diurnal profiles for formaldehyde (HCHO) by DOAS and for acetaldehyde species measured during the 2003 MCMA field campaign by PTR-MS. Data for formaldehyde and acetaldehyde were provided by Rainer Volkamer at MIT and from the research group at PNNL, respectively.

acetone and methyl ethyl ketone (MEK) were directly measured using PTR-MS by the research group at PNNL. The averaged diurnal profiles for both acetone and MEK are presented in Figure 5-15. The third ketone species, methyl i-butyl ketone (MIBK) was scaled to MEK based on emissions data obtained from the US EPA online database. All data collected for MEK and MIBK in 2004 for urban and rural monitors were compared and averaged to produce a ratio of MIBK to MEK. This ratio was used as a scaling factor for input into the box model. Based on data from the EPA online inventory, MIBK is estimated to be 13% of the MEK mixing ratio in ppb of carbon.

Esters

MCMv3.1 includes the degradation kinetics and reaction dynamics for 8 organic esters. The box model presented here has been constrained for 4 of these. Ethyl acetate mixing ratios were determined by GC/FID analysis of the air canister sampling done by the research group at WSU (described previously). The average value for ethyl

(a)   (b)
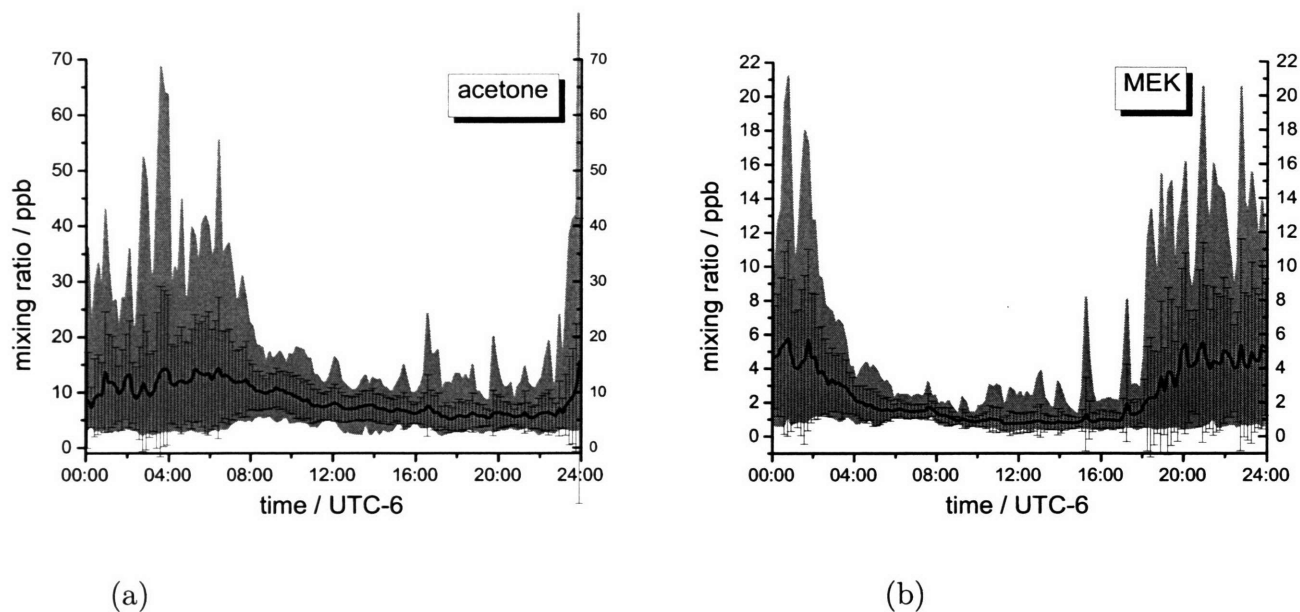
Figure 5-15: Diurnal profiles for ketone species measured during the 2003 MCMA field campaign by PTR-MS. Data were provided by the research group from PNNL.

acetate as a percentage of total mixing ratio in ppb of carbon was used to determine the concentrations used in the box model and is presented in Table 5.6. Concentrations for n-propyl, i-propyl and n-butyl acetate were estimated based on their percent compositions relative to that of ethyl acetate in the speciation profiles for surface coatings and adhesives, taken from Harley *et al.*[113]. The scaling factors in Table 5.6 for these compounds represent the percentage of these species relative to ethyl acetate.

Table 5.6: Scaling factors for organic esters used as input parameters. The value for ethyl acetate is a % ppb of total carbon, while the values for the remaining species represent the percentage of these compounds mixing ratios in ppb of carbon relative to ethyl acetate.

organic esters	scaling factor
ethyl acetate	0.6
n-propyl acetate	25
i-propyl acetate	25
n-butyl acetate	35

Ethers and Glycol Ethers

MCMv3.1 includes the degradation kinetics and reaction dynamics of 10 ethers and glycol ethers. The box model presented here has been constrained for 6 of these species. Methyl t-butyl ether (MTBE) was measured in the GC/FID analysis of air canister sampling done by the research group at WSU. The average percent mixing ratio of MTBE relative to total ppb of carbon detected using the canisters samples was calculated and used as an input scaling factor for the box model.

The remaining species were all glycol ethers (Table 5.7) and were scaled based on emissions data from Harley et al.[113] and the EPA online emissions inventory[117]. The scaling factors for each of these species are all reported as average percentages of the methanol mixing ratio (in ppb of carbon). The glycol ethers are scaled relative to methanol based on the speciation profiles for surface coatings and adhesives from Harley et al. and the 24-hr average concentrations reported by the EPA relative to the reported concentrations of methanol.

Table 5.7: Scaling factors for MTBE and select glycol ethers used as input parameters. The value for MTBE is a % ppb of total carbon, while the values for the remaining species represent the percentage of these compounds mixing ratios in ppb of carbon relative to methanol.

ethers and glycol ethers	scaling factor
MTBE	1.1
2-methoxy ethanol	2
2-ethoxy ethanol	2
1-methoxy 2-propanol	2
2-butoxy ethanol	2
1-butoxy 2-propanol	2

Halohydrocarbons

MCMv3.1 includes the degradation kinetics and reaction dynamics of 17 halohydrocarbon species. The box model presented here has been constrained for all of these species. There are 15 chlorohydrocarbon and 2 bromohydrocarbon species. Monitoring data on all of these species are available from the EPA's online database. The

entire set of data available for the United States from the year 2004 for these species was used to determine the appropriate scaling factors for these species. The data provided through the EPA is limited to 6-hr and 24-hr averages. In an effort to avoid over-estimating the contribution of these species to general chemical reactivity in the box model, the median values from all the data from the EPA's 24-hr averages were used. After determining an appropriate 24-hr average value, the assumption was made that these halohydrocarbon species would have a similar profile to the alkanes measured by the FTIR instrument (discussed previously). The diurnal profile for the alkane species was normalized and then scaled appropriately to be consistent with the 24-hr averages of the relative halohydrocarbons (Table 5.8).

Table 5.8: 24-hr averages for halohydrocarbons as determined by the median of available EPA monitoring data for the year 2004.

halohydrocarbons	24-hr avg (ppb_C)
methyl chloride	0.55
methylene chloride	0.10
chloroform	0.05
per-chloroethylene	0.05
tri-chloroethene	0.066
c-1,2-dichloroethene	0.025
t-1,2-dichloroethene	0.05
1,2-dichloroethane	0.05
1,1-dichloroethene	0.05
1,2-dichloropropane	0.05
1,1-dichloroethane	0.05
chloroethane	0.05
1,1,2,2-tetrachloroethane	0.05
1,1,2-trichloroethane	0.05
bromomethane	0.05
1,2-dibromoethane	0.05

Everything Else

Acetylene, the only alkyne species in MCMv3.1, was measured by GC/FID as part of the analysis of the air canister sampling by the group at WSU. An average percentage of its mixing ratio in ppb of carbon compared to that of total mixing ratio of carbons

was determined and used to scale the compound appropriately. Acetylene was scaled as 1.9 % of the total mixing ratio of carbon.

Acetic acid was measured directly and continuously using PTR-MS by the group at PNNL. The averaged diurnal profile for this compound is presented in Figure 5-16.

Temperature and pressure were also measured throughout the entire campaign, and are necessary to calculate accurate mixing ratios for the species in the box model. The average diurnal profiles of temperature and pressure are also shown in Figure 5-16.

Using traffic counts and measured concentrations of CO, we have the means to effectively dilute compounds in the mechanism where measurements are not available. The data for mixing heights were provided in height increments, an arbitrary measure, and were converted to a rate parameter by treating it as a first-order decay process. Using the data provided, the rate constant to dilute the compounds was calculated as

$$k_{dilution} = \ln \frac{D_{n+1}}{D_n} * (1/\Delta t), \tag{5.1}$$

where D_n is the measure of the height increment and Δt is the time between measurements, or 600 seconds. Based on available data (Figure 5-17), select parameters are diluted from 08:00-16:00. This method was validated by testing against benzene. Benzene is relatively unreactive during the time period between 08:00 - 16:00. The measured concentration of benzene during this time period can be estimated as follows:

$$[B] = [B]_0 + [B]_{emissions} - [B]_{diluted} \tag{5.2}$$

where $[B]_0$ is the concentration of benzene at 08:00, $[B]_{emissions}$ is the source term from emissions (primarily from traffic) and $[B]_{diluted}$ is the loss term from dilution. Benzene is directly measured during the campaign, and as such, we can assume that all of these factors are captured. If the measured concentration of benzene at 08:00 is used with the rate of dilution that is calculated from Equation 5.1, then it is expected that the calculated decay of benzene would be slightly lower than the observed concentrations, because the $[B]_{emissions}$ factor is not included. This calculation is shown in Figure 5-17-
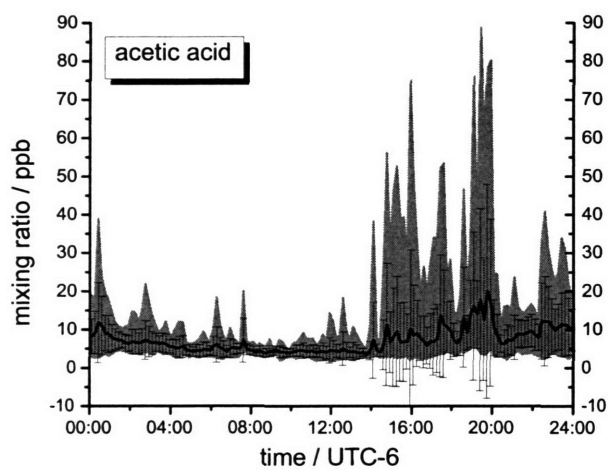
(a)
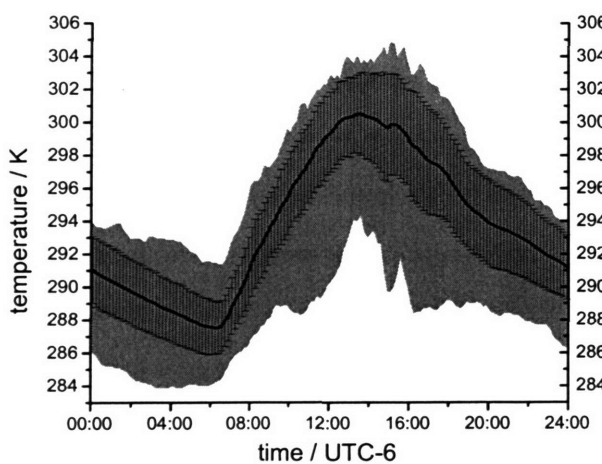
(b)
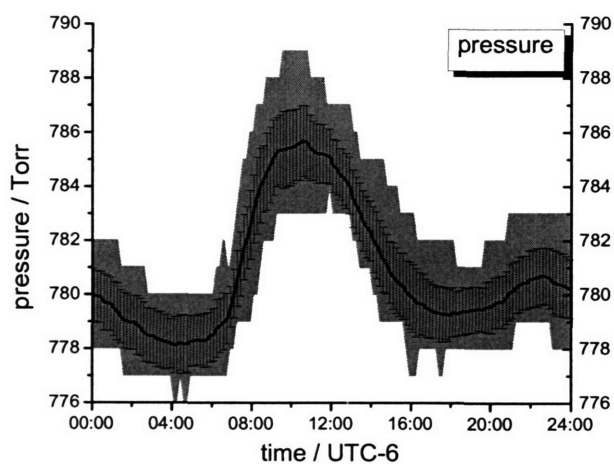
(c)

Figure 5-16: Diurnal profiles for (a) acetic acid, measured by PTR-MS; (b) temperature; and (c) pressure, both measured at the CENICA site.

b. As expected, this calculation slightly underestimates the concentration of benzene without the additive factor of fresh emissions. Even so, in the model, it is only necessary that oxidized products, which do not have the emissions term like benzene, are diluted. The agreement between the calculated and the observed concentrations of benzene from 08:00-16:00 confirms the efficacy of diluting select compounds in the MCM to avoid unrepresentative chemical accumulation.

(a)   (b)
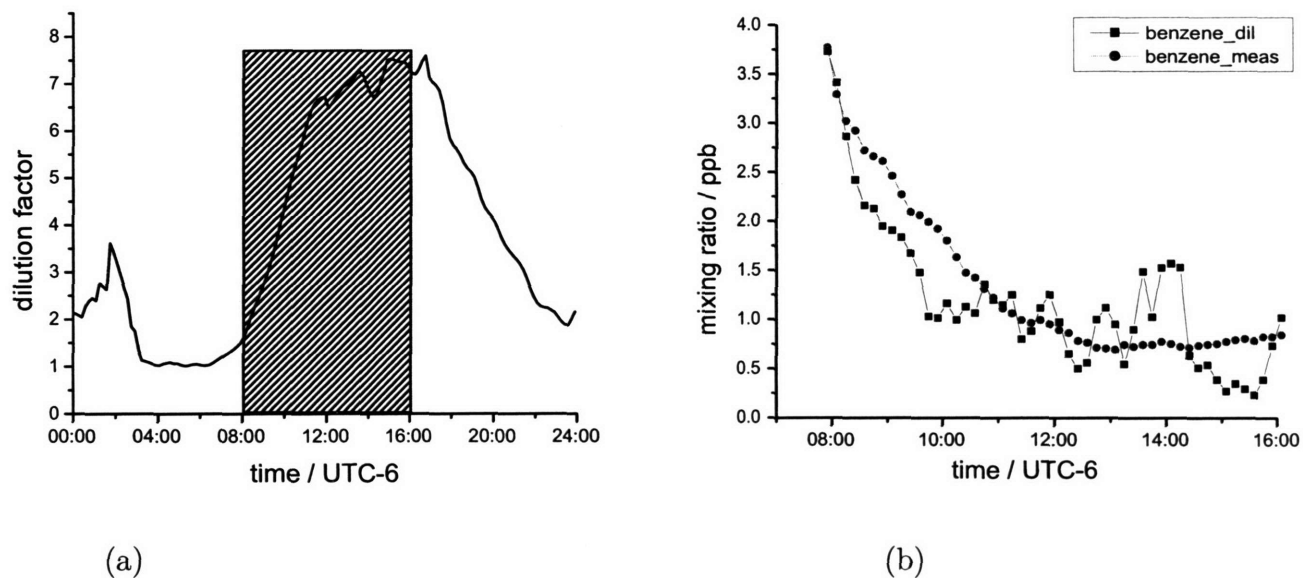
Figure 5-17: a) A representative average of the increase in the atmospheric mixing layer during the day as measured during the 2003 MCMA field campaign, as a measure of height increment. Data are only diluted and not 'concentrated', so only the data between 08:00 and 16:00 (shaded) are considered. b) Calculated 'dilution' of benzene as a first-order decay process using Equation 5.1, compared to observed concentration of benzene, which includes both dilution and fresh emissions.

Photolysis Rates of Reactions

Photolysis rates in the mechanism are calculated based on the assignment of photolysis parameters to a limited number of representative photolysis reactions with existing data for absorption cross sections and quantum yield [120] (Table 5.9). Calculated photolysis rates as a function of solar zenith angle (SZA) used here have been determined previously using a two stream isotropic scattering model. Calculations were initially performed using clear sky conditions at a latitude of 19°21'32" N and

a longitude of 99°4'25" W. The solar zenith angle is calculated as a function of the solar declination angle, δ_s and the local elevation angle, Ψ. The following equation and definitions are taken from *Meteorology for Scientists and Engineers* by Roland B. Stull [121]. The solar declination angle is defined as the angle between the ecliptic and the plane of the earth's equator. It is calculated as:

$$\delta_s = \phi_r \cos\left[2\pi \frac{(d - d_r)}{d_y}\right] \tag{5.3}$$

where ϕ_r is the tilt of the earths axis relative to the ecliptic, and is equal to 0.409 radians, d is the Julian Day (e.g. April 15, d=104 days), d_r corresponds to the Julian day of the summer solstice in a non-leap year (June 22, $d_r = 173$ days), and d_y is the total number of days per year, $d_y = 365$ days. Note that this equation is an approximation, as it assumes that the earths orbit is circular not elliptical.

Table 5.9: Selected photolysis reactions and parameters assigned as a function of solar zenith angle, χ (Table from Saunders *et al.*[97])

reaction		$J = l(cos\chi)^m exp(-nsec\chi)$		
		l	m	n
O_3	$\rightarrow O(^1D) + O_2$	6.073E-5	1.743	0.474
	$\rightarrow O(^3P) + O_2$	4.775E-4	0.298	0.080
NO_2	$\rightarrow NO + O(^3P)$	1.165E-2	0.244	0.267
HONO	$\rightarrow OH + NO$	2.644E-3	0.261	0.288
HNO_3	$\rightarrow OH + NO_2$	9.312E-7	1.230	0.307
HCHO	$\rightarrow HCO + H$	4.642E-5	0.762	0.353
HCHO	$\rightarrow CO + H_2$	6.853E-5	.0477	0.323
CH_3CHO	$\rightarrow HCO + CH_3$	7.344E-6	1.202	0.417

The calculation of photolysis rates solely as a function of solar zenith angle does not account for cloud coverage, scattering in the atmosphere, and the albedo of the earth's surface. The photolysis rates in the code are corrected using a factor that is based on the average deviation from the measured rates of photolysis of O_3, NO_2, and HCHO (see Figure 5-18). Photolysis rates were calculated based on data collected using spectroradiometry and available molecular photochemical data (i.e. UV absorption cross section and quantum yields). Spectroradiometry is a technique which

96

measures the actinic photon fluxes in a centrally resolved manner. A special $J(NO_2)$ filterradiometer was also employed, which is uniquely sensitive to the actinic UV-radiation that specifically photolyzes NO_2 in the atmosphere.
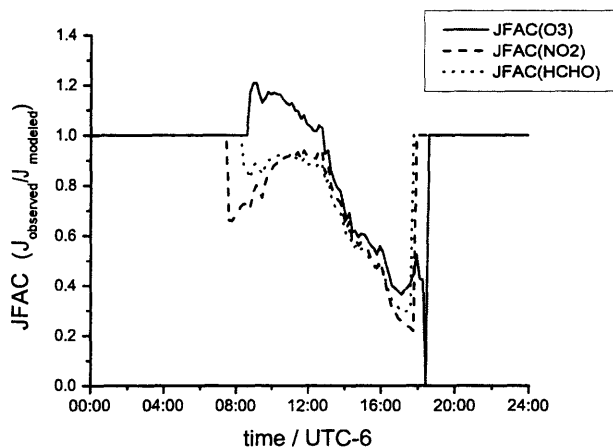
Figure 5-18: Calculated values for photolysis rate parameters do not include back scattering, cloud cover, or the earth's surface albedo. Scaling the calculated rate parameters with observations provide a factor to adjust photolsyis parameters in the box model. The J(factor) for $J(NO_2)$ (dashed line) is used to scale the photolysis rates other than $J(O_3)$ (solid line) and $J(HCHO)$ (dotted line).

5.2.4 HO$_X$ Parameters

A research group at Pennsylvania University (PSU) participating in the 2003 MCMA field campaign measured both OH and HO_2 from the CENICA site. Both species were measured by a Ground-based Tropospheric Hydrogen Oxides Sensor (GTHOS). The technique employs a Fluorescence Assay by Gas Expansion (FAGE) [122]. The instrument has a low detection limit of 0.01 ppt$_V$ for both OH and HO_2, with data averaged over every 1-min time interval. The diurnal profiles of data for OH and HO_2 from GTHOS are presented in Figure 5-19. The data was provided in 1-min time intervals and was averaged over 10-min time intervals to maintain a consistent input format for the model.
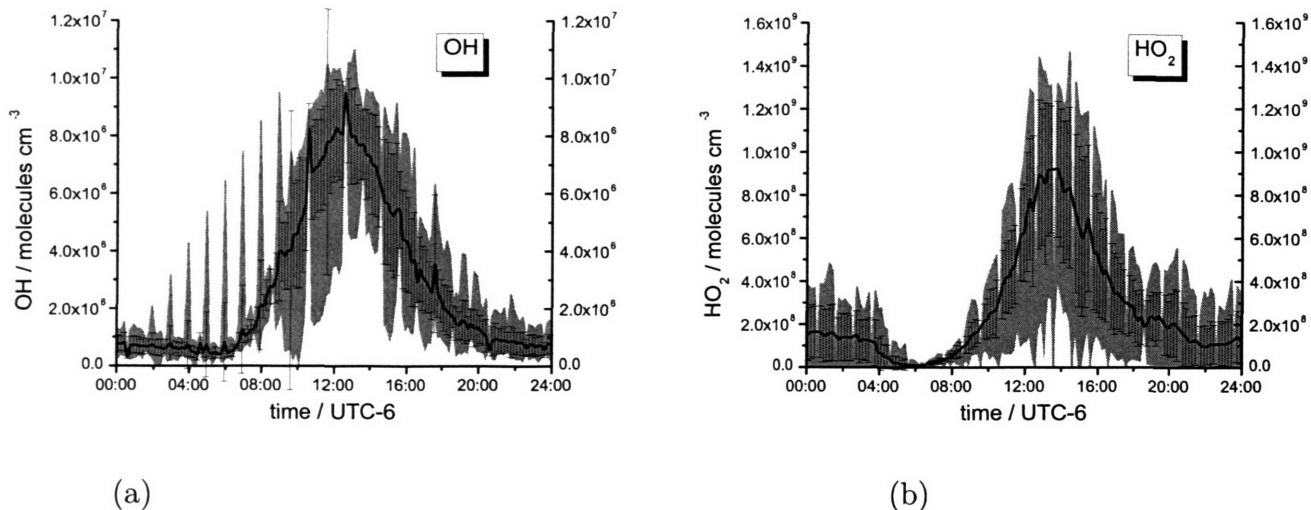
Figure 5-19: Diurnal profiles of OH (a) and HO_2 (b) during the 2003 MCMA field campaign. Measurements were made by GTHOS and data were provided by T. Shirley at PSU.

5.2.5 Defining parameters

Carefully defined output parameters allow the user to explore the sources, recycling and sinks of OH and HO_2, as calculated by the box model. For clarity and consistency, the following terms will be defined here: new radical production, radical recycling, and sink. The term new radical production refers to the formation of a OH or HO_2 molecule (generally, by photolysis) from a closed-shell species. For instance, the photolysis of HONO is considered a reaction generating new OH:

$$HONO + h\nu \rightarrow OH + NO \tag{5.4}$$

The term radical recycling refers to any reaction that converts a OH molecule to a HO_2 molecule, or vice versa. For instance, the reaction between HO_2 and NO that generates OH is considered OH recycling ($HO_2 \rightarrow OH$):

$$HO_2 + NO \rightarrow OH + NO_2 \tag{5.5}$$

The sink term refers to any reaction between a OH or HO_2 molecule that results in the formation of a stable, closed-shell species. For instance, the following reaction between OH and NO_2 is considered a sink:

$$OH + NO_2 \rightarrow HNO_3 \qquad (5.6)$$

5.2.6 Constrained vs. Unconstrained Parameters

As mentioned above, the model has been constrained for over 100 parameters (primarily VOC species); however, the MCMv3.1 contains some 4500 species and 13500 reactions. The extensive set of data from the 2003 MCMA field campaign provides a unique opportunity to construct a box model with constraints on most of the major contributors to the oxidation capacity of the troposphere. These constraints enable the investigation of primary and secondary pathways that contribute to the oxidation capacity of the troposphere. Therefore, it is worthwhile to ensure that the box model is in fact effectively constrained. This diagnostic is performed by summing all radical fluxes for reactions with OH as a product and as a reactant, which will be collectively referred to as OH production and OH loss [5]. The constrained species for OH loss are further divided by species that were directly measured or scaled verses those that were estimated.

OH production is dominated by the recycling of a HO_2 molecules into OH by reaction with ozone, NO and NO_3. As you can see in Figure 5-20, the box model predicts that both ozone and NO play a much more significant role in OH formation from recycling than for NO_3, an unconstrained parameter. Although the new production of OH radicals from photolysis is not as significant a source, it is also well constrained, as seen in Figure 5-21. Based on these figures, it is estimated that over 95 % of OH production is constrained.

There are hundreds of OH loss channels in MCMv3.1. OH loss is not as well constrained as OH production, particularly in the hours after sunrise. The overwhelming

---

[5]OH loss should not be confused with OH sinks, which are actually termination steps for radical propagation.
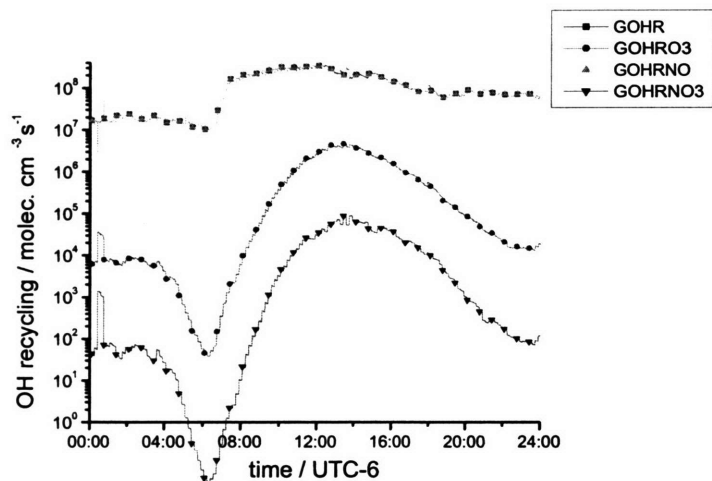
Figure 5-20: Comparison of three pathways for formation of OH radical from the reaction of NO, ozone, and nitrate radical with HO_2 (note logarithmic scale). The reaction with NO is clearly the dominant channel, as it varies from 2-7 orders of magnitude greater than the other channels.
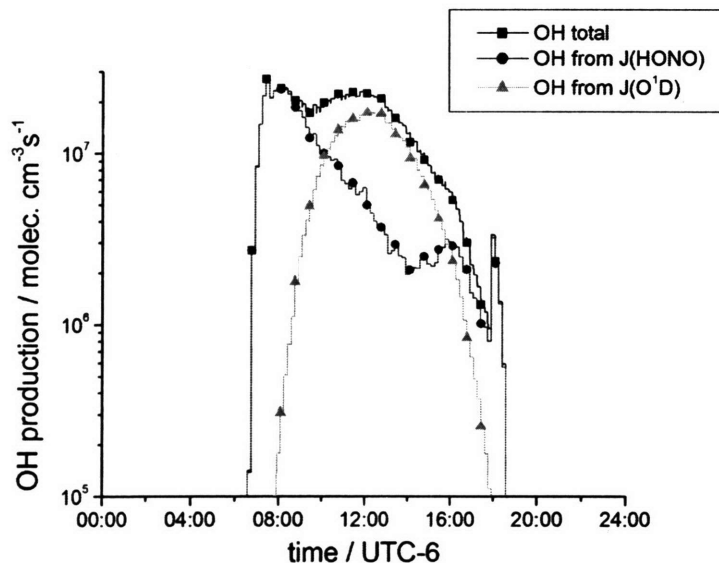
Figure 5-21: The box model predicts that the photolysis of HONO and the reaction between $O(^1D)$ and water, after the photolysis of ozone, are the primary contributors to the new production of OH in the troposphere. HONO makes a significant contribution to the production of OH at sunrise; however, as the day progresses, the reaction becomes less important. The re-formation of HONO from OH and NO in the atmosphere is also fast, and further suppresses the contribution of HONO photolysis to new OH production beyond the hour or two following sunrise.

100

number of intermediates that are often reactive with OH; as such, the percentage of OH loss that is constrained changes throughout the day. Total OH loss, OH loss from constrained parameters that were directly measured, OH loss from parameters that were estimated based on emissions inventories, and OH loss from unconstrained parameters as a function of time of day are plotted in Figure 5-22-a. In Figure 5-22-b the percentage of constrained and unconstrained parameters throughout the day is plotted to demonstrate the decreasing effect of constraining the model shortly after sunrise due to increased formation of oxidative products.

(a)   (b)
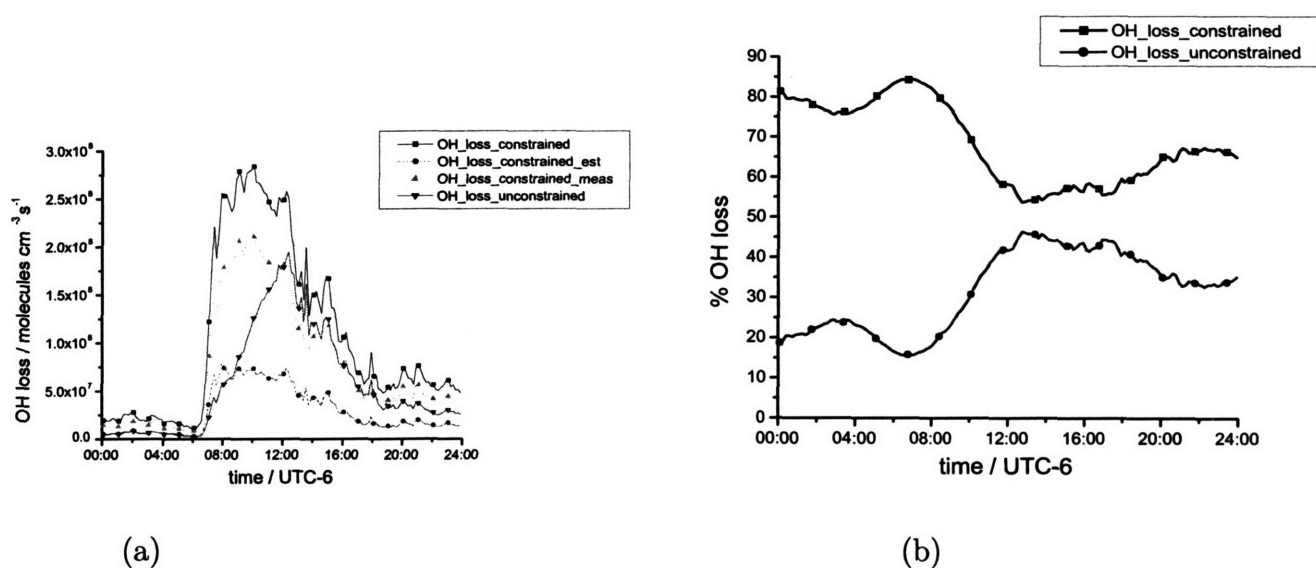
Figure 5-22: a) Constrained vs unconstrained parameters, and their contribution to the total radical flux of reaction with OH. b) Note the decreasing percentage of the constrained parameters as a function of OH loss in the early morning hours after sunrise. The oxidative capacity of the MCMA urban troposphere is effectively constrained by an average of nearly 70 % during the day.

Steady State

To ensure that the code is properly emulating HO_x kinetics in the troposphere, one can run a simple, yet important diagnostic test. The lifetime of OH in the troposphere during the 2003 MCMA field campaign varied from 5 - 50 ms; a time scale much shorter than most other kinetic and dynamic processes in the troposphere. As such, OH should be observed in steady state: OH production, any reaction forming OH,

should equal OH loss, any reaction resulting in the recycling or 'sink'-ing of a OH molecule. All of the OH production and OH loss terms in the 13500+ reactions of the MCMv3.1 are summed and plotted against each other for the entire 24-hour run in Figure 5-23. The two curves are essentially indistinguishable, indicating that indeed OH is in a steady state for the duration of the run. Similar profiles are observed for each Case described below.
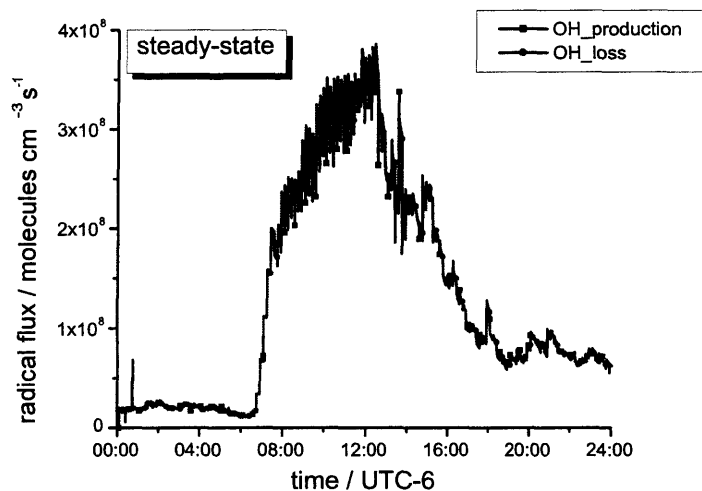
Figure 5-23: The lifetime of OH is short compared to the time scales of other tropospheric processes, and is in steady state in the troposphere. The box model accurately calculates OH in a steady state for the duration of each case presented here.

5.3 Results and Discussion

5.3.1 Case 1: no HO_X constraints

The observed and modeled concentrations for OH are presented in Figure 5-24-a. The model accurately predicts the diurnal profile and the concentration of modeled OH, and is in excellent agreement with observed concentrations. The observed-to-modeled ratios for OH are shown in Figure 5-25-a. With the exception of the very early morning hours (00:00 - 07:00), the measured-to-modeled ratios are well within the estimated uncertainty of the model and the measurements (discussed in more

102

detail below). The model slightly under predicts the concentration of OH during the morning rush hours between 08:00 and 10:00. For the hours of 11:00 until just before 20:00, the model and observed concentrations show no significant divergence. It appears that the modeled values may begin to increase with respect to the observed values after 20:00.

(a)   (b)
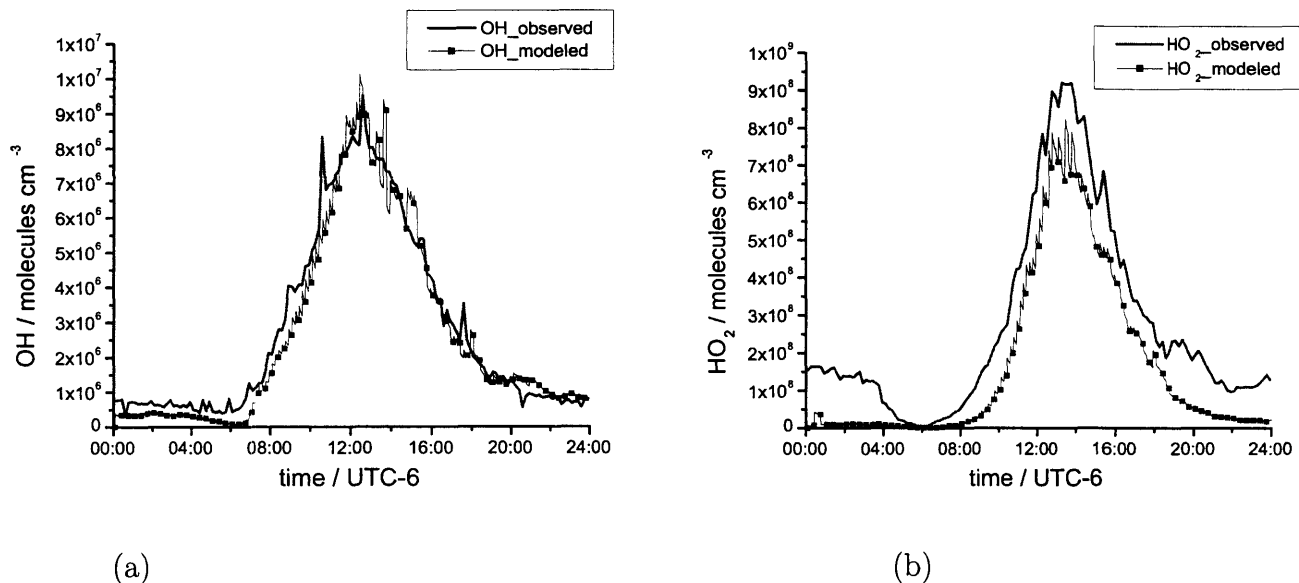
Figure 5-24: Comparison of observed OH (a) and HO_2 (b) data from the 2003 MCMA field campaign with box model calculations using the MCMv3.1.

The observed and modeled concentrations for HO_2 are presented in Figure 5-24-b. Although the model accurately predicts both the narrow HO_2 profile and the timing of the peak HO_2 concentration, the concentration is clearly underestimated for the entire day. The observed-to-modeled ratios for HO_2 are shown in Figure 5-25-b. The observed-to-modeled ratios for HO_2 fall within the estimated uncertainty of the model and measurements between 10:00 and 18:00; however, the very early morning hours indicate that the model is drastically under predicting the concentration of HO_2, with the measured values being as much as 23 times higher than those modeled. Although the ratios begin to improve just after sunrise (about 07:00), the observed-to-modeled ratios still range from 2-5 until 10:00. The model again begins to under predict the concentration of HO_2 starting just after 18:00, with what appears to be a steady increase in the observed-to-modeled ratio until the end of the day.
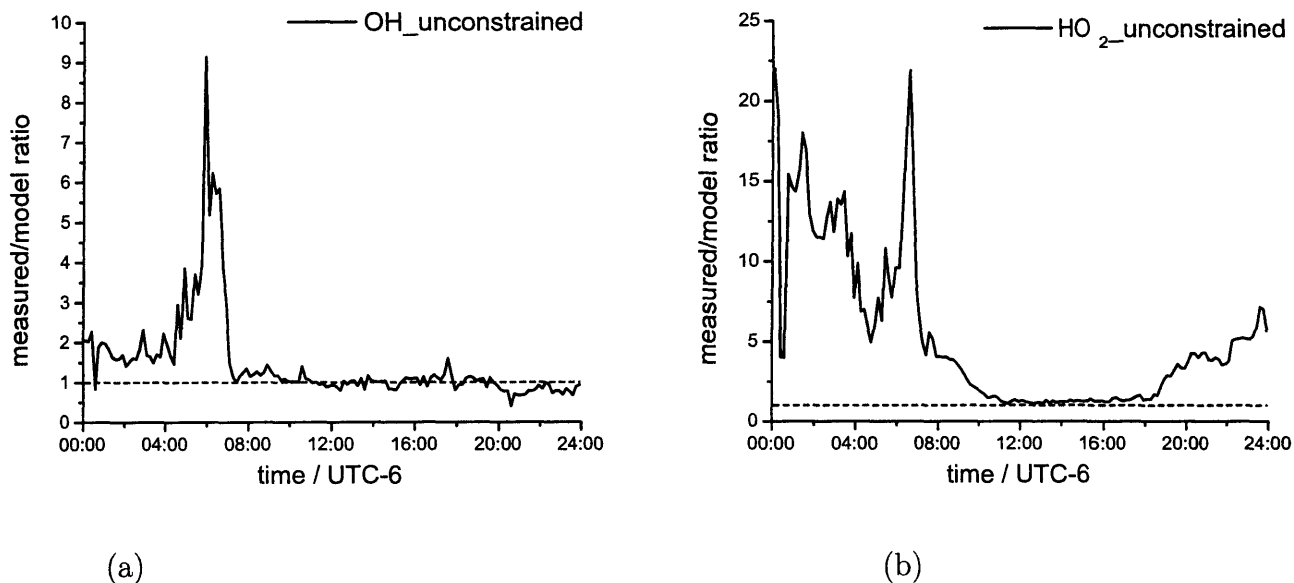
Figure 5-25: Observed to modeled ratios for OH (a) and HO_2 (b) concentrations. The dashed line represents a ratio of 1:1 for the observed to modeled concentrations.

Radical Budget

The HO_2 molecule accounts for a large fraction of the radical budget in the MCMA urban troposphere; however, only those molecules that are converted to OH contribute to the oxidation capacity of the troposphere. OH recycling, $HO_2 \rightarrow OH$, is then an important parameter. In the box model of the MCMA urban troposphere, there were three pathways for OH recycling: HO_2 reaction with NO, O_3, and HNO_3. Each species contribution to OH recycling as predicted by the box model are shown in Figure 5-20.

Just as accounting for the formation of OH from radical recycling of HO_2 is important as a means for quantifying the oxidative capacity of the troposphere, so too is the opposite process: $OH \rightarrow HO_2$. There are hundreds of channels in the box model that convert a OH molecule into HO_2 directly or indirectly. For instance, the reaction between OH and CO or HCHO directly forms HO_2. The oxidation of a VOC by reaction with OH forms RO_2, which in turn reacts with NO to form an alkoxy radical, RO. The alkoxy radical will react in the presence of oxygen to from HO_2. The contributions of these various processes to HO_2 recycling are shown in Figure

104

5-26 as a percentage of the radical flux during a 24-hour day.
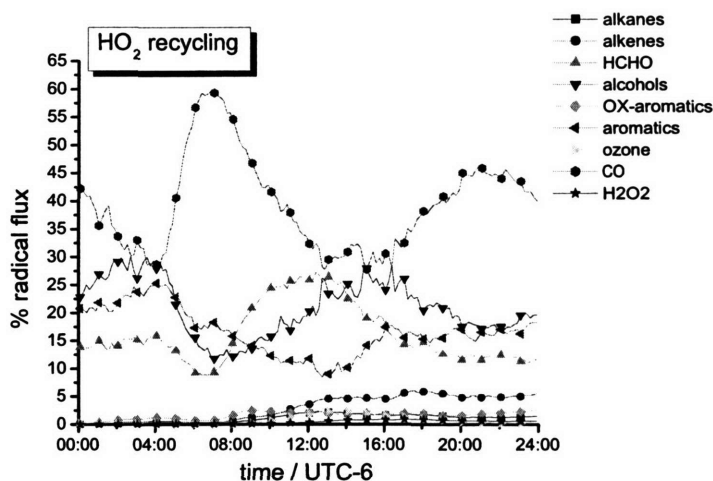
Figure 5-26: Comparison, as percentage contribution to the radical flux, of several HO_2 recycling channels. With the exception of the 'aromatics' and 'ox-aromatics' categories, the contributions from the groupings labeled as a VOC category (i.e. alcohols) are not from a reaction between OH and a primary VOC, but rather the reaction between OH and an oxidized species that is a product of a previous oxidation from that VOC category. The most dominant channels for HO_2 recycling are CO, HCHO, aromatics and oxidized alcohols.

5.3.2 Case 2: Constraining HO_2

The observed and modeled concentrations for OH, and the input values for HO_2 are presented in Figure 5-27. The modeled values generally agree with the observed OH profile from 06:00 to 18:00; however, during the early morning hours and the night time, the model over predicts the concentrations of OH by factors ranging from 2-5. The measured-to-modeled ratios for this case are presented in Fig 5-28. The model values are only within the estimated uncertainty of the box model for the aforementioned period, 06:00-18:00. Perhaps the most interesting feature is the persistent over prediction by the model of OH during the morning rush hour and just after sunrise (initiation of photolysis), from 07:00 - 10:00.
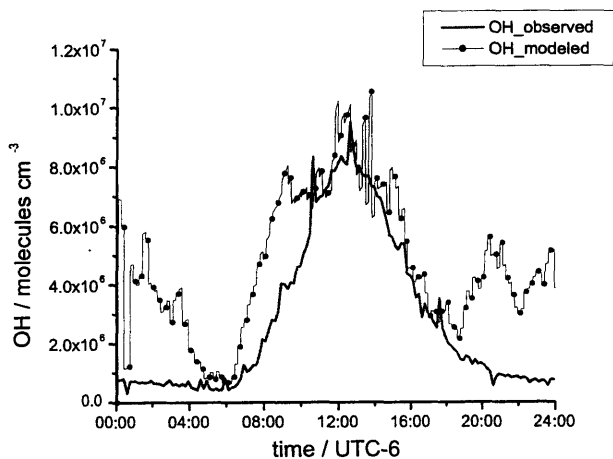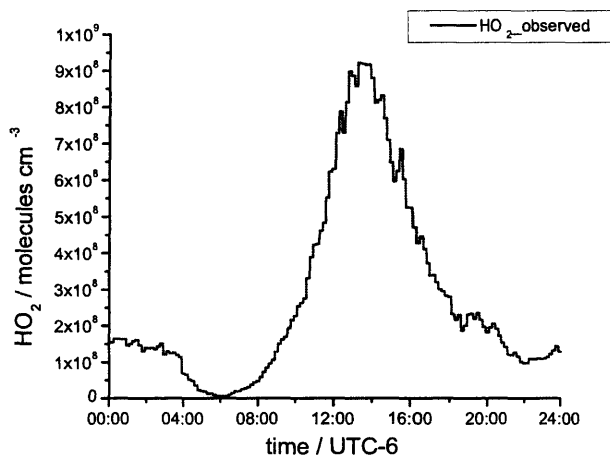
(a)   (b)

Figure 5-27: Comparison of observed OH data from the 2003 MCMA field campaign with a box model calculation performed with HO$_2$ constrained (b).
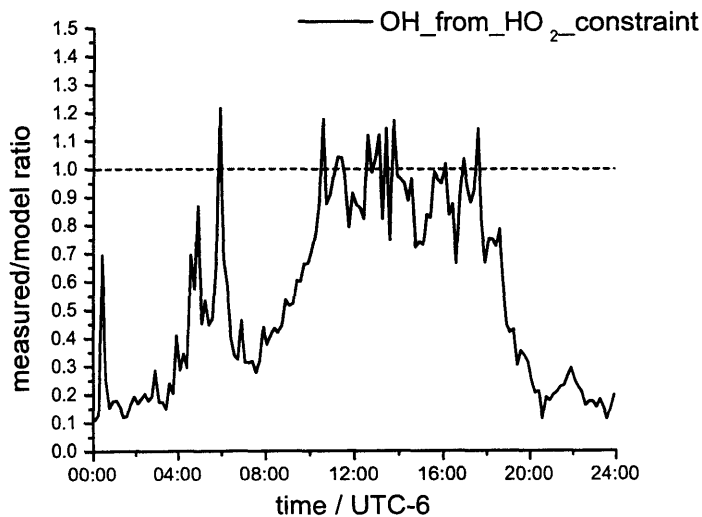
Figure 5-28: Observed to modeled ratios for OH concentrations calculated using a box model constrained for HO$_2$. The dashed line represents a ratio of 1:1 for the observed to modeled concentrations.

Radical Budget

Analysis of the radical budget for Case 2 focuses on the formation of OH from radical recycling. The same three pathways for OH recycling, from reaction of HO_2 with NO, O_3, and NO_3, demonstrate the same profiles (see Figure 5-29). The most notable difference is the increase in the radical flux, particularly in the most dominant pathway, HO_2 + NO. It appears that, with the introduced constraint of HO_2, this pathway has increased by a factor of 3. The peak of this reactivity occurs just before 08:00, and is most likely driving the unexpectedly high formation of OH in the morning rush hours just after sunrise.
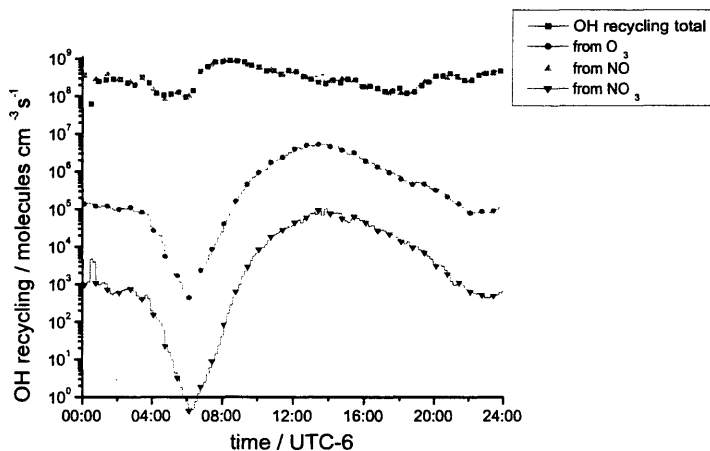
Figure 5-29: Comparison of three pathways for formation of OH radical from the reaction of NO, ozone, and nitrate radical with HO_2 (note logarithmic scale). The reaction with NO is clearly the dominant channel, as it varies from 2-7 orders of magnitude greater than the other channels. The difference between the profiles here and those in Figure 5-20 are the magnitudes of the various channels.

5.3.3 Case 3: Constraining OH

The constrained input for OH and the observed and modeled concentrations for HO_2 are presented in Figure 5-30. The modeled values generally agree with the observed diurnal profile of HO_2. The modeled values agree slightly better than in Case 1 (Section 5.3.1); however, there is still an under prediction by the model for HO_2

concentrations for the duration of the 24-hours modeled. The observed-to-modeled ratios for this case are presented in Figure 5-31. The model values are within the estimated uncertainty of the box model and measurements for the period 10:00-19:00. The observed-modeled ratios for Case 3 are remarkably similar in profile to those observed for HO_2 in Case 1; however, the ratios have actually been decreased with the introduction of the constraint on OH.

(a)   (b)
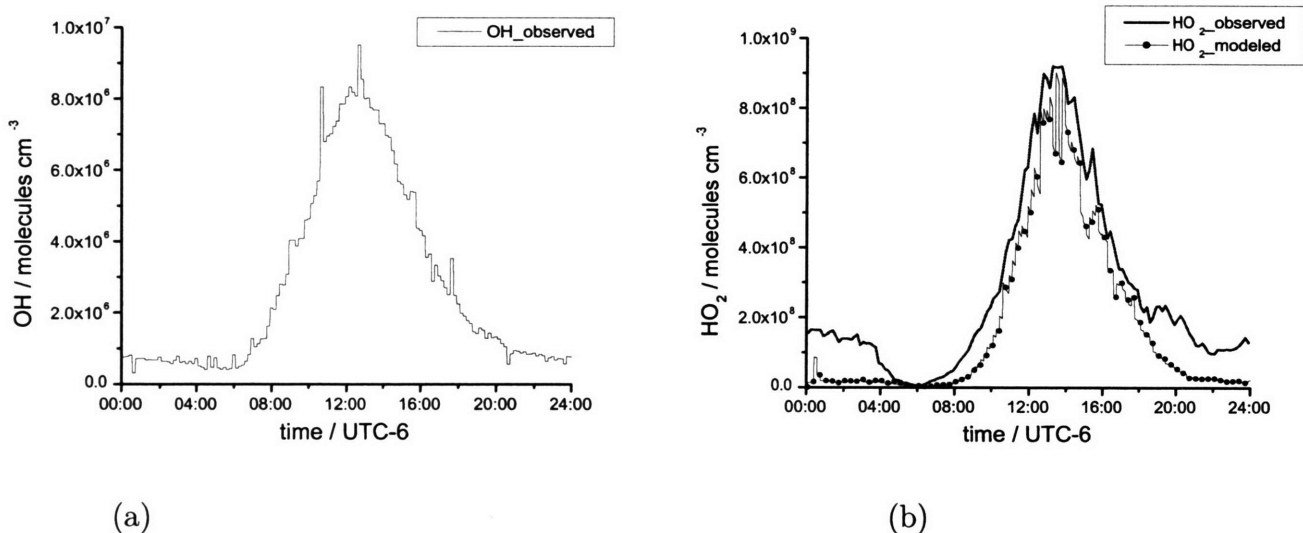
Figure 5-30: With OH constrained (a), observed HO_2 concentrations (b) from the 2003 MCMA field campaign are compared with concentrations calculated by the box model.

Radical Budget

The results of the modeling for HO_2 recycling in Case 3 are extremely similar to those from Case 1 when there were no constraints on HO_X.

5.3.4 Comparing Cases 1-3: What Can We Learn?

There are several points to be made when comparing the three different model runs described above. Firstly, with no HO_X constraints, the model here performs well in a high NO_X environment. This is important because the MCM project was designed with the intention of providing flexibility to the atmospheric modeling community so
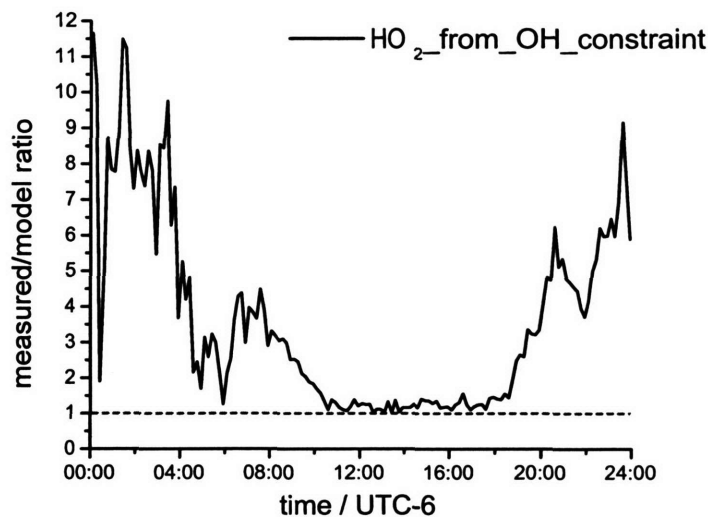
Figure 5-31: Observed to modeled ratios for HO_2 concentrations calculated using a box model constrained for HO_2. The dashed line represents a ratio of 1:1 for the observed to modeled concentrations.
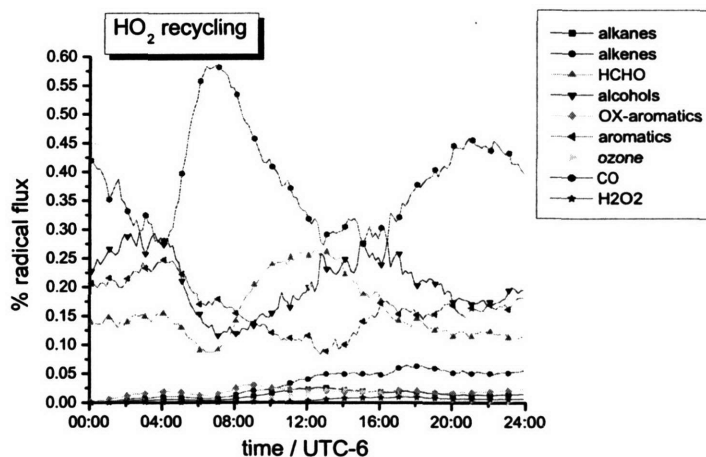
Figure 5-32: Comparison, as percentage contribution to the radical flux, of several HO_2 recycling channels for the box model using a constraint for OH. With the exception of the 'aromatics' and 'ox-aromatics' categories, the contributions from the groupings labeled as a VOC category (i.e. alcohols) are not from a reaction between OH and a primary VOC, but rather the reaction between OH and an oxidized species that is a product of a previous oxidation from that VOC category. The most dominant channels for HO_2 recycling are CO, HCHO, aromatics and oxidized alcohols, the same as for Case 1 in Section 5.3.1.

109

that urban, rural and remote atmospheric air masses could be modeled with the same near-explicit mechanism. The majority of studies having employed the MCM were in rural or remote areas [123], or are based on chamber experiments [99, 124].

For the unconstrained model in Case 1, although the model accurately predicts diurnal profiles for HO_x species, there is a general under estimation of the radical budget, particularly in the very early morning and at night. There is also a significant discrepancy in the radical budget for the period just after sunrise between 07:00 and 10:00. In chamber experiments by Bloss *et al.* it has been observed that the MCMv3.1 under estimates the oxidation capacity of the reactive system [99]. The same is observed here.

The added constraint of HO_2 actually downgrades the ability of the box model to predict the concentration of OH. It appears that the constraint on HO_2 increases the effects of radical recycling and contributes to the formation of OH in the early morning, at times prior to what is observed in the 2003 MCMA field campaign. The increase in the modeled values of OH during the early morning hours is to be expected when the model is constrained only for HO_2 . At early morning hours, the chain length - the average number of times a new OH radical will be recycled through the processes shown in Figure 5-1 - is very high, on the order of 100. When the chain length is high, the coupling between OH and HO_2 is strongest. That is, the formation of each radical is dominated by recycling processes, rather than new radical production from photolysis. Under these conditions, any change in HO_2, will affect the concentration of OH linearly, as it is one of the dominant pathways for OH formation. This is what is observed in the differences in the modeled OH concentration in Case 1 and 2: In Case 1, with no constraints, the model slightly under predicts the concentration of OH; in Case 2, when HO_2 is constrained (to higher values that what is predicted in Case 1), the model over predicts the concentration of OH by essentially the same factor that the HO_2 concentration is increased by the constraint. Case 2 mainly provides confirmation for this coupling of OH and HO_2 in the early morning hours; the increased over prediction of OH concentrations makes it difficult to extract other information from the output parameters.

The added constraint of OH improves the box model prediction of HO_2. The modeled concentrations of OH are only slightly lower for Case 1. When the concentrations are constrained to the slightly higher observed values, the agreement between observed and modeled HO_2 improves. This suggests that there may be some secondary recycling processes that facilitate the formation of HO_2 from the oxidation routes initiated by OH and VOCs. There were no significant differences immediately apparent in the profiles of HO_2 recycling; however, a closer look is warranted.

In the case of HO_2 recycling, the model predicts that the oxidation products from alcohols contribute as much to the radical flux as do aromatics. It also appears that alkenes and oxidized aromatic compounds play a minor role in the recycling at night.

The calculated values for RO_2 from each of the 3 cases presented above are shown in Figure 5-33. Each case demonstrates a similar profile, and it should be noted that RO_2 generally tracks the modeled diurnal profile of HO_2 very closely, with concentrations slightly higher. The diurnal profiles modeled are in good agreement with those observed elsewhere for organic peroxyl radicals [92]. The concentrations for the modeled RO_2 values when HO_X is unconstrained matches extremely well for when OH is constrained. The highest modeled values for RO_2 are reported for the case in which HO_2 is constrained. Based on the ability of each model case to reproduce observed parameters, it is suggested that the values of RO_2 from Case 2 are the most accurate.

5.3.5   Glyoxal Formation

The work here so far has focused on HO_X chemistry. The following investigation into the formation of glyoxal from VOC oxidation is meant to illustrate one of the many ways the box model can be used to further investigate the urban troposphere of the MCMA.

The role of VOCs in the formation of ozone is well understood [125]; however, control strategies for reducing air pollution require the identification of molecules that serve as indicators for VOC oxidation. Traditional oxidation indicators, such
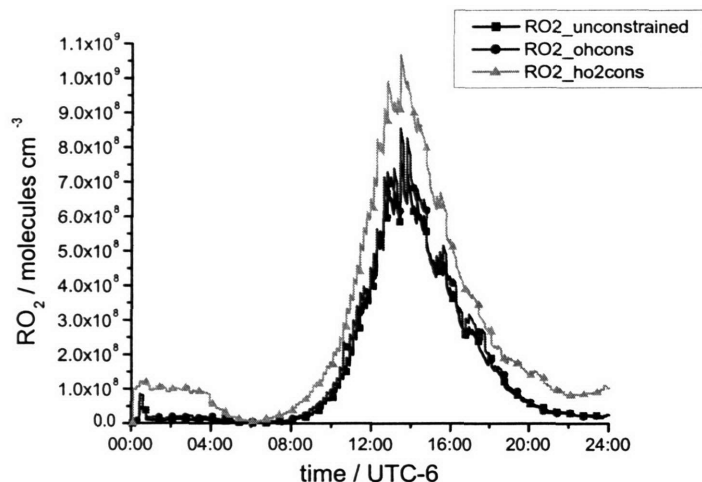
Figure 5-33: Calculated concentrations of organic peroxyl radicals, RO_2 for each of the 3 cases presented above. When HO_2 is constrained (triangles), the highest concentration of RO_2 is calculated. The concentrations for RO_2 when OH is constrained as compared to when neither HO_2 nor OH is constrained, are similar, and essentially indistinguishable.

as O_3, O_X ($= O_3 + NO_2$), HCHO, and MVK are affected by direct vehicle emissions [125]. Glyoxal is formed from the oxidation of numerous VOCs [108, 126, 127]. During the 2003 MCMA field campaign, Volkamer et al. [120] made the first direct ambient measurements of glyoxal in the atmosphere using the DOAS instrument described previously, and showed that it is essentially unaffected by direct vehicle emissions [120]. Elsewhere, Volkamer et al. [128] showed that current modeling capabilities to predict the sources of glyoxal from VOC oxidation requires further investigation. They go on to predict that models will significantly over estimate glyoxal formation because of the inclusion of secondary formation processes (even though they are experimentally unverified.) Similarly, glyoxal sinks are not well characterized; as additional losses (other than the gas phase sinks included in MCMv3.1) from dry deposition and secondary organic aerosol (SOA) formation are expected.

The average diurnal profile of glyoxal during the 2003 MCMA field campaign is shown in Figure 5-34. Data were provided by Rainer Volkamer and measured via DOAS. The modeled concentration of glyoxal for Cases 1 and 3, as well as a separate

112

version of the model that is constrained for both OH and HO_2 (Case 4), is compared to the average observed concentration in Figure 5-35. Case 2 was not used because the HO_2 constraint significantly increases OH production, which increases the oxidation capacity of the system and drastically skews the calculation of glyoxal.
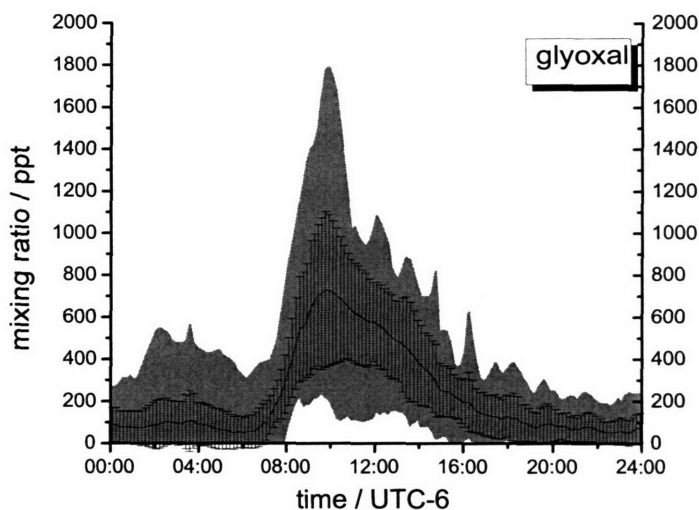
Figure 5-34: Diurnal profile of glyoxal as measured by DOAS during the 2003 MCMA field campaign. The shaded areas represent the maxima and minima values, and the bars represent one standard deviation of the measurements over the entire campaign. Data were provided by Rainer Volkamer at MIT.

Clearly, the prediction by Volkamer *et al.* regarding the over estimation of glyoxal formation seems to be accurate for the box model constructed for the MCMA. For Case 1, because there is a lower than observed concentration of OH, the peak modeled value is 2.1 times the observed values. For Cases 3 and 4, the formation of glyoxal is identical; the peak modeled value is about 3.4× the observed value. It is also apparent the background concentrations of glyoxal before sunrise are far too high: in Cases 3 and 4, the background is already at 1000 ppt, while Case 1 is at 500 ppt. In Cases 1, 3, and 4, the modeled peak of glyoxal is shifted by approximately 45 mins compared to the average observed peak. In Case 1, with no constraint on OH, the formation of glyoxal persists throughout the afternoon, and the only reason that the model does not predict a higher concentration is because of the dilution factor incorporated into
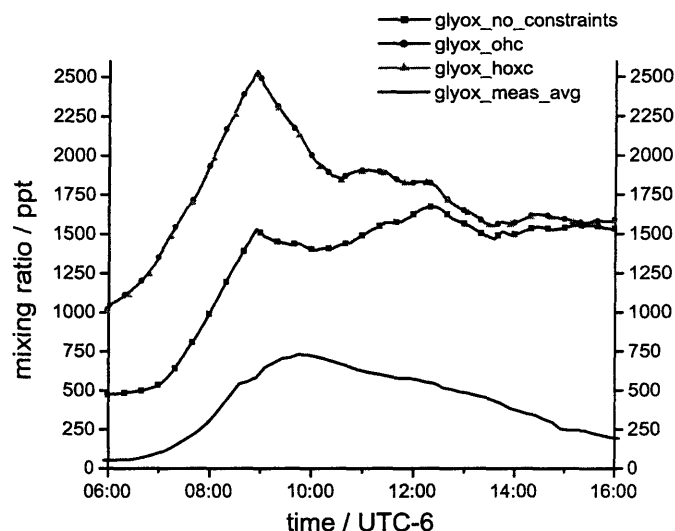
Figure 5-35: Comparison of measured glyoxal values ('glyox_meas_avg') to different modeled values. The different modeled values are based on different constraints used in the input parameters. The model runs with a OH constraint and the HO_X constraint are identical and over estimate the peak concentration of glyoxal by a factor of 3.5. The unconstrained model over estimates the peak of glyoxal by a factor of 2.1.

the mechanism (see Section 5.2.3 above). Based on the modeled values presented here, it is reasonable to confirm the prediction by Volkamer *et al.* that secondary formation of glyoxal in the MCMv3.1 results in an over prediction, and that there are missing sinks in the glyoxal chemistry. While experimental uncertainty may account for some of the differences between observed and modeled values, it is not significant enough to account for the entire difference. This suggests that further investigation into the loss of glyoxal in SOA formation and by dry deposition is required.

5.3.6 Estimated Uncertainty

The MCMv3.1 contains about 13500 reactions and 4500 species. Each of these changing species is determined by the kinetic rate coefficients, photolysis rate coefficients, branching ratios, and the input parameters that have been constrained. Carslaw *et al.* have performed a rigorous uncertainty analysis for an observationally constrained box model [129]. They determined the uncertainty in their box model with a Monte

114

Carlo method for sensitivity analysis. They report 2σ uncertainties of 31, 21, and 25 % for modeled concentrations of OH, HO_2, and $\Sigma(HO_2+RO_2)$ for clean air, and 42, 25, and 27 % for semi-polluted air. Thompson and Stewart [130] found that for higher NO_X conditions typical of an urban air mass, that the 1σ uncertainty for OH and HO_2 was 70 %. Using a RACM model, Shirley [131] has estimated the uncertainty to be 45 and 70 % for OH and HO_2, respectively, using a similar method to Carslaw et al..

Carslaw et al. employed MCMv3.0 in their calculation of the uncertainty for their modeled values of HO_X and RO_2. The box model constructed here also has a larger number of input parameters - 100+ parameters were constrained. Constraining the code using these parameters is a more accurate representation of the urban troposphere; however, it results in additional terms contribution to the uncertainty, based on the uncertainty of the measurements used. Considering estimated uncertainties from the various models and mechanisms presented above; the large suite of data employed for constraining the concentrations input species - measured and estimated; and the rate coefficients, photolysis coefficients, and other parameters used by the MCMv3.1, the estimated uncertainty for the OH, HO_2, and RO_2 values is 70 %.

5.4 Conclusion

A kinetic box model for the MCMA urban troposphere has successfully been constructed and employed to explore HO_X and VOC chemistry. Three cases were presented to highlight the performance of the box model in predicting HO_X concentrations. The model performs reasonably well for all three cases during the day time; however, discrepancies (often significant ones) remain between observed and modeled values. The modeled values for HO_X are consistently lower than those observed during the campaign, indicating that the radical budget - and the oxidation capacity - of the urban troposphere are not completely represented by the box model. This notion of missing reactivity has been observed in chamber experiments [99] and confirmed in field studies [132–134]. The drastic under estimation of the modeled values during

the night time suggests that night time sinks are too strong, or, more likely, that there is a night time source of HO_x that is not included. It has been shown that biogenic compounds (many of which were not measured during the 2003 MCMA field campaign) can contribute to peroxy radicals at night due to ozonolysis and reaction with NO_3 radicals [92]. In addition to comparing observed and modeled values of HOx, values for total organic peroxyl radicals, RO_2, were calculated to complement measured values for OH and HO_2.

The box model was used to confirm the prediction by Volkamer et $al.$ [128] that the concentration of glyoxal, a new indicator for VOC oxidation, is over estimated by the model for two reasons: secondary formation of glyoxal from recycling processes included in MCMv3.1 (that have not been experimentally verified), and a lack of sink terms (particularly heterogeneous chemistry). The qualitative features of glyoxal formation have been characterized; however, quantitative methods for determining the over estimation of the MCMv3.1 for the formation should provide the means to determine to what degree glyoxal sources and sinks are missing.

Further investigation of the oxidation scheme represented by the MCMv3.1 is needed. As the issue of missing reactivity as part of the overall radical budget is an important one, it would be valuable to quantify the missing reactivity of the code and determine the potential reactions or reactive pathways that require further laboratory studies. The mechanism has demonstrated an ability to reproduce the profiles of oxidized products in chamber experiments [99, 124]; however, it has not been tested in an urban setting. Oxidized products, other than glyoxal, including cresol and phenol, were directly measured by Rainer Volkamer at MIT via DOAS during the 2003 MCMA field campaign. These measurements are an excellent opportunity to examine oxidation channels in more detail. Further work with the box model should also focus on: 1) comparisons with lumped mechanisms; 2) using box model results to update lumped mechanisms; 3) compare and contrast daily chemistry, rather than the averaged profiles; 4) modeling NO_y chemistry; and 5) investigating night-time chemistry.

Chapter 6

Conclusion

Advancing our understanding of atmospheric chemistry is an essential component of addressing many public health and environmental concerns that exist today: air pollution, ozone depletion, and, not least, climate change. Sound science can play a major role in developing the appropriate strategy and/or policy to reduce the harmful effects of perturbations caused by anthropogenic forcing. The Montreal Protocol on Substances that Deplete the Ozone Layer [135], the international response to ozone depletion, is an excellent example of the scientific community providing policy makers the means to respond to an environmental hazard. The scientific basis for the protocol highlights the primary tools that are available to atmospheric chemists: Jones and Shanklin [136] have made field measurements demonstrating a continued decline of ozone over Antarctica. Previously, Molina and Rowland [137] demonstrated the catalytic destruction of ozone by man-made chlorofluorocarbons (CFCs) with a series of kinetics measurements in the laboratory. Meanwhile, Crutzen [138] demonstrated the depletion of ozone as a result of increased nitrogen oxides in the stratosphere with modeling. The synergistic effect of combining field measurements, laboratory measurements and modeling was on full display as policy makers gathered to combat the threat of ozone depletion.

The work presented here focused on the construction, operation, and improvement of an IntraCavity Laser Absorption Spectrometer, a valuable tool for measuring

spectroscopic features, kinetics, and reaction dynamics of trace species. The ICLA Spectrometer was coupled with a discharge flow system to measure the kinetics of the reaction intermediate, nitrosyl hydride (HNO). An updated reaction rate constant for the formation of HNO from hydrogen atoms, H, and nitric oxide, NO, in the presence of a third body, M, was reported. The successful implementation of a discharge flow apparatus expands the capabilities of the instrument to measure both spectroscopic information and reaction dynamics on a new scale. The system was further modified and enhanced with the introduction of a novel edge-tuner. The introduction of the tuner into the cavity enabled the operation of the broadband laser up to 1040 nm, which is further into the infrared than any reported measurements for an ICLA Spectrometer using a Ti:Sapphire lasing medium.

Laboratory measurements were complemented with a detailed analysis of a comprehensive box model of the urban troposphere in the Mexico City Metropolitan Area (MCMA), using the Master Chemical Mechanism (MCM) and data collected from a field campaign in 2003. The ability of the model to reproduce OH and HO_2 (= HO_X) measurements was presented, including an analysis of the role of various volatile organic compounds (VOCs) in HO_X formation. The results of the model are designed to provide feedback to experimentalists regarding missing reactivity and other areas that require further study.

As far as the operation of the ICLA Spectrometer is concerned, continued modifications and improvements may provide the means to make (more) detailed spectroscopic and kinetics measurements of trace species, such as the hydroperoxyl radical, at wavelengths longer than 1 μm. Of particular interest is the role of water vapor in the self-reaction of the hydroperoxyl radical, and the spectroscopic detection of a water-hydroperoxyl radical complex (H_2O-HO_2). In contrast, the heavy lifting for the construction of the box model has been done. At this point, it is trivial to tailor the model to explore more detailed information regarding the ability of the mechanism to reproduce measured compounds, as well as explore in further detail the role of individual VOCs in the formation of HO_X and ozone. For instance, it would be valuable to explore the ability of the model to predict the concentrations of oxidation

products such as cresol and phenol - each of which was measured during the 2003 field campaign. Both the ICLA Spectrometer and the box model described here are capable of making valuable and needed contributions that will facilitate the ongoing exchange between laboratory studies, modeling and field studies of the species that govern the chemical and physical processes in the atmosphere.

Appendix A

Modeling HNO formation in CHEMKIN®

As described in 3, we initially coupled the ICLAS laser with a flow tube with the intention of measuring the rate of reaction for

$$HNO + O_2 \rightarrow HO_2 + NO \qquad (A.1)$$

Using the experimental conditions as the parameters for a basic CHEMKIN® model and literature values [52, 56] for the rate of formation of HNO from the reaction,

$$H + NO \rightarrow HNO \qquad (A.2)$$

we determined that this reaction was not going to completion. The following calculations provided strong evidence that suggests we are not able to experimentally determine the rate for Reaction 3.4.

Based on Figure A-1, we estimated that the reaction between H and NO, in the flow system employed for the HNO+O_2 experiment, was only at 75-80% completion, depending on the pressure in the flow tube. Because Reaction 3.7 was unable to go to completion, it is likely that Reactions 3.8, 3.9, and 3.11 (all with rates higher than Reaction 3.7) were competing for hydrogen atoms. This complication is significant
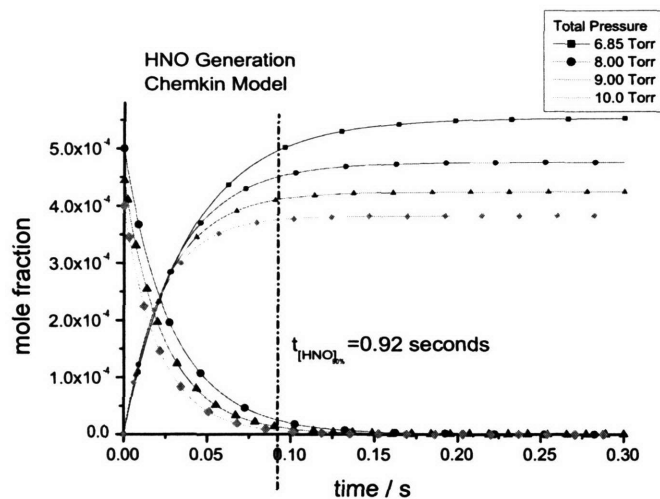
Figure A-1: Kinetic curves for the formation of HNO at various pressures employed in the HNO+O$_2$ experimental setup. The actual time that H atoms and NO had to react before being exposed to the oxygen was approximately 0.05 sec, nearly half the time required to reach [HNO]$_{90\%max}$.

enough to complicate the analysis of the HNO+O$_2$ measurements, as well as skew any results from the HNO+O$_2$ measurements.

Appendix B

"Discharge Flow Kinetic Measurements using IntraCavity Laser Absorption Spectroscopy (ICLAS)", Journal of Physical Chemistry, 109(17), 8358-8362 (2005).

Discharge—Flow Kinetics Measurements Using Intracavity Laser Absorption Spectroscopy[†]

P. Sheehy and J. I. Steinfeld*

Department of Chemistry, Massachusetts Institute of Technology, Cambridge, Massachusetts 02139

Received: June 16, 2004; In Final Form: October 26, 2004

Intracavity laser absorption spectroscopy ("ICLAS") has been demonstrated as a feasible detection method for trace species in a discharge flow tube. This implementation has been used to measure the rate of the reaction between atomic hydrogen and NO to form HNO in helium carrier gas. A reaction rate constant of $(4.3 \pm 0.4) \times 10^{-32}$ cm^6 molecule^{-2} s^{-1} at 295 K was measured for the reaction H + NO + M → HNO + M (M = He). The pressure and concentration range enabled by ICLAS detection has allowed us to limit reactive pathways that would inhibit the formation of HNO. The sensitivity of ICLAS, coupled with the versatility of the discharge flow technique, suggests that intracavity absorption spectroscopy will be a useful technique for kinetics measurements on free radicals and other reactive species.

1. Introduction

Trace amounts of reactive molecular free radicals play an integral role in the chemical properties of the atmosphere.[1] A principal objective of laboratory studies of free radicals is to obtain the spectroscopic and kinetic parameters necessary to understand their behavior in the atmosphere.[2] The high reactivity of free radicals and the difficulty in generating, and subsequently isolating, the radical for analysis present significant challenges to their detection. Absorption spectroscopy is a powerful technique for identifying and measuring the concentration of reactive species. One of the many implementations of this technique, time-resolved tunable diode laser absorption spectroscopy, has provided much valuable information about the production and decay of highly energetic, short-lived species.[3–5] Linear absorption spectroscopy possesses a fundamental limitation, however, which is that the absorbance given by the Beer—Lambert law[6]

$$A = -\ln(I/I_0) = \sigma N l_{\text{eff}} \tag{1}$$

is limited by the product of the absorption cross section σ, the number density of absorbers N, and the effective absorption path length l_{eff}. If either the cross section or species density is extremely small, then the achievable absorbance is likely to be too small to be easily detected above the background noise in the source and/or the detector. The latter constraint, viz., low number density, is frequently the case in measurements of free radical kinetics.

Cavity enhanced spectroscopy offers an approach to compensate low intrinsic absorbance by placing the sample of interest within the cavity of a laser. In the intracavity laser absorption spectroscopy (ICLAS)[7–11] experiment, light from a lasing medium reflects through the absorbing sample as many as 10^5 times, amplifying the absorbance of a weak absorber to a much greater extent than in traditional multipass absorption cells. The effective path length in the absorbing medium is given by

$$l_{\text{eff}} = (l/L)ct_g \tag{2}$$

where l is the absolute path length through the absorbing sample, L is the total cavity length, c is the speed of light, and t_g is the generation time in the ICLAS laser.

We have coupled our ICLAS system to a discharge-flow apparatus[12,13] and measured the formation kinetics of HNO from atomic hydrogen and nitric oxide as a test of kinetics using intracavity absorption spectroscopy (KICAS). The results indicate that KICAS will be a promising method for carrying out kinetics measurements on weakly absorbing species. A related technique, simultaneous kinetics and ring-down (SKaR) has recently been reported by Brown et al.[14] In the latter approach, the reaction being studied is enclosed in a Cavity Ring-Down cell which is optically coupled to a pulsed laser.

2. Experimental Section

The ICLAS system used in these experiments has been previously described.[15,16] A traveling-wave, ring configuration was utilized for these measurements (Figure 1a). The horizontally polarized output of a 15 W argon ion laser (Coherent INNOVA Sabre DBW15) pumped a 5 × 15 mm Brewster cut, Ti:sapphire rod (AM), situated between two spherical folding mirrors (FM1 and FM2). A VWR Scientific Products chiller was used to maintain a temperature of 13 °C for the Ti:sapphire rod. The pump beam was focused on the gain medium by a focusing lens (FL). A wedged, horizontal polarizer (P) and a Faraday rotator (FR) were inserted into the short arm of the cavity, between the first high reflector (HR1) and the crystal (AM). Two high reflectors (HR2 and HR3) are used to compensate for the rotation of polarized light induced by the Faraday rotator and to ensure a unidirectional, traveling-wave. The height of the second high reflector (HR2) is adjustable to optimize the compensation. The distance between HR3 and the output coupler (OC) make up the long arm of the cavity, including the sample cell.

The Ti:sapphire laser was continuously tunable between 700 and 1000 nm. The laser was operated around 750 nm to access the desired HNO transition. Both the high reflectors and the folding mirrors had better than 99.9% reflectivity, whereas the three output couplers had better than 98% reflectivity. Tuning within a given wavelength region was performed by rotating or translating a pellicle beam splitter inserted into the short arm of the cavity.

Discharge−Flow Kinetics Measurements Using ICLAS

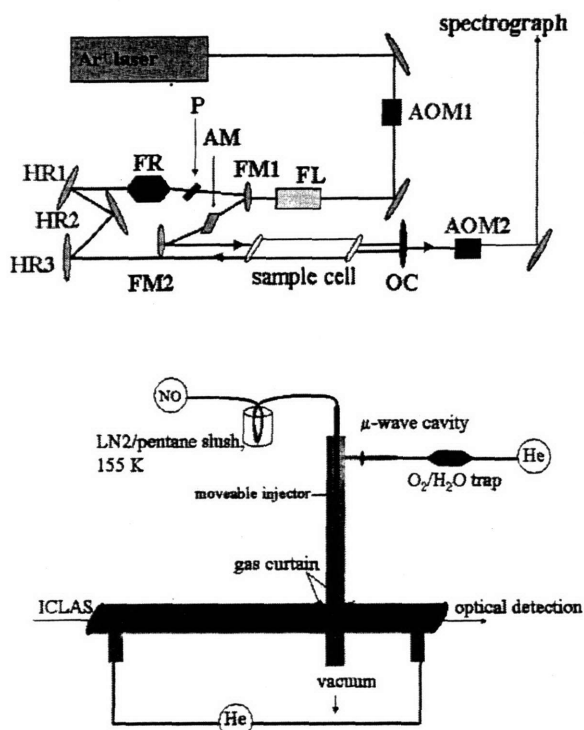*J. Phys. Chem. B, Vol. 109, No. 17, 2005* **8359**

Figure 1. Apparatus for carrying out kinetics using intracavity absorption spectroscopy. (a) Traveling-wave, ring configuration of the ICLAS spectrometer. (b) Flow apparatus used for measuring HNO formation kinetics using the ICLAS spectrometer.

Large wedge windows with 2 in. diameter, 0.5 in. thickness, and a 1° wedge (CVI Laser Corp.) were used for the sample cells. The entire cavity of the laser, except for the sample cell, was housed within a constructed purge box. During experiments the box was purged with argon to remove residual absorbers, such as water and oxygen. The concentrations of these absorbers were reduced by 3 orders of magnitude.

The generation time of the laser was controlled by two acousto-optic modulators (AOM1 and AOM2). The first gate, AOM1 (IntraAction Corp. model ASM-802B39), directed the pump laser onto the Ti:sapphire gain medium, whereas the second gate, AOM2 (model ASM-40N), directed the output of the laser to the spectrograph. A 2.5 m echelle grating spectrograph dispersed the laser output, and the spectrally dispersed laser output was recorded with a linear silicon diode array (3,724 pixel Toshiba TCD1301D). The spectrograph could be operated in single, double, or triple pass mode by manually tilting the grating. Alignment of the spectrograph is performed with a 4 mW HeNe laser (Uniphase model 1057-0). The AOMs, the grating position, and the diode array were digitally controlled by software in Delphi programming language. The traveling-wave, ring configuration of the ICLAS laser resulted in effective path lengths of up to 3×10^4 km and detectable absorption coefficients on the order of 10^{-11} cm^{-1}.

The silicon linear diode array recorded a spectrum of photon count versus pixel number. The x-axis was calibrated for wavenumber and was linearized to account for the diffraction grating's wavelength-dependent dispersion. The y-axis was normalized to determine transmittance. The wavenumber calibration of ICLAS spectra was performed using nearby transitions from residual water or oxygen absorption lines. Although the cavity of the ICLAS laser was purged with argon, the path from the output coupler to the linear diode array detector was not purged. The 10 m path length between the output coupler and

the diode array was sufficient to allow for the detection of both oxygen and water lines. Depending on the spectral region that the system was set up for, the known frequencies[17] of these lines were used to calibrate the spectra. In the case that the system was operated in a spectral region where oxygen and water absorption lines were insufficiently intense, an iodine absorption cell could be coupled with ICLAS to calibrate the spectra.[18]

The apparatus used for kinetic measurements is shown in Figure 1b. Experiments were carried out in a Pyrex tube (1.8 cm i.d., 65 cm long) connected to a T-cross that served as the axis for the optical detection system. Helium was used as the main carrier gas (BOC Gases, 99.999%). The flow tube gas was pumped by a Welch Duo-seal vacuum pump (500 L min^{-1}). Pressures were measured using a 0−100 Torr MKS Baratron manometer. The flow of the helium carrier gas was monitored using a TubeCube A7940HA-5 flow meter. The flow of nitric oxide was monitored using a Sierra Instruments Side Trak mass flow meter.

Hydrogen atoms were injected through a sidearm inlet located at the rear of the flow tube. The excess reactant, NO, was injected through a moveable inlet. The total flow through the injector was kept below 10% of the main carrier gas flow. Hydrogen, H$_2$, exists as a 1 ppm impurity in grade 5.0 helium.[19] The number density of the helium carrier gas is $\approx 10^{17}$ molecules cm^{-3}. This corresponds to a molecular hydrogen number density of $\approx 10^{11}$ molecules cm^{-3}. Atomic hydrogen was generated by passing the helium carrier gas through a microwave discharge. The microwave discharge cavity was cooled with a stream of nitrogen to maximize atomic hydrogen yields.[20] The helium was passed through an OxiClear Disposable Gas Purifier to effectively reduce the concentrations of water and oxygen. The efficiency of the microwave discharge cavity in dissociating molecular hydrogen may vary from day-to-day; however, regardless of potential day-to-day variations, between 1 and 10% of the molecular hydrogen should be atomized to generate H-atoms. This corresponds to $\approx 10^9 - 10^{10}$ molecules cm^{-3} of atomic hydrogen generated in the flow tube.

To remove NO$_2$, a purified stream of NO was prepared by passing the gas through a liquid nitrogen and pentane (LN$_2$/pentane) slush cooled to approximately 165 K. The temperature of the LN$_2$/pentane slush was monitored with a Fluke 51 Series II digital thermometer. Only a trace amount of NO$_2$ is necessary to affect the formation kinetics of HNO. The rate constant for the reaction between atomic hydrogen and NO$_2$ is several orders of magnitude greater than the HNO formation rate; so even though NO is present in excess, NO$_2$ still competes for hydrogen atoms. Minimizing, and essentially eliminating, NO$_2$ as an impurity is essential. Within the flow tube, the density of NO varied from 1×10^{16} to 3×10^{16} molecule cm^{-3}.

The ICLAS laser was constructed with Brewster surfaces to minimize losses. Two large wedge windows, 2 in. diameter, 0.5 in thick and a 1° wedge, were used for the sample cell. To prevent the diffusion of HNO into the sidearms, potentially contaminating the windows and decreasing the sample cell window transmission, a "gas curtain" of helium was introduced. Eliminating diffusion to the sidearms also eliminates the potential for inaccurate measurements of HNO number density as a result of an increased effective path length. The total flow rate was around 20 SLPM of air, corresponding to a linear flow rate of approximately 5×10^3 cm s^{-1}. Measurements were conducted at total pressures of both 13.85 and 24.00 Torr.
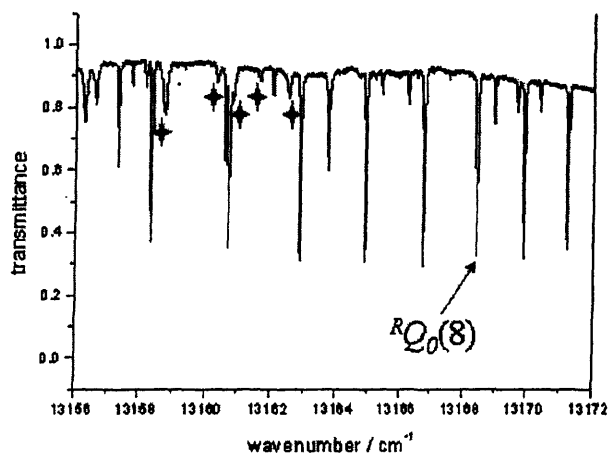
Figure 2. ICLAS spectrum of HNO used for kinetics measurements. The five transitions marked with a four-point star are oxygen absorption peaks that are used for frequency calibration of the spectrum.

3. HNO Spectroscopy

Nitrosyl hydride, HNO, was chosen to demonstrate the capability of ICLAS to measure kinetics in a discharge flow system. The HNO molecule was selected for a variety of reasons—it is a key intermediate in number of reactions relevant to the fields of astrophysics, combustion chemistry, and atmospheric chemistry.[21-26] HNO has a strong electronic transition within the spectral range of the Ti:sapphire-based ICLA Spectrometer. The molecule has a large absorption cross-section — requiring only trace amounts of HNO to conduct the necessary experiments ($\sigma > 10^{-17}$ cm^2 molecule^{-1}). In a setup with an occupation ratio of ~35% and a generation time of 500 μs, a detection limit for HNO of ~10^7 molecules cm^{-3} is achievable with ICLAS.

The spectroscopy of HNO has been measured extensively by both absorption[27-29] and emission methods.[30-32] The molecule has a bent equilibrium geometry and C_s symmetry in its three lowest lying electronic states: $\tilde{X}^1A'$, $\tilde{A}^1A''$, and $\tilde{a}^3A''$. HNO is a slightly asymmetric near prolate rotor ($\kappa = -0.988$). Only c-type transitions have been observed for the $\tilde{A} \leftarrow \tilde{X}$ transition, indicating the transition moment is perpendicular to the plane of the molecule. Kinetic measurements of HNO were made using the (000) ← (000) band of the $\tilde{A}^1A'' \leftarrow \tilde{X}^1A'$ electronic transition, centered at 13 154.38 cm^{-1}. The $^RQ_0(8)$ line of the $\Delta K_a'' = 0$ subband at approximately 13 168 cm^{-1} was used most often for monitoring HNO kinetics because of the lack of interference from other HNO lines and oxygen transitions, as well as sufficient oxygen at nearby frequencies to accurately calibrate the transition (Figure 2). Several other spectral lines in the $\Delta K_a'' = 1$ subband were interrogated and yielded kinetic plots essentially similar to those presented; because the $\Delta K_a'' = 1$ subband lies in a region in which there are no nearby oxygen calibration lines, the $\Delta K_a'' = 0$ subband was chosen for detailed measurements.

The absorption cross-section of the $^RR_3(6)$ transition of the (100) ← (000) band of HNO is reported in the literature as 3.3 × 10^{-20} cm^2 molecule^{-1} at room temperature.[33] Using known Franck—Condon factors[34] and rotational line strength factors calculated using expressions derived by Lide,[35] the absorption cross-section of the $^RQ_0(8)$ transition of the (000) ← (000) band of HNO was calculated to be 4.2 × 10^{-17} cm^2 molecule^{-1}, with an uncertainty of approximately 20%. This calculated cross-section provided the means to determine the number density of HNO for kinetic measurements.
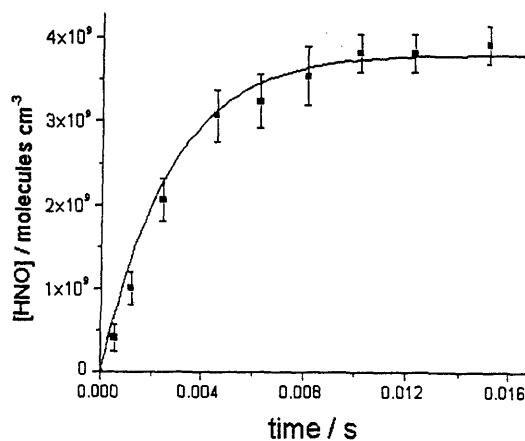
Figure 3. Sample kinetic plot at 13.85 Torr total pressure showing measured HNO number densities and a pseudo-first-order fit to the data. Error bars represent one standard deviation.

4. H + NO + M Kinetics

The following reactions are relevant to the study of HNO formation using ICLAS as the detection method:

$$H + NO + M \xrightarrow{k_1} HNO + M \qquad (R1)$$

$$H + H + M \xrightarrow{k_2} H_2 + M \qquad (R2)$$

$$HNO + H \xrightarrow{k_3} H_2 + NO \qquad (R3)$$

$$HNO + wall \xrightarrow{k_w} decay \qquad (R4)$$
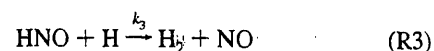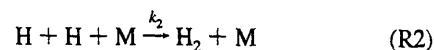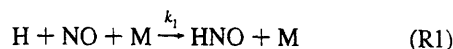
The procedure used for determining the rate of reaction (R1) with this method is similar to that commonly used for low-pressure flow tubes;[12,13] however, the product, rather than reacting species, is monitored. Nitric oxide and helium were injected at a fixed rate, and their number densities were calculated assuming complete mixing in the region downstream of the injector. In each reaction, both NO and He (carrier gas = M) were present in several orders of magnitude greater than the estimated hydrogen atom concentration, creating pseudo-first-order conditions. The plasma discharge was initiated or "lit" and the position of the moveable injector was varied to generate a series of kinetic curves; an example is shown in Figure 3. A nonlinear least-squares fit was then performed in Microcal Origin. The data were fit to the following expression:

$$[HNO]_t = \frac{k_{eff}[H]_o}{k_w - k_{eff}}(e^{-k_{eff}t} - e^{-k_w t}) \qquad (3)$$

where $k_{eff} = k_1[NO][M]$ (M = He), and $[H]_o$ is the initial concentration of atomic hydrogen in the flow tube in the absence of nitric oxide. The initial concentration of atomic hydrogen was not explicitly determined. The input value for $[H]_o$ was assumed to be approximately equal to $[HNO]_{z\ max}$ where z is the distance between the injector and the ICLAS axis of detection. When z was maximized, neither an increase in background pressure nor an increase in the concentration of NO yielded a higher concentration of HNO. Both of these indicators confirm that $[HNO]_{maximum} \approx [HNO]_{z\ max}$. It was also assumed that all the [HNO] formed at z_{max} was from the titration of atomic hydrogen with nitric oxide. This assumption leads to $[HNO]_{max} \approx [H]_o$. The number densities calculated for [HNO] are in good agreement with expected values: the concentration

of atomic hydrogen generated from the discharge was estimated between 10^9–10^{10} molecules cm^{-3} and the calculated number densities for $[HNO]_{max}$ vary between 3 and 5×10^9 molecules cm^{-3}.

Considering potential systematic errors in the measurement of gas flows, pressure, and detector signal, as well as uncertainties associated with the Franck—Condon factors used to calculate the HNO number density, it is estimated that the rate constant can be determined with an accuracy of ±20%.

The termolecular rate constant reported in Table 1 is $(4.3 \pm 0.4) \times 10^{-32}$ cm^6 molecule^{-2} s^{-1}. Clyne and Thrush[36] and Miyazaki and Takahashi[37] have determined the value of k_1 by measuring the decrease in HNO emission intensity in a discharge-flow system. They report values of $(1.8 \pm 0.3) \times 10^{-32}$ and 3.0×10^{-32} cm^6 molecule^{-2} s^{-1}, respectively. These are the only two values in the literature that report the formation of HNO with helium as a carrier gas. The work of Miyazaki and Takahashi requires a complicated data reduction scheme,[37] making a comparison of values extremely difficult.

Although similar concentrations of nitric oxide were used in all experiments, the concentration of atomic hydrogen in the previous work was approximately 0.5–2% of the total flow.[36–39] In this work, the concentration of atomic hydrogen was reduced to approximately 1×10^{-4}% of the total flow. Minimizing the concentration of atomic hydrogen limits the potential for other formation or recombination reactions involving atomic hydrogen. Similarly, limiting the concentration of atomic hydrogen limits the formation of HNO. This prevents potential losses of HNO via wall loss, self-reaction, or other successive reactions.

In the KICAS flow tube, the absorption spectrum of HNO is not observed if the nitric oxide stream is not purified by means of the LN2/pentane cold bath. Nitrogen dioxide exists as an impurity in the stream of NO from the cylinder. Nitrogen dioxide reacts much faster with atomic hydrogen than nitric oxide does. A rigorous purification of the NO stream is essential to measuring the rate parameters of (R1) and (R4) accurately. Clyne and Thrush make a similar observation in that they are unable to detect the "glow intensity" due to the emission of HNO at increased concentrations of nitrogen dioxide.[36]

The work of Clyne and Thrush[36,38] neglects to account for any potential wall loss—for both HNO and atomic hydrogen. In our system, it is possible that the wall is acting as a third body and contributing to the stabilization of the electronically excited HNO* molecule, as well as acting as a loss site. Similar recombination phenomena are possible with atomic hydrogen. The only indication of sensitivity to detecting HNO in the literature is given by observations associated with the steady-state concentration of HNO being much less than $0.2[NO]$.[36,38] A rough estimate of the detection sensitivity reveals that the HNO was observed in concentrations around 10^{12}–10^{13} molecules cm^{-3}, much higher than the concentrations reported here. In the present work, we effectively reduced the concentration of HNO so that we could isolate the formation of HNO, followed by a slow wall reaction. At higher concentrations of HNO, it is unlikely that the slow self-reaction,
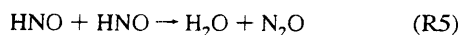
$$HNO + HNO \rightarrow H_2O + N_2O \qquad (R5)$$

becomes significant; however, it is likely that higher concentrations of HNO will affect the fast reaction,

$$HNO + H \rightarrow H_2 + NO \qquad (R3)$$
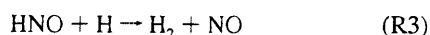
Although (R3) is and should be considered in the study by Clyne and Thrush.[36] the potential of this reaction to skew the measured

TABLE 1: Observed Termolecular Rate Constants at 13.85 and 24.00 Torr for the Reaction

$$H + NO \xrightarrow{M} HNO$$

pressure, Torr	velocity, 10^3 cm s^{-1}	$[H]_o$, 10^9 cm^{-3}	$k_1 \pm \sigma$, 10^{-32} cm^6 s^{-1}	$k_{wall} \pm \sigma$, s^{-1}
13.85	5.3	4.15	3.0 ± 0.3	0.6 ± 0.3
	4.9	4.01	4.1 ± 0.4	0.5 ± 0.4
24.00	5.1	3.86	5.7 ± 0.4	0.7 ± 0.2
	5.1	3.92	4.7 ± 0.5	0.7 ± 0.4
	5.2	4.01	4.1 ± 0.4	0.5 ± 0.5

concentration of HNO in the ICLAS system is minimized by manipulating the number densities and flows such that $[NO] \gg [H], [HNO]$.

The total pressure in the system employed by Clyne and Thrush was 5–10 times lower than the pressures used in this experiment. Under the experimental conditions reported by Clyne and Thrush, it is interesting to note that $k_3 > k_2[M]$. This is not the case in our experiment. By limiting the concentration of atomic hydrogen and the formation of HNO, we were able to observe a steady-state concentration of HNO (at about 6 ms of reaction time).

The wall loss reaction is reported with high uncertainties because of the relatively small effect it has on the simulated curve (vide infra) up to a value of 1 s^{-1}. The upper limit for the rate constant of the wall reaction for this system is reported as 1 s^{-1}, and is most likely in the range 0.2–0.7 s^{-1}, which is in good agreement with other reported values.[40,41] At values above 1 s^{-1}, the curve fitting function, eq 3, begins to demonstrate behavior inconsistent with the experimental observations. On the time scale of the experiment (~20 ms), a value greater than 1 s^{-1} would demonstrate a slow, but detectable decline in the concentration of HNO. All of the experimental data at varying pressures observed here supports a slower decay associated with the wall reaction.

The Aurora application, part of the CHEMKIN software package,[42] simulates the time evolution or steady state of a well mixed reactor. The Aurora application was used to model the series of reactions ((R1)–(R4)) in the HNO reaction system to compare numerically modeled kinetics curves with the experimental curves obtained from the KICAS measurements.

The rates used in the simulations were: $k_1 = 4.3 \times 10^{-32}$ cm^6 molecule^{-2} s^{-1}, $k_2 = 6 \times 10^{-33}$ cm^6 molecule^{-2} s^{-1}, $k_3 = 1.7 \times 10^{-12}$ cm^3 molecule^{-1} and $k_w = 0.5$ s^{-1}. The application was run under conditions appropriate to the experiments reported above. The simulated kinetics curves showed good agreement with the experimental data.[43]

5. Discussion

ICLAS has been demonstrated as a feasible detection method for trace species in a discharge flow tube. This implementation has been used to measure the rate of the reaction between atomic hydrogen and NO to form HNO in helium carrier gas. A reaction rate constant of $(4.3 \pm 0.4) \times 10^{-32}$ cm^6 molecule^{-2} s^{-1} at 295 K was measured for the reaction $H + NO + M \rightarrow HNO + M$ (M = He). The pressure and concentration range enabled by ICLAS detection has allowed us to limit reactive pathways that would inhibit the formation of HNO. The sensitivity of ICLAS, coupled with the versatility of the discharge flow technique, suggests that intracavity absorption spectroscopy will be a useful technique for kinetics measurements on free radicals and other reactive species.

The KICAS method described here is essentially equivalent to similar methodologies used in kinetic studies employing

cavity ring down spectroscopy in a pulsed-photolysis or discharge-flow configuration. The primary difference between KICAS and CRDS-based experiments is the accessible spectral range of the spectroscopic system employed. The SKaR method recently reported by Brown et al.[14] represents an analogous methodology. The sensitivity of both SKaR and KICAS are comparable. One specific advantage that KICAS or a conventional configuration for CRDS detection may have over SKaR is the time scale accessible for kinetic measurements, as SKaR is inherently limited by the empty cavity time constant (τ_0) which the authors state is variable up to hundreds of microseconds. To be a candidate for SKaR, a reaction must have kinetics on the order of τ_0. The experiment reported here was carried out at time scales up to 20 ms, well beyond the range of SKaR. On the other hand, SKaR is an attractive option for kinetics experiments at short time scales, as a laser light pulse into the cavity initiates the experiment and controls the time scale, whereas KICAS requires a more complicated discharge flow configuration to operate at shorter time scales. Both methodologies have their merit, and should be considered complementary.

References and Notes

(1) Seinfeld, J. H.; Pandis, S. N. *Atmospheric Chemistry and Physics: From Air Pollution to Climate Change*; Wiley: New York, 1998.

(2) Lightfoot, P. D.; Cox, R. A.; Crowley, J. N.; Destriau, M.; Hayman, G. D.; Jenkin, M. E.; Moortgat, G. K.; Zabel, F. *Atmos. Environ. Part A — Gen. Top.* **1992**, *26*, 1805.

(3) Sedlacek, A. J.; Weston, R. E., Jr.; Flynn, G. W. *J. Chem. Phys.* **1991**, *94*, 6483.

(4) Hewitt, S. A.; Zhu, L.; Flynn, G. W. *J. Chem. Phys.* **1992**, *97*, 6396.

(5) Mullin, A. S.; Michaels, C. A.; Flynn, G. W. *J. Chem. Phys.* **1995**, *102*, 6032.

(6) Beer, A. *Ann. Phys.* **1852**, *86*, 78.

(7) Pakhomycheva, L. A.; Sviridenkov, E. A.; Suchkov, A. F.; Titova, L. V.; Chrilov, S. S. *JETP Lett.* **1970**, *12*, 43.

(8) Peterson, A. *J. Opt. Soc. Am.* **1971**, *61*, 746.

(9) Hänsch, T. S.; Schawlow, A. L.; Toschek, P. E. *IEEE J. Quantum Electron.* **1972**, *8*, 802.

(10) Kachanov, A. A.; Charvat, A.; Stoeckel, F. *J. Opt. Soc. Am. B* **1994**, *11*, 2412.

(11) Campargue, A.; Stoeckel, F.; Chenevier, M. *Spectrochim. Acta Rev.* **1990**, *13*, 69.

(12) Howard, C. J. *J. Phys. Chem.* **1979**, *83*, 3.

(13) Seeley, J. V.; Jayne, J. T.; Molina, M. J. *J. Phys. Chem.* **1996**, *100*, 4019.

(14) Brown, S. S.; Ravishankara, A. R.; Stark, H. *J. Phys. Chem. A* **2000**, *104*, 7044.

(15) Yang, S.f.; Canagaratna, M. R.; Witonsky, S. K.; Coy, S. L.; Steinfeld, J. I.; Field, R. W.; Kachanov, A. A. *J. Mol. Spectrosc.* **2000**, *201*, 188.

(16) Witonsky, S. K.; Canagaratna, M. R.; Coy, S. L.; Steinfeld, J. I.; Field, R. W.; Kachanov, A. A. *J. Chem. Phys.* **2001**, *115*, 3134.

(17) Rothman, L. S.; Rinsland, C. P.; Goldman, A.; Massie, S. T.; Edwards, D. P.; Flaud, J. M.; Perrin, A.; Camy-Peyret, C.; Dana, V.; Mandin, J. Y.; Schroeder, J.; McCann, A.; Gamache, R. R.; Watson, R. B.; Yoshino, K.; Chance, K. V.; Jucks, K. W.; Brown, L. R.; Nemtchinov, V.; Varanasi, P. *J. Quant. Spectrosc. Rad. Transfer* **1998**, *60*, 665.

(18) Gerstenkorn, S.; Luc, P.; Verges, J. *Atlas du Spectre d'Absorption de la Molecule d'Iode: 7200—11200 cm^{-1}*, CNRS: Paris, 1993.

(19) Private communication from J. Jordan, BOC Gases Inc.

(20) Stonge, L.; Moisan, M. *Plasma Chem. Plasma Proc.* **1994**, *14*, 87.

(21) DeMore, W. B.; Sander, S. P.; Golden, D. M.; Hampson, R. F.; Kurylo, M. J.; Howard, C. J.; Ravishankara, A. R.; Kolb, C. E.; Molina, M. J. *Chemical Kinetics and Photochemical Data for Use in Stratospheric Modeling*; JPL: Pasadena, CA, 1997; Publication 97-4.

(22) Graedel, T. E.; Langer, W. D.; Frerking, M. A. *Astrophys. J. Supp. Ser.* **1982**, *48*, 321.

(23) Viala, Y. P. *Astron. Astrophys. Supp. Ser.* **1986**, *64*, 391.

(24) Miller, J. A.; Bowman, C. T. *Prog. Energy Combust. Sci.* **1989**, *15*, 287.

(25) Soto, M. R.; Page, M.; McKee, M. L. *Chem. Phys. Lett.* **1991**, *187*, 335.

(26) Viereck, R. A.; Bernstein, L. S.; Mende, S. B.; Murad, E.; Swenson, G. R.; Pike, C. P. *J. Spacecraft Rockets* **1993**, *30*, 724.

(27) Dalby, F. W. *Can. J. Phys.* **1958**, *36*, 1336.

(28) Bancroft, J. L.; Hollas, J. M.; Ramsay, D. A. *Can. J. Phys.* **1962**, *40*, 322.

(29) Johns, J. W. C.; McKellar, A. R. W. *J. Chem. Phys.* **1977**, *66*, 1217.

(30) Dixon, R. N.; Noble, M.; Taylor, C. A.; Delhoume, M. *Discuss. Faraday Soc.* **1981**, *71*, 125.

(31) Dixon, R. N.; Jones, K. B.; Noble, M.; Carter, S. *Mol. Phys.* **1981**, *42*, 455.

(32) Obi, K.; Matsumi, Y.; Takeda, Y.; Mayama, S.; Watanabe, H.; Tsuchiya, S. *Chem. Phys. Lett.* **1983**, *95*, 520.

(33) Cheskis, S. G.; Nadtochenko, V. A.; Sarkisov, O. M. *Int. J. Chem. Kinet.* **1981**, *13*, 1041.

(34) Mordaunt, D. H.; Flothmann, H.; Stumpf, M.; Keller, H. M.; Beck, C.; Schinke, R.; Yamashita, K. *J. Chem. Phys.* **1997**, *107*, 6603.

(35) Lide, D. R. *J. Chem. Phys.* **1952**, *20*, 1761.

(36) Clyne, M. A. A.; Thrush, B. A. *Discuss. Faraday Soc.* **1962**, *33*, 139.

(37) Miyazaki, S.; Takahashi, S. *Mem. Def. Acad. Jpn.* **1969**, *9*, 643.

(38) Clyne, M. A. A.; Thrush, B. A. *Trans. Faraday Soc.* **1961**, *57*, 1305.

(39) Hartley, D. B.; Thrush, B. A. *Proc. R. Soc. A* **1967**, *297*, 520.

(40) Bryukov, M. G.; Kachanov, A..A.; Timonnen, R.; Seetula, J.; Vandoren, J.; Sarkisov, O. M. *Chem. Phys. Lett.* **1993**, *208*, 392.

(41) Callear, A. B.; Carr, R. W. *J. Chem. Soc., Faraday Trans.* **1975**, *71*, 1603.

(42) Distributed by Reaction Design, Inc.

(43) P. Sheehy, Ph.D. Thesis, Massachusetts Institute of Technology, 2005.

Bibliography

[1] J. H. Seinfeld and S. N. Pandis, *Atmospheric Chemistry and Physics : From Air Pollution to Climate Change*. New York: Wiley, 1998.

[2] P. D. Lightfoot, R. A. Cox, J. N. Crowley, M. Destriau, G. D. Hayman, M. E. Jenkin, G. K. Moortgat, and F. Zabel, "Organic peroxy-radicals - kinetics, spectroscopy and tropospheric chemistry," *Atmospheric Environment Part A-General Topics*, vol. 26, no. 10, pp. 1805–1961, 1992.

[3] I. Newton *Trans. R. Soc. Lond.*, vol. 6, p. 3075, 1671.

[4] G. Kirchoff and R. Bunsen *Philos. Mag.*, vol. 33, p. 329, 1861.

[5] A. Walsh *Spectrochimica Acta*, vol. 7, p. 108, 1955.

[6] A. Beer *Ann. Physik*, vol. 86, p. 78, 1852.

[7] J. White *Optical Society of America*, vol. 32, p. 285, 1942.

[8] T. H. Maiman *Nature*, vol. 187, p. 493, 1960.

[9] C. Townes and A. Schawlow, "Infrared and optical masers," *Physical Review*, vol. 112, no. 6, p. 1940, 1958.

[10] L. Pakhomycheva, E. Sviridenkov, A. Suchkov, L. Titova, and S. Churilov *JETP Letters*, vol. 12, p. 43, 1970.

[11] A. Peterson *J. Opt. Soc. Am.*, vol. 61, p. 746, 1971.

[12] T. Hänsch, A. Schawlow, and P. Toschek *IEEE J. Quantum Electron.*, vol. 8, p. 802, 1972.

[13] S. F. Yang, M. R. Canagaratna, S. K. Witonsky, S. L. Coy, J. I. Steinfeld, R. W. Field, and A. A. Kachanov, "Intensity measurements and collision-broadening coefficients for the oxygen A band measured by IntraCavity Laser Absorption Spectroscopy," *Journal of Molecular Spectroscopy*, vol. 201, no. 2, pp. 188–197, 2000.

[14] S. K. Witonsky, M. R. Canagaratna, S. L. Coy, J. I. Steinfeld, R. W. Field, and A. A. Kachanov, "The $3\nu_1$ overtone band of trans-nitrous acid: Rotational and perturbation analysis and absolute intensity," *Journal of Chemical Physics*, vol. 115, no. 7, pp. 3134–3143, 2001.

[15] M. J. Molina and L. T. Molina, *Air Quality in the Mexico Megacity: An Integrated Assessment*, vol. 2 of *Science & Technology: Tools for Sustainable Development*. Boston: Kluwer Academic Publishers, 2002.

[16] S. K. Witonsky, *Kinetics and Dynamics Measured Using IntraCavity Laser Abosrption Spectroscopy*. Phd thesis, Massachusetts Institute of Technology, 2002.

[17] A. Kachanov, A. Charvat, and F. Stoeckel, "Intracavity laser spectroscopy with vibronic solid-state lasers .1. spectrotemporal transient-behavior of a Ti-sapphire laser," *Journal of the Optical Society of America B-Optical Physics*, vol. 11, no. 12, pp. 2412–2421, 1994.

[18] A. Campargue, F. Stoeckel, and M. Chenevier, "High-sensitivity intracavity laser spectroscopy - applications to the study of overtone transitions in the visible range," *Spectrochimica Acta Reviews*, vol. 13, no. 1, pp. 69–88, 1990.

[19] P. Moulton *Optical News*, vol. 8, p. 9, 1982.

[20] A. B. Budgor, L. Esterowitz, and L. G. DeShazer, *Tunable solid-state lasers II: Proceedings of the OSA Topical Meeting, Rippling River Resort, Zigzag, Oregon,*

June 4-6, 1986. Springer series in optical sciences ; v. 52, Berlin ; New York: Springer-Verlag, 1986.

[21] W. Demtröder, *Laser spectroscopy: Basic Concepts and Instrumentation.* Advanced texts in physics,, Berlin ; New York: Springer, 3rd ed., 2003.

[22] W. Sooy *Appl. Phys. Lett,* vol. 7, p. 36, 1965.

[23] A. Kachanov, "ICLAS User's Manual," 1994.

[24] E. N. Antonov, P. S. Antsyferov, A. A. Kachanov, and V. G. Koloshnikov, "Parasitic selection in intra-cavity laser detection spectroscopy," *Optics Communications,* vol. 41, no. 2, pp. 131–134, 1982.

[25] A. Kachanov, A. Charvat, and F. Stoeckel, "Intracavity laser spectroscopy with vibronic solid-state lasers .2. influence of the nonlinear mode-coupling on the maximum sensitivity of a Ti-Sapphire laser," *Journal of the Optical Society of America B-Optical Physics,* vol. 12, no. 6, pp. 970–979, 1995.

[26] A. A. Kachanov, V. R. Mironenko, and I. K. Pashkovich, "Quantum-limited sensitivity threshold in a traveling-wave intracavity laser spectrometer," *Kvantovaya Elektronika,* vol. 16, no. 1, pp. 146–152, 1989.

[27] C. L. Pan, C. D. Hwang, J. C. Kuo, J. M. Shieh, and K. H. Wu, "Birefringence-induced spectral features in continuous-wave and passively mode-locked Ti-Sapphire lasers," *Optics Letters,* vol. 17, no. 21, pp. 1547–1549, 1992.

[28] C. L. Pan, J. C. Kuo, C. D. Hwang, J. M. Shieh, Y. Lai, C. S. Chang, and K. H. Wu, "Buildup dynamics of the spectrum and the average output power of a homogeneously broadened continuous-wave Ti-Sapphire laser," *Optics Letters,* vol. 17, no. 14, pp. 994–996, 1992.

[29] L. S. Rothman, C. P. Rinsland, A. Goldman, S. T. Massie, D. P. Edwards, J. M. Flaud, A. Perrin, C. Camy-Peyret, V. Dana, J. Y. Mandin, J. Schroeder, A. McCann, R. R. Gamache, R. B. Wattson, K. Yoshino, K. V. Chance, K. W.

Jucks, L. R. Brown, V. Nemtchinov, and P. Varanasi, "The HITRAN molecular spectroscopic database and HAWKS (HITRAN atmospheric workstation): 1996 edition," *Journal of Quantitative Spectroscopy & Radiative Transfer*, vol. 60, no. 5, pp. 665–710, 1998.

[30] S. Gerstenkorn, P. Luc, and J. Verges, *Atlas du Spectre d'Absorption da la Molecule d'Iode: 7200-11200 cm^{-1}*. Paris: CNRS, 1993.

[31] M. G. Bryukov, A. A. Kachanov, R. Timonnen, J. Seetula, J. Vandoren, and O. M. Sarkisov, "Kinetics of HNO reactions with O_2 and HNO," *Chemical Physics Letters*, vol. 208, no. 5-6, pp. 392–398, 1993.

[32] C. J. Howard, "Kinetic measurements using flow tubes," *Journal of Physical Chemistry*, vol. 83, no. 1, pp. 3–9, 1979.

[33] J. V. Seeley, J. T. Jayne, and M. J. Molina, "Kinetic studies of chlorine atom reactions using the turbulent flow tube technique," *Journal of Physical Chemistry*, vol. 100, no. 10, pp. 4019–4025, 1996.

[34] J. I. Steinfeld, J. S. Francisco, and W. L. Hase, *Chemical kinetics and dynamics*. Upper Saddle River, N.J.: Prentice Hall, 2nd ed., 1999.

[35] W. B. DeMore and J. P. L. (U.S.), *Chemical kinetics and photochemical data for use in stratospheric modeling : Evaluation number 11*. JPL publication ; 94-26, Pasadena, Calif.: National Aeronautics and Space Administration, Jet Propulsion Laboratory, California Institute of Technology, 1994.

[36] T. E. Graedel, W. D. Langer, and M. A. Frerking, "The kinetic chemistry of dense inter-stellar clouds," *Astrophysical Journal Supplement Series*, vol. 48, no. 3, pp. 321–368, 1982.

[37] Y. P. Viala, "Chemical-equilibrium from diffuse to dense interstellar clouds .1. galactic molecular clouds," *Astronomy & Astrophysics Supplement Series*, vol. 64, no. 3, pp. 391–437, 1986.

[38] J. A. Miller and C. T. Bowman, "Mechanism and modeling of nitrogen chemistry in combustion," *Progress in Energy and Combustion Science*, vol. 15, no. 4, pp. 287–338, 1989.

[39] M. R. Soto, M. Page, and M. L. McKee, "Configuration-interaction calculations of structures, vibrational frequencies, and heats of formation for HHNO species," *Chemical Physics Letters*, vol. 187, no. 4, pp. 335–344, 1991.

[40] R. A. Viereck, L. S. Bernstein, S. B. Mende, E. Murad, G. R. Swenson, and C. P. Pike, "Visible spectra of thruster plumes from the space-shuttle primary reaction control-system," *Journal of Spacecraft and Rockets*, vol. 30, no. 6, pp. 724–730, 1993.

[41] F. Dalby *Can. J. Phys.*, vol. 36, p. 1336, 1958.

[42] D. R. J.L. Bancroft, J.M. Hollas *Can. J. Phys.*, vol. 40, p. 322, 1962.

[43] J. W. C. Johns and A. R. W. McKellar, "Laser stark spectroscopy of fundamental bands of HNO (ν_2 and ν_3) and DNO (ν_1 and ν_2)," *Journal of Chemical Physics*, vol. 66, no. 3, pp. 1217–1224, 1977.

[44] R. N. Dixon, M. Noble, C. A. Taylor, and M. Delhoume, "Magnetic-field and time-resolved studies of the electronic-spectrum of HNO," *Faraday Discussions*, no. 71, pp. 125–142, 1981.

[45] R. N. Dixon, K. B. Jones, M. Noble, and S. Carter, "The mechanism of HNO predissociation - an interpretation using analytical potential-energy functions for the $\tilde{A}^1 A''$, $\tilde{A}^3 A''$ and $\tilde{X}^1 A'$ states," *Molecular Physics*, vol. 42, no. 2, pp. 455–473, 1981.

[46] K. Obi, Y. Matsumi, Y. Takeda, S. Mayama, H. Watanabe, and S. Tsuchiya, "Fluorescence lifetimes and excitation-spectra of the jet-cooled HNO radical," *Chemical Physics Letters*, vol. 95, no. 6, pp. 520–524, 1983. Article.

[47] S. G. Cheskis, V. A. Nadtochenko, and O. M. Sarkisov, "Study of the HNO + HNO and HNO + NO reactions by intra-cavity laser spectroscopy," *International Journal of Chemical Kinetics*, vol. 13, no. 10, pp. 1041–1050, 1981.

[48] D. H. Mordaunt, H. Flothmann, M. Stumpf, H. M. Keller, C. Beck, R. Schinke, and K. Yamashita, "The dissociation of HNO .1. potential energy surfaces for the $\tilde{X}^1 A'$, $\tilde{A}^1 a''$, and $\tilde{A}^3 a''$ states," *Journal of Chemical Physics*, vol. 107, no. 17, pp. 6603–6615, 1997.

[49] D. Lide *J. Chem. Phys.*, vol. 20, p. 1761, 1952.

[50] C. Foissac, A. Campargue, A. Kachanov, P. Supiot, G. Weirauch, and N. Sadeghi, "Intracavity laser absorption spectroscopy applied to measure the absolute density and temperature of N_2 $(A^3\Sigma_u^+)$ metastable molecules in a flowing N_2 microwave discharge," *Journal of Physics D-Applied Physics*, vol. 33, no. 19, pp. 2434–2441, 2000.

[51] N. Sadeghi, C. Foissac, and P. Supiot, "Kinetics of N_2 $(A^3\Sigma_u^+)$ molecules and ionization mechanisms in the afterglow of a flowing N_2 microwave discharge," *Journal of Physics D-Applied Physics*, vol. 34, no. 12, pp. 1779–1788, 2001.

[52] M. Clyne and B. Thrush *Dis. Faraday Soc.*, vol. 33, p. 139, 1962.

[53] J. Jordan, "Hydrogen impurity in helium 5.0 grade," October 2004.

[54] L. Stonge and M. Moisan, "Hydrogen-atom yield in RF and microwave hydrogen discharges," *Plasma Chemistry and Plasma Processing*, vol. 14, no. 2, pp. 87–116, 1994.

[55] S. Miyazaki and S. Takahashi *Mem. Defense Acad. Japan*, vol. 9, p. 643, 1969.

[56] M. Clyne and B. Thrush *Trans. Faraday Soc.*, vol. 57, p. 1305, 1961.

[57] D. Hartley and B. Thrush *Proc. Roy. Soc. A*, vol. 297, p. 520, 1967.

[58] R. L. Brown, "Tubular flow reactors with 1st-order kinetics," *Journal of Research of the National Bureau of Standards*, vol. 83, no. 1, pp. 1–8, 1978.

[59] A. B. Callear and R. W. Carr, "Thermal-decomposition of HNO," *Journal of the Chemical Society-Faraday Transactions Ii*, vol. 71, pp. 1603–1609, 1975.

[60] L. S. Rothman, A. Barbe, D. C. Benner, L. R. Brown, C. Camy-Peyret, M. R. Carleer, K. Chance, C. Clerbaux, V. Dana, V. M. Devi, A. Fayt, J. M. Flaud, R. R. Gamache, A. Goldman, D. Jacquemart, K. W. Jucks, W. J. Lafferty, J. Y. Mandin, S. T. Massie, V. Nemtchinov, D. A. Newnham, A. Perrin, C. P. Rinsland, J. Schroeder, K. M. Smith, M. A. H. Smith, K. Tang, R. A. Toth, J. Vander Auwera, P. Varanasi, and K. Yoshino, "The HITRAN molecular spectroscopic database: edition of 2000 including updates through 2001," *Journal of Quantitative Spectroscopy & Radiative Transfer*, vol. 82, no. 1-4, pp. 5–44, 2003.

[61] A. Charvat, S. F. Deppe, H. H. Hamann, and B. Abel, "The $3\nu_1 + \nu_2$ combination band of HOCl: Assignments, perturbations, and line intensities," *Journal of Molecular Spectroscopy*, vol. 185, no. 2, pp. 336–346, 1997.

[62] K. H. Becker, E. H. Fink, P. Langen, and U. Schurath, "Near-infrared emission bands of HO_2 radical," *Journal of Chemical Physics*, vol. 60, no. 11, pp. 4623–4625, 1974.

[63] K. H. Becker, E. H. Fink, A. Leiss, and U. Schurath, "Study of near-infrared emission bands of hydroperoxyl radical at medium resolution," *Chemical Physics Letters*, vol. 54, no. 1, pp. 191–196, 1978.

[64] E. H. Fink and D. A. Ramsay, "High-resolution study of the $A^1 A'' \leftarrow X^1 A'$ transition of HO_2: Analysis of the 000-000 band," *Journal of Molecular Spectroscopy*, vol. 185, no. 2, pp. 304–324, 1997.

[65] P. A. Freedman and W. J. Jones, "Rotational analysis of $^2 A' \rightarrow^2 A''$ emission band system of HO_2 at 1.43 μm," *Journal of the Chemical Society-Faraday Transactions Ii*, vol. 72, pp. 207–215, 1976.

[66] K. J. Holstein, E. H. Fink, J. Wildt, R. Winter, and F. Zabel, "Mechanisms of $HO_2(A^2A')$ excitation in various chemical-systems," *Journal of Physical Chemistry*, vol. 87, no. 20, pp. 3943–3948, 1983.

[67] H. E. Hunziker and H. R. Wendt, "Near-infrared absorption-spectrum of HO_2," *Journal of Chemical Physics*, vol. 60, no. 11, pp. 4622–4623, 1974.

[68] H. E. Hunziker and H. R. Wendt, "Electronic absorption-spectra of organic peroxyl radicals in the near infrared," *Journal of Chemical Physics*, vol. 64, no. 8, pp. 3488–3490, 1976.

[69] K. Nagai, Y. Endo, and E. Hirota, "Diode-laser spectroscopy of the HO_2 ν_2 band," *Journal of Molecular Spectroscopy*, vol. 89, no. 2, pp. 520–527, 1981.

[70] D. D. Nelson and M. S. Zahniser, "Diode-laser spectroscopy of the ν_3 vibration of the HO_2 radical," *Journal of Molecular Spectroscopy*, vol. 150, no. 2, pp. 527–534, 1991.

[71] R. P. Tuckett, P. A. Freedman, and W. J. Jones, "Emission bands of HO_2 between 1.43 and 1.51 μm," *Molecular Physics*, vol. 37, no. 2, pp. 379–401, 1979.

[72] C. Yamada, Y. Endo, and E. Hirota, "Difference frequency laser spectroscopy of the ν_1 band of the HO_2 radical," *Journal of Chemical Physics*, vol. 78, no. 7, pp. 4379–4384, 1983.

[73] M. S. Zahniser and A. C. Stanton, "A measurement of the vibrational band strength for the ν_3 band of the HO_2 radical," *Journal of Chemical Physics*, vol. 80, no. 10, pp. 4951–4960, 1984.

[74] M. S. Zahniser, K. E. Mccurdy, and A. C. Stanton, "Quantitative spectroscopic studies of the HO_2 radical - band strength measurements for the ν_1 and ν_2 vibrational bands," *Journal of Physical Chemistry*, vol. 93, no. 3, pp. 1065–1070, 1989.

[75] J. M. Cronkhite, R. E. Stickel, J. M. Nicovich, and P. H. Wine, "Laser flash photolysis studies of radical-radical reaction kinetics: The HO_2+IO reaction," *Journal of Physical Chemistry A*, vol. 103, no. 17, pp. 3228–3236, 1999.

[76] S. Aloisio, J. S. Francisco, and R. R. Friedl, "Experimental evidence for the existence of the $HO_2 \bullet H_2O$ complex," *Journal of Physical Chemistry A*, vol. 104, no. 28, pp. 6597–6601, 2000.

[77] R. R. Lii, M. C. Sauer, and S. Gordon, "Temperature-dependence of the gas-phase self-reaction of HO_2 in the presence of H_2O," *Journal of Physical Chemistry*, vol. 85, no. 19, pp. 2833–2834, 1981.

[78] S. Aloisio and J. S. Francisco, "Existence of a hydroperoxy and water ($HO_2 \bullet H_2O$) radical complex," *Journal of Physical Chemistry A*, vol. 102, no. 11, pp. 1899–1902, 1998.

[79] H. Levy, "Normal atmosphere: Large radical and formaldehyde concentrations predicted," *Science*, vol. 173, pp. 141–143, 1971.

[80] B. Weinstock, "Carbon monoxide: Residence time in the atmosphere," *Science*, vol. 166, pp. 224–225, 1969.

[81] M. J. Molina, A. V. Ivanov, S. Trakhtenberg, and L. T. Molina, "Atmospheric evolution of organic aerosol," *Geophysical Research Letters*, vol. 31, no. 22, 2004.

[82] J. H. Mather, P. S. Stevens, and W. H. Brune, "OH and HO_2 measurements using laser-induced fluorescence," *Journal of Geophysical Research-Atmospheres*, vol. 102, no. D5, pp. 6427–6436, 1997.

[83] P. S. Stevens, J. H. Mather, and W. H. Brune, "Measurement of tropospheric OH and HO_2 by laser-induced fluorescence at low-pressure," *Journal of Geophysical Research-Atmospheres*, vol. 99, no. D2, pp. 3543–3557, 1994.

[84] H. P. Dorn, U. Brandenburger, T. Brauers, and H. Hausmann, "A new in-situ laser long-path absorption instrument for the measurement of tropospheric OH

radicals," *Journal of the Atmospheric Sciences*, vol. 52, no. 19, pp. 3373–3380, 1995.

[85] T. Reiner, M. Hanke, and F. Arnold, "Atmospheric peroxy radical measurements by ion molecule reaction mass spectrometry: A novel analytical method using amplifying chemical conversion to sulfuric acid," *Journal of Geophysical Research-Atmospheres*, vol. 102, no. D1, pp. 1311–1326, 1997.

[86] J. P. Abram, D. J. Creasey, D. E. Heard, J. D. Lee, and M. J. Pilling, "Hydroxyl radical and ozone measurements in England during the solar eclipse of 11 August 1999," *Geophysical Research Letters*, vol. 27, no. 21, pp. 3437–3440, 2000.

[87] D. E. Heard, L. J. Carpenter, D. J. Creasey, J. R. Hopkins, J. D. Lee, A. C. Lewis, M. J. Pilling, P. W. Seakins, N. Carslaw, and K. M. Emmerson, "High levels of the hydroxyl radical in the winter urban troposphere," *Geophysical Research Letters*, vol. 31, no. 18, 2004.

[88] L. A. George, T. M. Hard, and R. J. O'Brien, "Measurement of free radicals OH and HO_2 in los angeles smog," *Journal of Geophysical Research-Atmospheres*, vol. 104, no. D9, pp. 11643–11655, 1999.

[89] M. Martinez, H. Harder, T. A. Kovacs, J. B. Simpas, J. Bassis, R. Lesher, W. H. Brune, G. J. Frost, E. J. Williams, C. A. Stroud, B. T. Jobson, J. M. Roberts, S. R. Hall, R. E. Shetter, B. Wert, A. Fried, B. Alicke, J. Stutz, V. L. Young, A. B. White, and R. J. Zamora, "OH and HO_2 concentrations, sources, and loss rates during the Southern Oxidants Study in Nashville, Tennessee, summer 1999," *Journal of Geophysical Research-Atmospheres*, vol. 108, no. D19, 2003.

[90] M. Martinez, H. Harder, W. Brune, P. Di Carlo, E. Williams, D. Hereid, T. Jobson, W. Kuster, J. Roberts, D. Trainer, and A. Geyer, "The behavior of the hydroxyl and hydroperoxyl radicals during TexAQS2000. Abstract A12D-0174," in *AGU Fall Meeting*, (San Francisco CA), EOS Transactions, 2002.

[91] X. R. Ren, H. Harder, M. Martinez, R. L. Lesher, A. Oliger, J. B. Simpas, W. H. Brune, J. J. Schwab, K. L. Demerjian, Y. He, X. L. Zhou, and H. G. Gao, "OH and HO_2 chemistry in the urban atmosphere of New York City," *Atmospheric Environment*, vol. 37, no. 26, pp. 3639–3651, 2003.

[92] U. Platt, B. Alicke, R. Dubois, A. Geyer, A. Hofzumahaus, F. Holland, M. Martinez, D. Mihelcic, T. Klupfel, B. Lohrmann, W. Patz, D. Perner, F. Rohrer, J. Schafer, and J. Stutz, "Free radicals and fast photochemistry during BERLIOZ," *Journal of Atmospheric Chemistry*, vol. 42, no. 1, pp. 359–394, 2002.

[93] F. C. W. Lurmann and C. LA, "A surrogate species chemical reaction mechanism for urban-scale air quality simulation models," Tech. Rep. EPA/600/3-87/014, US Environmnetal Protection Agency, Research Triangle Park, NC, 1987 1987.

[94] G. J. Frost, M. Trainer, G. Allwine, M. P. Buhr, J. G. Calvert, C. A. Cantrell, F. C. Fehsenfeld, P. D. Goldan, J. Herwehe, G. Hubler, W. C. Kuster, R. Martin, R. T. McMillen, S. A. Montzka, R. B. Norton, D. D. Parrish, B. A. Ridley, R. E. Shetter, J. G. Walega, B. A. Watkins, H. H. Westberg, and E. J. Williams, "Photochemical ozone production in the rural southeastern United States during the 1990 Rural Oxidants in the Southern Environment (ROSE) program," *Journal of Geophysical Research-Atmospheres*, vol. 103, no. D17, pp. 22491–22508, 1998.

[95] W. R. Stockwell, F. Kirchner, M. Kuhn, and S. Seefeld, "A new mechanism for regional atmospheric chemistry modeling," *Journal of Geophysical Research-Atmospheres*, vol. 102, no. D22, pp. 25847–25879, 1997.

[96] M. E. Jenkin, S. M. Saunders, and M. J. Pilling, "The tropospheric degradation of volatile organic compounds: A protocol for mechanism development," *Atmospheric Environment*, vol. 31, no. 1, pp. 81–104, 1997.

139

[97] S. M. Saunders, M. E. Jenkin, R. G. Derwent, and M. J. Pilling, "Protocol for the development of the master chemical mechanism, MCM v3 (Part A): tropospheric degradation of non-aromatic volatile organic compounds," *Atmospheric Chemistry and Physics*, vol. 3, pp. 161–180, 2003.

[98] R. Simonaitis, J. F. Meagher, and E. M. Bailey, "Evaluation of the condensed Carbon Bond (CB-IV) mechanism against smog chamber data at low VOC and NOx concentrations," *Atmospheric Environment*, vol. 31, no. 1, pp. 27–43, 1997.

[99] C. Bloss, V. Wagner, A. Bonzanini, M. E. Jenkin, K. Wirtz, M. Martin-Reviejo, and M. J. Pilling, "Evaluation of detailed aromatic mechanisms (MCMv3 and MCMv3.1) against environmental chamber data," *Atmospheric Chemistry and Physics*, vol. 5, pp. 623–639, 2005.

[100] C. Bloss, V. Wagner, M. E. Jenkin, R. Volkamer, W. J. Bloss, J. D. Lee, D. E. Heard, K. Wirtz, M. Martin-Reviejo, G. Rea, J. C. Wenger, and M. J. Pilling, "Development of a detailed chemical mechanism (MCMv3.1) for the atmospheric oxidation of aromatic hydrocarbons," *Atmospheric Chemistry and Physics*, vol. 5, pp. 641–664, 2005.

[101] M. E. Jenkin, S. M. Saunders, V. Wagner, and M. J. Pilling, "Protocol for the development of the Master Chemical mechanism, MCM v3 (Part B): tropospheric degradation of aromatic volatile organic compounds," *Atmospheric Chemistry and Physics*, vol. 3, pp. 181–193, 2003.

[102] R. I. Olariu, I. Barnes, K. H. Becker, and B. Klotz, "Rate coefficients for the gas-phase reaction of OH radicals with selected dihydroxybenzenes and benzoquinones," *International Journal of Chemical Kinetics*, vol. 32, no. 11, pp. 696–702, 2000.

[103] H. L. Bethel, J. Arey, and R. Atkinson, "Products of the OH radical-initiated reaction of 3-hexene-2,5-dione," *Environmental Science & Technology*, vol. 35, no. 22, pp. 4477–4480, 2001.

[104] R. Volkamer, B. Klotz, I. Barnes, T. Imamura, K. Wirtz, N. Washida, K. H. Becker, and U. Platt, "OH-initiated oxidation of benzene - Part I. phenol formation under atmospheric conditions," *Physical Chemistry Chemical Physics*, vol. 4, no. 9, pp. 1598–1610, 2002.

[105] R. I. Olariu, B. Klotz, I. Barnes, K. H. Becker, and R. Mocanu, "FT-IR study of the ring-retaining products from the reaction of OH radicals with phenol, o-, m-, and p-cresol," *Atmospheric Environment*, vol. 36, no. 22, pp. 3685–3697, 2002.

[106] B. Klotz, R. Volkamer, M. D. Hurley, M. P. S. Andersen, O. J. Nielsen, I. Barnes, T. Imamura, K. Wirtz, K. H. Becker, U. Platt, T. J. Wallington, and N. Washida, "OH-initiated oxidation of benzene - part ii. influence of elevated NOx concentrations," *Physical Chemistry Chemical Physics*, vol. 4, no. 18, pp. 4399–4411, 2002.

[107] P. Martin, E. C. Tuazon, S. M. Aschmann, J. Arey, and R. Atkinson, "Formation and atmospheric reactions of 4,5-dihydro-2-methylfuran," *Journal of Physical Chemistry A*, vol. 106, no. 47, pp. 11492–11501, 2002.

[108] R. Volkamer, U. Platt, and K. Wirtz, "Primary and secondary glyoxal formation from aromatics: Experimental evidence for the bicycloalkyl-radical pathway from benzene, toluene, and p-xylene," *Journal of Physical Chemistry A*, vol. 105, no. 33, pp. 7865–7874, 2001.

[109] R. I. Olariu, *Atmospheric Oxidation of Selected Aromatic Hydrocarbons*. Phd thesis, Bergische Universitaet Gesamthochschule Wuppertal, 2001.

[110] R. Volkamer, *A DOAS study on the oxidation mechanism of aromatic hydrocarbons under simulated atmospheric conditions*. Phd thesis, University of Heidelberg, 2001.

[111] A. Curtis and W. Sweetenham, "FACSIMILE/CHEKMAT user's manual," Tech. Rep. AERE Rep-R12805, Her Majest's Stationery Office, 1987.

[112] B. Lamb, E. Velasco, E. Allwine, H. H. Westberg, S. Herndon, B. Knighton, E. Grimsrud, T. Jobson, M. Alexander, and P. Prezeller, "Ambient VOC measurements in Mexico City," in *American Meteorology Society Fifth Conference on Urban Environment*, (Vancouver, Canada), 2004.

[113] R. A. Harley, M. P. Hannigan, and G. R. Cass, "Respeciation of organic gas emissions and the detection of excess unburned gasoline in the atmosphere," *Environmental Science & Technology*, vol. 26, no. 12, pp. 2395–2408, 1992.

[114] A. B. Guenther and A. J. Hills, "Eddy covariance measurement of isoprene fluxes," *Journal of Geophysical Research-Atmospheres*, vol. 103, no. D11, pp. 13145–13152, 1998.

[115] R. Volkamer, T. Etzkorn, A. Geyer, and U. Platt, "Correction of the oxygen interference with UV spectroscopic (DOAS) measurements of monocyclic aromatic hydrocarbons in the atmosphere," *Atmospheric Environment*, vol. 32, no. 21, pp. 3731–3747, 1998.

[116] R. Volkamer, L. T. Molina, M. J. Molina, E. Flores, M. Grutter, B. Galle, J. Mellqvist, J. Samuelsson, B. Knighton, and B. T. Jobson, "Open-path emission factors derived from DOAS and FTIR measurements in the Mexico City Metropolitan Area," *American Geophysical Union, Fall Meeting Supplement*, vol. 85, no. 47, pp. Abstract A11A–0003, 2004.

[117] H. A. Pollutants, "EPA AirData Monitor Values Report," *EPA AirData Reports, http://www.epa.gov/air/data*, 2004.

[118] B. T. Jobson, M. Alexander, P. Prazeller, C. M. Berkowitz, R. Volkamer, L. T. Molina, H. Westberg, B. Lamb, E. Velasco, and E. Allwine, "Hydrocarbon measurements during the MCMA2003 field experiment: Intercomparison and analysis," *American Geophysical Union, Fall Meeting Supplement*, vol. 85, no. 47, pp. Abstract A11A–0001, 2004.

[119] R. Volkamer, U. Platt, M. Garcia, K. Wirtz, and W. Jukermann, "Comparison of calibration standards for the measurement of HCHO via UV-, IR absorption spectroscopy and the Hantzsch technique," tech. rep., 2005 (in press).

[120] R. Volkamer, L. Molina, M. Molina, T. Shirley, and W. H. Brune, "DOAS measurement of glyoxal as an indicator for fast VOC chemistry in urban air," *Geophysical Research Letters*, vol. 32, no. 8, p. L08806, 2005.

[121] R. B. Stull, *Meteorology for Scientists and Engineers.* Pacific Grove: Brooks/Cole, second ed., 2000.

[122] T. M. Hard, R. J. Obrien, C. Y. Chan, and A. A. Mehrabzadeh, "Tropospheric free-radical determination by FAGE," *Environmental Science and Technology*, vol. 18, no. 10, pp. 768–777, 1984.

[123] N. Carslaw, D. J. Creasey, D. E. Heard, A. C. Lewis, J. B. McQuaid, M. J. Pilling, P. S. Monks, B. J. Bandy, and S. A. Penkett, "Modeling OH, HO_2, and RO_2 radicals in the marine boundary layer - 1. Model construction and comparison with field measurements," *Journal of Geophysical Research-Atmospheres*, vol. 104, no. D23, pp. 30241–30255, 1999.

[124] V. Wagner, M. E. Jenkin, S. M. Saunders, J. Stanton, K. Wirtz, and M. J. Pilling, "Modelling of the photooxidation of toluene: conceptual ideas for validating detailed mechanisms," *Atmospheric Chemistry and Physics*, vol. 3, pp. 89–106, 2003.

[125] B. J. Finlayson-Pitts and J. N. Pitts, *Chemistry of the upper and lower atmosphere : theory, experiments and applications.* San Diego, Calif. ; London: Academic Press, 2000.

[126] J. G. Calvert, *The mechanisms of atmospheric oxidation of aromatic hydrocarbons.* Oxford ; New York: Oxford University Press, 2002.

[127] J. G. Calvert, *The mechanisms of atmospheric oxidation of the alkenes.* New York: Oxford University Press, 2000.

[128] R. Volkamer, I. Barnes, U. Platt, L. Molina, and M. Molina, *Remote Sensing of Glyoxal by Differential Optical Absorption Spectroscopy (DOAS): Advancements in Simulation Chamber and Field Experiments.* in press, Kluwer, 2005.

[129] N. Carslaw, P. J. Jacobs, and M. J. Pilling, "Modeling OH,HO_2, and RO_2 radicals in the marine boundary layer 2. Mechanism reduction and uncertainty analysis," *Journal of Geophysical Research-Atmospheres*, vol. 104, no. D23, pp. 30257–30273, 1999.

[130] A. M. Thompson and R. W. Stewart, "Effect of chemical-kinetics uncertainties on calculated constituents in a tropospheric photochemical model," *Journal of Geophysical Research-Atmospheres*, vol. 96, no. D7, pp. 13089–13108, 1991.

[131] T. Shirley, W. H. Brune, X. R. Ren, J. Mao, R. L. Lesher, B. Cardenas, R. Volkamer, M. J. Molina, L. Molina, B. Lamb, E. Velasco, T. Jobson, and M. Alexander, "Atmospheric oxidation in the Mexico City Metropolitan Area (MCMA) during April 2003," *unpublished work*, unpublished work.

[132] P. Di Carlo, W. H. Brune, M. Martinez, H. Harder, R. Lesher, X. R. Ren, T. Thornberry, M. A. Carroll, V. Young, P. B. Shepson, D. Riemer, E. Apel, and C. Campbell, "Missing OH reactivity in a forest: Evidence for unknown reactive biogenic VOCs," *Science*, vol. 304, no. 5671, pp. 722–725, 2004.

[133] X. R. Ren, H. Harder, M. Martinez, R. L. Lesher, A. Oliger, T. Shirley, J. Adams, J. B. Simpas, and W. H. Brune, "HOx concentrations and OH reactivity observations in New York City during PMTACS-NY2001," *Atmospheric Environment*, vol. 37, no. 26, pp. 3627–3637, 2003.

[134] T. A. Kovacs, W. H. Brune, H. Harder, M. Martinez, J. B. Simpas, G. J. Frost, E. Williams, T. Jobson, C. Stroud, V. Young, A. Fried, and B. Wert, "Direct measurements of urban OH reactivity during Nashville SOS in summer 1999," *Journal of Environmental Monitoring*, vol. 5, no. 1, pp. 68–74, 2003.

[135] J. P. D. Abbatt and M. J. Molina, "Status of stratospheric ozone depletion," *Annual Review of Energy and the Environment*, vol. 18, pp. 1–29, 1993.

[136] A. E. Jones and J. D. Shanklin, "Continued decline of total ozone over Halley, Antarctica, since 1985," *Nature*, vol. 376, no. 6539, pp. 409–411, 1995.

[137] M. J. Molina and F. S. Rowland, "Stratospheric sink for chlorofluoromethanes - chlorine atomic-catalysed destruction of ozone," *Nature*, vol. 249, no. 5460, pp. 810–812, 1974.

[138] P. Crutzen, "The influence of nitrogen oxides on atmospheric ozone content," *Q.J.R. Meteorol. Soc.*, vol. 96, pp. 320–325, 1970.

Philip Sheehy

Business Address:
Massachusetts Institute of Technology
77 Massachusetts Avenue 54-314
Cambridge, MA 02139
617.452.3265
sheehy@mit.edu

Home Address:
213 Harvard St – Apt 1L
Cambridge, MA 02139
617.970.0887

Education/ Research Experience

Massachusetts Institute of Technology   Cambridge, MA
Advisors: Professors Jeffrey I. Steinfeld and Mario J. Molina
Doctor of Philosophy, Department of Chemistry, *2005*. Researched kinetics and spectroscopy of trace species using IntraCavity Laser Absorption Spectroscopy in order to assess role(s) in a variety of atmospheric processes. Developed a uniquely tailored box model to improve understanding of oxidative capacity of Mexico City Metropolitan Area (MCMA) urban troposphere.
(September 2000 – June 2005)

MIT Department of Urban Studies and Planning   Cambridge, MA
Advisor: Dara O'Rourke
Technical and scientific assistance to Community Environmental Monitoring project (CEMP), focusing on developing strategies for community participation in measuring air quality. Developed simplified tools for gathering air quality information by building on existing community interests and activities.
(May 2002-present)

Kalamazoo College   Kalamazoo, MI
Bachelor of Arts, Chemistry and Physics, Cum Laude, *2000*. Participated in research at Pharmacia as part of a Senior Individualized Project (SIP) that resulted in a thesis and presentation. Thesis: Determination of the Binding Constant between Alprostadil and alpha-cyclodextrin by Conductivity and Microcalorimetry (Advisor: Tore Ramstad).
(September 1996 – June 2000)

Teaching Experience

MIT, Department of Chemistry   Cambridge, MA
Introductory Chemistry Laboratory and Introductory Chemistry, Teaching Assistant
Supervised one group (5-8 students) in the laboratory. Responsible for writing, administering and grading quizzes as well as laboratory reports. In classroom, responsible for attending lectures and conducting two recitation lectures a week to a group of 20+ students. Assisted writing and grading problems sets and exams. (September 2000 – May 2001)

Kalamazoo College   Kalamazoo, MI
Physical/Analytical/Organic Chemistry, Laboratory Assistant
Supervised students and answered questions regarding all experiments. Aided in set-up and pre-laboratory preparations. Available outside of the laboratory to answer questions regarding write-up. Responsible for grading of laboratory reports. (September 1998-June 2000)

Publications

"Discharge-Flow Kinetics Measurements using Intra-Cavity Laser Absorption Spectroscopy", P. Sheehy and J.I. Steinfeld, *Journal of Physical Chemistry B*, **2005**, *109*, 8358-8362.

"Determination of the Molecular complexation constant between alprostadil and alpha-cyclodextrin by conductometry: Implications for a freeze-dried formulation", P. Sheehy and T. Ramstad, submitted to *Journal of Pharmaceutical and Biomedical Analysis*